



AN ABSTRACT OF THE THESIS OF

Charles Rymal for the degree of Master of Science in

Mechanical Engineering presented on November 7, 2014.

Title: Numerical Design of a High-Flux Microchannel Solar Receiver.

Abstract approved: \_\_\_\_\_

Sourabh V. Apte

This thesis discusses the design of several microchannel solar receiver devices for use in CSP (concentrated solar power) using CFD (computational fluid dynamics) simulations. The goal is to demonstrate that, by taking advantage of the higher heat transfer coefficient of microchannels, solar receivers can achieve higher efficiency than current receiver technology, reducing the cost of solar thermal power. Design using CFD simulations is necessary in order to estimate the performance of different designs and identify potential issues before investing in a real device. The lack of previous research into such devices is most likely due to challenges concerning (a) the manufacturing of microchannels in materials that are suited to the high temperature and stress of the application and (b) the design of a headering system for a large scale implementation. Both supercritical carbon-dioxide and molten salt are used as heat-transfer fluids. The required inlet and outlet temperatures of the fluid are 773 K and 923 K for carbon-dioxide and 573 K and 873 K for molten salt. These values are determined by the CSP application and the properties of the fluids. Designs presented range in size from 1 cm<sup>2</sup> to 4 cm<sup>2</sup> and in heat transfer rates from 200 W to 400 W. These values are

determined by the capacity of the solar simulator, which will be used for testing. For carbon-dioxide, three designs are developed with varying manufacturability. The high risk design features a circular micro-pin-fin array created using chemical etching and is constructed using diffusion bonding. The low risk design features machined and welded parts and parallel circular channels. The medium risk design features machined and diffusion bonded parts and parallel rectangular channels. For molten salt, two designs are developed: one using parallel rectangular channels and one using a circular pin-fin array. Conjugate CFD simulations of each design are used to evaluate pressure drop, receiver efficiency, and flow distribution. Two- and three-dimensional structural analyses are used to ensure that the devices will withstand the mechanical and thermal stress. An efficiency of 89.7%, pressure drop of 0.2 bar, and structural safety factor of 1.3 was achieved for carbon-dioxide. An efficiency of 92.1%, pressure drop of 0.5 bar, and structural safety factor of 2.5 was achieved for molten salt. The results demonstrate that microchannel devices can withstand the high flux, temperature, and stress of a CSP application and have high efficiency. However, additional work is needed before these designs can be implemented on a large scale.

©Copyright by Charles Rymal

November 7, 2014

All Rights Reserved

Numerical Design of a High-Flux Microchannel Solar Receiver

by

Charles Rymal

A THESIS

submitted to

Oregon State University

in partial fulfillment of  
the requirements for the  
degree of

Master of Science

Presented November 7, 2014

Commencement June 2015

Master of Science thesis of Charles Rymal presented on  
November 7, 2014

APPROVED:

---

Major Professor, representing Mechanical Engineering

---

Head of the School of Mechanical, Industrial and Manufacturing Engineering

---

Dean of the Graduate School

I understand that my thesis will become part of the permanent collection of Oregon State University libraries. My signature below authorizes release of my thesis to any reader upon request.

---

Charles Rymal, Author

## ACKNOWLEDGMENTS

I would like to express my gratitude to my advisor, Dr. Sourabh Apte, for his guidance and support throughout my graduate program. I also thank my fellow project team members Dr. Kevin Drost, Dr. Vinod Narayanan, Thomas L'Estrange, Eric Truong and Erfan Rasouli, for their collaboration and commitment to this project. All of the MIME faculty and staff who have helped me succeed in my undergraduate and graduate programs. This work was funded by the US Department of Energy SunShot Initiative as well as Oregon BEST. Finally, I want to thank my wife and my family; I could never have done this without them.

# TABLE OF CONTENTS

	<u>Page</u>
1 INTRODUCTION .....	2
1.1 Purpose .....	2
1.2 Goals .....	6
1.2.1 Supercritical Carbon-Dioxide as the Working Fluid .....	6
1.2.2 Molten Salt as the Working Fluid .....	7
1.2.3 Receiver Concept .....	7
1.3 Requirements .....	7
1.3.1 Requirements for Supercritical Carbon-Dioxide .....	7
1.3.2 Requirements for Molten Salt .....	9
1.3.3 General Requirements .....	9
1.3.4 Calculations .....	10
1.3.5 Summary .....	11
2 LITERATURE REVIEW .....	13
2.1 Review of Power Tower Technology .....	13
2.2 Review of Working Fluids .....	17
2.2.1 Super-critical Carbon-Dioxide .....	17
2.2.2 Molten Salt .....	18
2.3 Review of Microchannel Technology .....	18
3 SUPERCRITICAL CARBON-DIOXIDE DESIGNS .....	21
3.1 Limitations of Manufacturing Processes .....	21
3.1.1 Chemical Etching .....	21
3.1.2 Diffusion Bonding .....	22
3.2 Single-Channel Simulations .....	25
3.2.1 Introduction .....	25
3.2.2 Channel Parameters .....	26

## TABLE OF CONTENTS (Continued)

	<u>Page</u>
3.2.3 Setup .....	27
3.2.4 Results .....	30
3.3 Structural Analysis of Pin-Fin Array .....	32
3.4 Material Selection .....	35
3.5 Header Design .....	36
3.5.1 Introduction .....	36
3.5.2 Original Header .....	37
3.5.3 Redesigned Header .....	42
3.6 Pin-Fin Array .....	45
3.6.1 Introduction .....	45
3.6.2 Design Parameters .....	47
3.6.3 Analysis .....	48
3.6.4 Manufacturing Issues .....	51
3.7 Circular Channels .....	54
3.7.1 Introduction .....	54
3.7.2 Design Parameters .....	54
3.7.3 Analysis .....	56
3.8 Rectangular Channels .....	60
3.8.1 Introduction .....	60
3.8.2 Design Parameters .....	62
3.8.3 Analysis .....	64
3.9 Conclusion .....	65
4 MOLTEN SALT DESIGNS .....	68
4.1 Rectangular Channels .....	68
4.1.1 Introduction .....	68
4.1.2 Design Parameters .....	68
4.1.3 Analysis .....	71

TABLE OF CONTENTS (Continued)

	<u>Page</u>
4.2 Pin-Fin Array .....	73
4.2.1 Introduction .....	73
4.2.2 Single Channel Simulations .....	73
4.2.3 Header Simulations .....	76
4.2.4 Design Parameters .....	76
4.2.5 Analysis .....	77
5 ERROR ANALYSIS .....	79
5.1 Introduction .....	79
5.2 Results .....	80
6 EXPERIMENTAL VALIDATION .....	84
6.1 Introduction .....	84
6.2 Experiments .....	85
6.2.1 Experiments with the Device Unheated .....	86
6.2.2 Experiments with the Device Heated .....	86
6.3 Results .....	88
7 SCALED-UP DESIGN .....	90
8 CONCLUSION .....	93
8.1 Recommendation for Future Work .....	94
APPENDIX A EQUATIONS .....	95
A.1 Pin-Fin Geometry .....	95

TABLE OF CONTENTS (Continued)

	<u>Page</u>
A.2 Fluid Dynamics and Heat Transfer .....	97
A.2.1 Mass Flow Rate .....	97
A.2.2 Reynolds Number .....	97
A.2.3 Pressure Drop .....	98
A.2.4 Heat Transfer .....	101
A.3 Efficiency .....	102
A.3.1 Receiver Efficiency .....	102
A.3.2 Thermal Efficiency .....	103
A.3.3 Estimation of Constants .....	103
A.3.4 Overall Efficiency .....	104
APPENDIX B MATERIALS .....	108
B.1 Carbon-Dioxide .....	108
B.2 Dynalene MS-1 .....	108
B.3 Stainless Steel .....	109
B.4 Haynes 214 .....	110
B.5 Haynes 230 .....	110
APPENDIX C EXPERIMENTAL VALIDATION .....	111
REFERENCES .....	113

## LIST OF FIGURES

<u>Figure</u>	<u>Page</u>
1.1 Illustration of a solar power tower plant. ....	3
1.2 Receiver temperature versus Carnot, receiver, and overall efficiency. $K = 4 \times 10^{-4}$ . ....	5
1.3 Solid model illustrating general concept for the receiver. ....	8
2.1 Illustration of a tube array used in a tube receiver. ....	14
2.2 Illustration of a volumetric receiver. ....	15
2.3 Schematic of a solid particle receiver. ....	16
2.4 “Carbon dioxide pressure-temperature phase diagram” by Ben Finney, Mark Jacobs. Licensed under CC0. ....	17
3.1 Cross-section of a sheet of material at three stages in the isotropic etching process. Gray is the solid material and red is the mask. . .	22
3.2 Cross-section of a microchannel device composed of three sheets. The white open regions are the channels. The arrows represent the external pressure used in diffusion bonding. ....	24
3.3 Topview of two sample channel concepts: parallel channels and a circular pin-fin array. Gray represents the solid material, white is the channel, and the arrows represent the direction of fluid flow. ....	25
3.4 Solid models illustrating two sample channel concepts: parallel channels and a circular pin-fin array. ....	26
3.5 Schematic of single channel boundary conditions. Geometry shown is fluid volume; no solid material is shown. ....	31
3.6 Contour plot of von Mises stress from FEA of a single pin. The model is two-dimensional and axisymmetric. The left edge of the model is the centerline of the pin. The color scale is arbitrary; stress increases from blue to red. ....	33
3.7 Three-dimensional wire-frame view of a header concept with one inlet and one outlet to the microchannel array. ....	38
3.8 Three-dimensional wire-frame view of a header concept with two inlets and one outlet to the microchannel array. ....	39

## LIST OF FIGURES (Continued)

<u>Figure</u>	<u>Page</u>
3.9 SCO2 Header Design: Original header concept: Slice of a microchannel device showing an inlet and outlet header channel. Blue and red arrows indicate the direction of flow of cold and hot fluid. Yellow arrows indicate the direction of solar flux. ....	40
3.10 SCO2 Header Design: Original header concept: Contour plot of von Mises stress with exaggerated deflection. The arrows point to the areas of highest stress. Blue indicates minimum stress and red indicates maximum stress. The exact values of stress in this plot are not of interest, only the locations at which high stress occurs. ....	41
3.11 SCO2 Header Design: Redesigned header concept: Slice of a microchannel device showing an inlet and outlet header channel. Blue and red arrows indicate the direction of flow of cold and hot fluid. Yellow arrows indicate the direction of solar flux. ....	42
3.12 SCO2 Header Design: Redesigned header concept: Contour plot of Von-mises stress. The arrows point to the areas of highest stress. Blue indicates minimum stress and red indicates maximum stress. The exact values of stress in this plot are not of interest, only the locations at which high stress occurs. ....	44
3.13 SCO2 Pin-Fin Design: Diagram of pin-fin design. Blue arrows show the path of the cold fluid and red arrows show the path of the hot fluid. ....	46
3.14 SCO2 Pin-Fin Design: Photograph of a manufactured plate featuring the pin-fin array. ....	47
3.15 Schematic of full-design simulation boundary conditions. ....	50
3.16 SCO2 Pin-Fin Design: Plot of mass flow rate for each pin gap at the inlet and outlet of the pin-fin array. ....	52
3.17 SCO2 Pin-Fin Design: Contour plot of temperature of the solid material at a cross-section of the device midway along the length of the pin-fin array. ....	53
3.18 SCO2 Circular Channel Design: Exploded view of the design. Blue arrows show the path of the cold fluid and red arrows show the path of the hot fluid. Yellow arrows show the direction of the solar flux. ....	55

LIST OF FIGURES (Continued)

<u>Figure</u>	<u>Page</u>
3.19 SCO2 Circular Channel Design: Top wire-frame view. Blue arrows show the path of the cold fluid and red arrows show the path of the hot fluid. ....	56
3.20 SCO2 Circular Channel Design: Photograph of assembled device prior to welding of the three parts and inlet and outlet tubes. ....	57
3.21 SCO2 Circular Channel Design: Plot of mass flow rate for each individual channel. ....	59
3.22 SCO2 Rectangular Channel Design: Exploded diagram of the three plates. Blue arrows show the path of the cold fluid and red arrows show the path of the hot fluid. Yellow arrows show the direction of the solar flux. ....	61
3.23 SCO2 Rectangular Channel Design: Top wireframe view. Blue arrows show the path of the cold fluid and red arrows show the path of the hot fluid. ....	62
3.24 SCO2 Rectangular Channel Design: Photograph of a manufactured microchannel plate. ....	63
3.25 SCO2 Rectangular Channel Design: Contour plot of temperature of the solid at a cross-section midway along the channels. Flow is into the page and solar flux is indicated by the yellow arrows. ....	65
3.26 SCO2 Rectangular Channel Design: Plot of mass flow rate for each individual channel. ....	66
4.1 MS Rectangular Channel Design: Exploded view showing the design without the middle header plate. Blue arrows show the path of the cold fluid and red arrows show the path of the hot fluid. Yellow arrows show the direction of the solar flux. ....	69
4.2 MS Rectangular Channel Design: Top wire-frame view. Blue arrows show the path of the cold fluid and red arrows show the path of the hot fluid. ....	70
4.3 MS Rectangular Channel Design: Contour plot of temperature of the solid at a cross-section midway along the channels. Flow is into the page and solar flux is indicated by the yellow arrows. ....	73

LIST OF FIGURES (Continued)

<u>Figure</u>	<u>Page</u>
4.4 MS Rectangular Channel Design: Plot of mass flow rate for each individual channel (difference between inlet and outlet due to error in post-processing, description in text). . . . .	74
4.5 MS Pin-Fin Design: Diagram showing one end of the single channel geometry. This is the fluid volume. . . . .	75
4.6 MS Pin-Fin Design: Plot of mass flow rate through individual pin-fin gaps at three locations along the microchannel array. A gap is the flow area between two adjacent pin-fins. Data is from a full-design CFD simulation. . . . .	78
5.1 Cross-section of channel and surrounding solid showing the three grid resolutions. . . . .	80
5.2 Three-dimensional contour plot of heat flux at the fluid-solid interface for the SCO2 rectangular channel design. . . . .	81
5.3 Plot of heat flux versus grid size at a single point on the channel wall for the SCO2 rectangular channel design. . . . .	82
6.1 Diagram of experimental setup . . . . .	85
6.2 Plot of thermocouple measurements for “unheated” experiments versus average body temperature. . . . .	87
7.1 Fluid volume rendering of a branching channel header. The large cylindrical sections at the top are the global inlet and outlet tubes. The small parallel sections at the bottom are the microchannels. The inlet header channels are blue and the outlet header channels are red. . . . .	91
7.2 Cutaway view of the pin-fin header channel concept. Blue arrows indicate cold fluid, red arrows indicate hot fluid, and yellow arrows indicate solar flux. . . . .	92
A.1 Top-view diagram of a for a circular staggered pin-fin array with key dimensions. . . . .	96
A.2 Contour plot of maximum efficiency versus $K$ and emissivity. . . .	106
A.3 Plot of receiver temperature at maximum efficiency versus $K$ . . . .	107

LIST OF FIGURES (Continued)

<u>Figure</u>	<u>Page</u>
C.1 Plot of scaling factor required to match “heat loss curve” in simulation versus average body temperature.....	112

## LIST OF TABLES

Table	Page
1.1 Summary of goals and requirements for the receivers. ....	12
3.1 Parameters and results of full-design CFD simulation of the SCO2 pin-fin design. ....	51
3.2 Parameters and results of full-design CFD simulation of the SCO2 circular channel design. ....	58
3.3 Parameters and results of full-design CFD simulation of the SCO2 rectangular channel design. ....	64
3.4 Comparison of SCO2 Designs .....	67
4.1 Parameters and results of full-design CFD simulation of the MS rectangular channel design. ....	72
4.2 Results of MS pin-fin single channel simulations .....	76
4.3 Parameters and results of the full-design CFD simulation of the MS pin-fin design. ....	78
6.1 Experimental data and validation simulation results for SCO2 rectangular design.....	89
B.1 Properties of carbon-dioxide at 120 bar and at the inlet, average, and outlet temperature of the fluid. ....	108
B.2 Properties of Dynalene MS-1 at the inlet, average, and outlet temperature of the fluid. ....	109
B.3 Properties 316 Stainless Steel.....	109
B.4 Properties Haynes 214.....	110
B.5 Properties Haynes 230.....	110

*For my wife, Jessica.*

**NUMERICAL DESIGN OF A HIGH-FLUX  
MICROCHANNEL SOLAR RECEIVER**

# CHAPTER 1. INTRODUCTION

---

The following sections explain the purpose of the current work and explain the origin and significance of the goals and requirements for the receivers being developed.

## 1.1 Purpose

There are two categories of solar power technology: photovoltaic and thermal. Photovoltaic (PV) solar panels convert solar radiation directly to electric current using the photoelectric effect. In solar thermal power, solar radiation is converted to thermal energy that is then converted to mechanical energy and finally electricity. Commercial PV solar panels have efficiencies around 12-20% [1]. Solar thermal power plants have efficiencies around 16-23% [2]. A major issue for both forms of solar power is that peak production and peak demand occur at different times of day. Though methods exist for the storage of electrical power, they are expensive and inefficient. An advantage of solar thermal power is the ability to use thermal storage. With thermal storage, thermal energy is stored underground during times of excess production and then extracted when solar radiation decreases.

Solar thermal power is generally in the form of concentrated solar power (CSP). In CSP, reflectors concentrate solar insolation in order to achieve higher fluid temperature. Higher fluid temperature yields higher efficiency in the conversion from thermal to mechanical energy. The downside of higher fluid temperature is greater radiative losses from the receiver. This creates a trade-off between power

cycle efficiency and receiver efficiency as will be seen later in this section. Increasing the overall efficiency of CSP plants reduces the levelized cost of electricity (LCOE) of solar thermal power. Reducing the LCOE promotes increased investment and eventually a larger share in global power generation. The efficiency of a solar thermal plant can be defined as the ratio of electrical power produced to the available solar power. The receiver, where the concentrated solar radiation heats the working fluid, is one contributor to this efficiency. Figure 1.1 is an illustration of a solar power tower plant. Water is the working fluid in this illustration, but the principles are the same for any working fluid. The heliostats are mirrors that focus the sun's rays on the receiver. The fluid is heated in the receiver then flows through the turbine, which turns the generator. The fluid is then cooled and pumped back to the receiver.

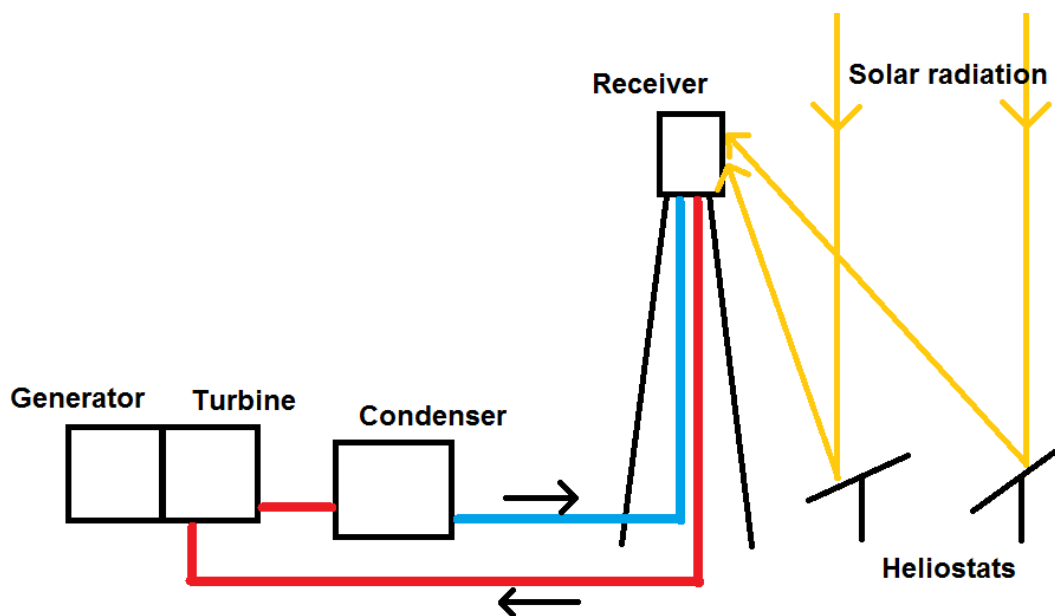


Figure 1.1: Illustration of a solar power tower plant.

The goal of this work is to demonstrate that microchannels, which generally

have a higher heat transfer coefficient than the technology currently used in CSP, can be used to increase the efficiency of the receiver. This is done using computational fluid dynamics (CFD) simulations and finite element analysis (FEA) for various designs. Current receiver technologies are macro-scale tube arrays and volumetric receivers, which pump fluid through a solid porous material. Tube receivers have efficiencies around 83% to 86% [3]. Volumetric receiver efficiency is typically between 60% and 80% [4].

Though the operating temperature considered in the following work is fixed, as will be described in section 1.3, it is helpful to examine the relationship between the temperature of the receiver, the receiver efficiency, the cycle efficiency, and the overall efficiency. We will use the Carnot efficiency as the cycle efficiency, though the real cycle efficiency will be much lower. For receiver efficiency, we consider losses due to re-radiation and reflection. The Carnot efficiency is

$$\eta_{\text{Carnot}} = 1 - \frac{T_C}{T_H} \quad (1.1)$$

where  $T_C$  is the cold sink temperature and  $T_H$  is the temperature of the receiver, which we will assume is close to the peak temperature of the working fluid. The receiver efficiency is

$$\eta_{\text{rec}} = \epsilon \left( 1 - K \left( \left( \frac{T_H}{T_C} \right)^4 - 1 \right) \right), K = \frac{\sigma T_C^4}{q''_{\text{inc}}} \quad (1.2)$$

where  $\epsilon$  is the emissivity of the receiver surface,  $\sigma$  is the Stefan-Boltzmann constant, and  $q''_{\text{inc}}$  is the incident solar radiation. A detailed derivation of this equation can be found in appendix A.3.4. The combined efficiency is simply the multiplication of the cycle efficiency and the receiver efficiency. Figure 1.1 is a plot of receiver

temperature versus Carnot, receiver, and overall efficiency. For this plot, the emissivity is one and  $K$  is  $4 \times 10^{-4}$ , which corresponds to a cold sink temperature of 293 K and an incident flux of approximately  $1 \text{ MW/m}^2$ . The Carnot efficiency is zero at  $T_H = T_C$  and increases asymptotically towards one as  $T_H$  increases. The receiver efficiency is one at  $T_H = T_C$  and decreases as  $T_H$  increases. The receiver efficiency goes negative at a temperature of about 2100 Kelvin (we will denote this as  $T_{H,2}$ ). At this point, more heat is emitted by the receiver surface than is incident. The maximum overall efficiency occurs at a receiver temperature between  $T_C$  and  $T_{H,2}$  (we will denote this as  $T_{H,1}$ ). Analysis of the effects of emissivity and  $K$  on the maximum efficiency and  $T_{H,1}$  can be found in appendix A.3.4.

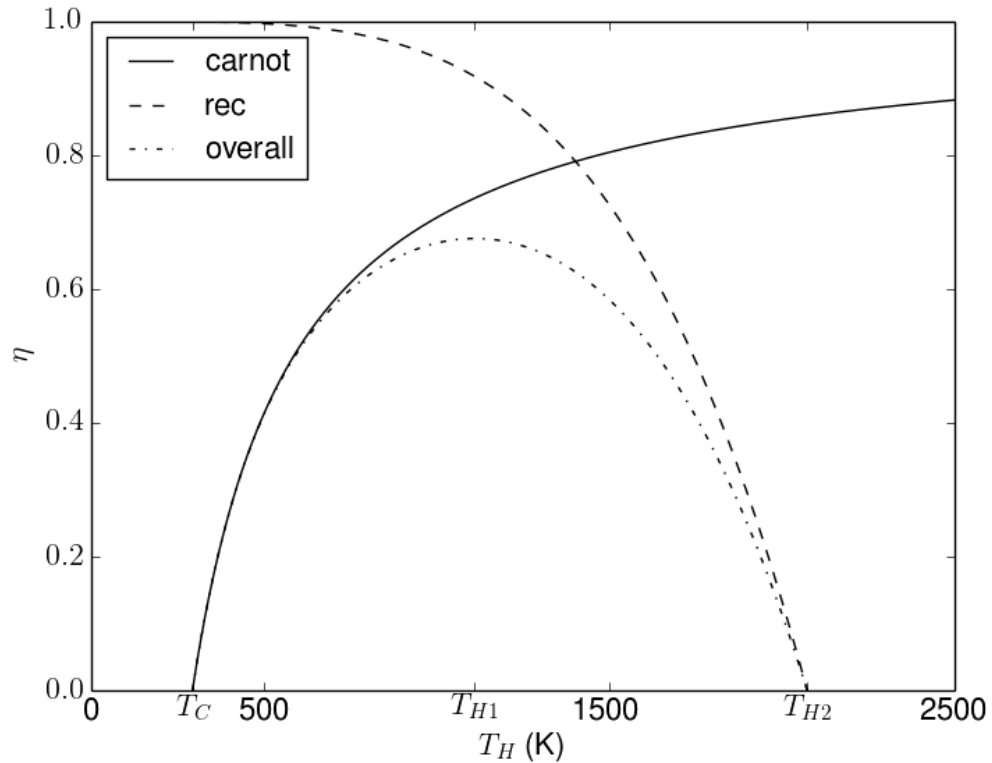


Figure 1.2: Receiver temperature versus Carnot, receiver, and overall efficiency.  $K = 4 \times 10^{-4}$ .

## 1.2 Goals

Receivers will be developed for two different working fluids: supercritical carbon-dioxide and molten salt. The following sections state the performance goals for each of these fluids as well as the general concept for receiver design.

### 1.2.1 *Supercritical Carbon-Dioxide as the Working Fluid*

Use CFD (Ansys FLUENT) simulations to develop a receiver using SCO<sub>2</sub> (supercritical carbon-dioxide) as the working fluid. SCO<sub>2</sub> is used because the supercritical Brayton cycle has shown potentially higher overall system efficiency than other power cycles [5]. The receiver efficiency (see appendix A.3.1) should be at least 90%. This value is the result of hand calculations and comparison with current technology. Ultimately, the goal of this work is to achieve as high a receiver efficiency as possible. Pressure drop through the device should be less than 0.35 bar. This value is also the result of hand calculations. It is necessary to have this goal in order to avoid excessive pressure drop when designing the receiver. Higher pressure drop in the receiver requires greater pumping power, leading to higher equipment cost and lower overall efficiency of the plant. The calculations used to determine the efficiency and pressure drop goals are discussed in section 1.3.4. Current CSP receiver technology is discussed in section 2.1.

### 1.2.2 *Molten Salt as the Working Fluid*

A receiver using MS (molten salt) as the working fluid will also be developed. Molten salt is used because it has high thermal conductivity, leading to high heat transfer coefficient [6]. It also allows for efficient thermal storage, a major advantage for solar thermal power over PV, as stated earlier. The receiver efficiency should be at least 95%. This value is the result of hand calculations and comparison with current technology. Pressure drop through the device should be less than 1.0 bar. This value is also the result of hand calculations. It is necessary to have this goal in order to avoid excessive pressure drop when designing the receiver. As stated in the previous section, these calculations and current CSP receiver technology are discussed in later sections.

### 1.2.3 *Receiver Concept*

Figure 1.3 shows a solid model of the general concept for a receiver. The device is rectangular with tubes extending from the bottom carrying inlet and outlet fluid. Solar flux is incident on the top surface of the receiver.

## 1.3 **Requirements**

### 1.3.1 *Requirements for Supercritical Carbon-Dioxide*

One of the working fluids been used is SCO<sub>2</sub>. The inlet and outlet temperatures for SCO<sub>2</sub> are 500 and 650 C (773 and 923 K). This requirement is based on the power cycle in the target application, as determined by the project sponsors.

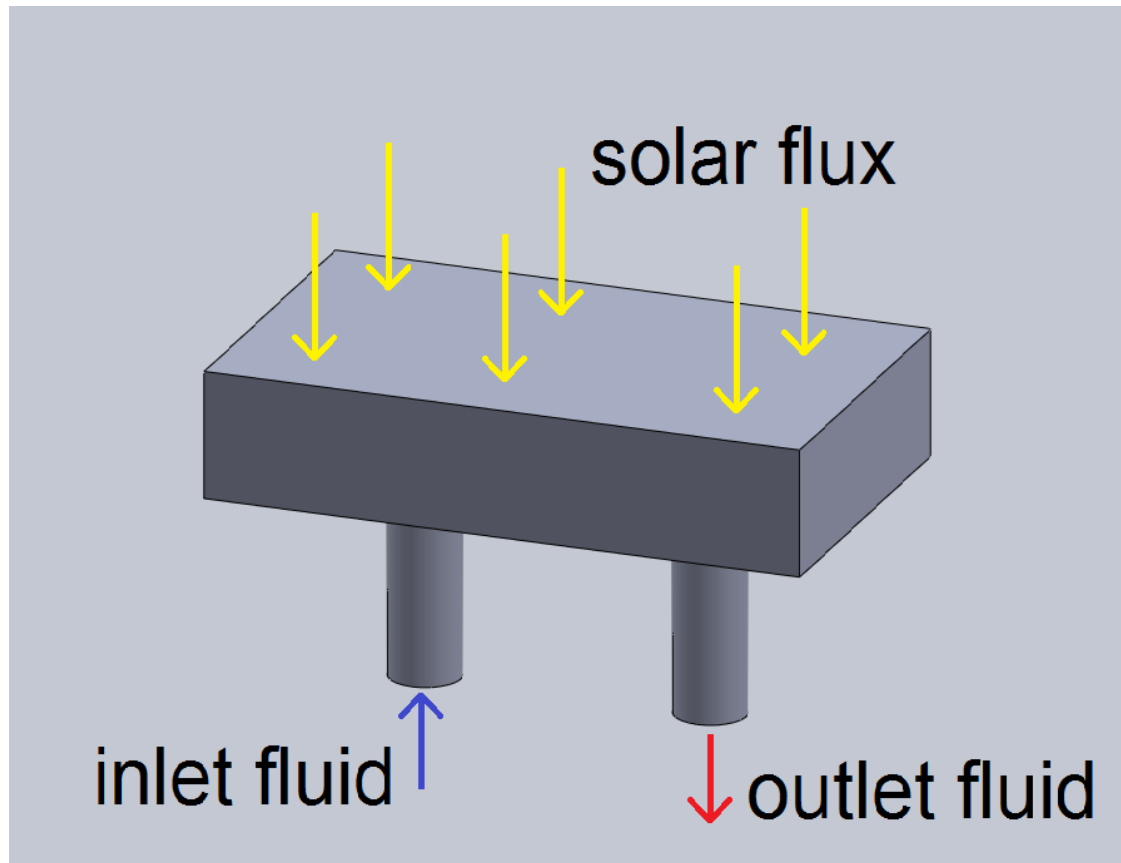


Figure 1.3: Solid model illustrating general concept for the receiver.

The temperature of the fluid must also remain well above the critical temperature of 304 K. The average incident solar flux is  $100 \text{ W/cm}^2$ . This value is the result of hand calculations and comparison with current receiver technology. The fluid operating pressure is 120 bar. As with the fluid temperature, this is determined by the power cycle. The pressure must also remain well above the critical pressure of 73.8 bar.

### 1.3.2 *Requirements for Molten Salt*

The second working fluid is MS, specifically Dynalene MS-1. The inlet and outlet temperatures of the MS are 300 and 600 C (573 and 873 K). This is chosen to cover the full working range of the fluid. Note that the molten salt chosen has a maximum temperature around 550 C [6]. By using a higher outlet temperature, we are anticipating the development of higher temperature salts in the future. The average incident solar flux is 400 W/cm<sup>2</sup>. This value is the result of hand calculations and comparison with current receiver technology. The fluid operating pressure is 10 bar. This value is based on the pressure in the molten salt loop, as determined by the project sponsors. This pressure depends on the details of the power tower implementation, therefore the value is an estimate.

### 1.3.3 *General Requirements*

Flow through the microchannel array must be adequately distributed. This avoids hot-spots caused by regions with significantly reduced flow rate. The device must withstand the mechanical stress caused by the operating pressure of the fluid and thermal stress from temperature gradients in the solid material. Mechanical stress is more of an issue in the SCO<sub>2</sub> devices because of the higher operating pressure of the fluid. Thermal stress is more of an issue in the MS devices because of the higher solar flux and therefore higher temperature gradients.

Manufactured devices are tested using a solar simulator built at MBI (Microproducts Breakthrough Institute). The simulator consists of a lamp focused by an aluminum reflector. The size of the microchannel array depends on the output

capability of solar simulator. Details of these experiments are beyond the scope of this work. However, these experiments are discussed in the section on validation of simulation results (section 6). At the time of writing, experimental work has not yet been completed for all of the designs presented in this thesis.

To ensure that the designs can be applied to larger scale implementations in future work, at least one design for each fluid must be scalable. Also, a concept must be developed for a 1 m<sup>2</sup> receiver panel (see section 7).

### 1.3.4 Calculations

Hand calculations are used to calculate some of the goals and requirements for the two working fluids. These calculations estimate the heat transfer and pressure drop in hypothetical microchannels.

The goal of heat transfer equations is to estimate the exterior temperature of a receiver. This exterior temperature is used to estimate the receiver efficiency, see appendix A.3. Two processes determine this temperature: convection in the microchannel and conduction through the solid material. Convection in internal flow (channels) and conduction are discussed in appendices A.2.4 and A.2.4. The temperature difference from the bulk fluid to the exterior of the device is

$$T - T_{\text{bulk fluid}} = \frac{q}{hA_{\text{chan sur}}} + \frac{q\Delta x}{k_s} \quad (1.3)$$

Fully-developed pressure drop for flow in a duct is

$$\Delta p = f \frac{L}{D_h} \frac{\rho v^2}{2} \quad (1.4)$$

where  $f$  is Darcy friction factor,  $L$  is channel length,  $D_h$  is hydraulic diameter,  $\rho$  is density and  $v$  is average velocity. Methods for determining friction factor depend on the shape of the channel and the nature of the flow (laminar or turbulent). This is discussed in more detail in appendix A.2.3.

Using these equations and the requirements set by the project sponsors, the authors of the initial proposal for this work determined appropriate values of goals and requirements such as pressure drop and incident solar flux. These values are unique to this work because of the combination of the use of microchannels in CSP and the working fluids being used. This unique combination of parameters has not yet been researched, likely due to the fact that CSP is a relatively young technology and the technical challenges associated with using microchannels in a CSP application. These challenges are discussed in later sections.

The difference in the requirements for the two working fluids comes from the difference in fluid properties. Most significant are thermal conductivity and density. Thermal conductivity affects the heat transfer coefficient in the convection heat transfer equation. Density affects the pressure drop equation directly and through the velocity term.

### 1.3.5 *Summary*

Table 1.1 presents the various goals and requirements for the receivers.

	Fluid	
	supercritical carbon-dioxide	molten salt
Inlet temperature (K)	773	573
Outlet temperature (K)	923	873
Incident flux ( $\text{W}/\text{cm}^2$ )	100	400
Receiver efficiency (%)	90	95
Pressure drop (bar)	0.35	1.0
Operating pressure (bar)	120	10
Additional requirements	flow distribution structural integrity scalability	

Table 1.1: Summary of goals and requirements for the receivers.

## CHAPTER 2. LITERATURE REVIEW

---

### 2.1 Review of Power Tower Technology

In current power tower technology, incident flux on the receiver ranges from 300 to 1000 kW/m<sup>2</sup> [2, 3]. On average, insolation on a surface perpendicular to the sun's rays is approximately 1000 W/m<sup>2</sup>. At different locations on the earth, this value decreases based on distance from the equator and weather. Therefore the above values for receiver flux correspond to concentration factors of 300 to 1000. Common types of receivers are tube receivers and volumetric receivers [3, 4].

Tube receivers consist of arrays of parallel macro-scale circular tubes. Heat is absorbed by the exterior walls of the tubes, conducted through the tube walls, then absorbed by fluid flowing through the tubes. These receivers are the simplest in construction of the receiver types presented here. Tube receivers have efficiencies around 83% to 86%. Figure 2.1 shows a simple illustration of a tube array.

Volumetric receivers use a porous material contained in a structure to absorb the solar radiation. The heat is then transferred to a fluid that flows through the porous material. Figure 2.1 shows an illustration of a volumetric receiver. In some volumetric receivers, including the type shown in the figure, one face of the porous material is open to the environment and the working fluid is air. Air from outside the receiver is pulled through the porous material, absorbing heat. Volumetric receiver efficiency is typically between 60% and 80%.

Still in development are falling particle receivers [7]. In these receivers, a

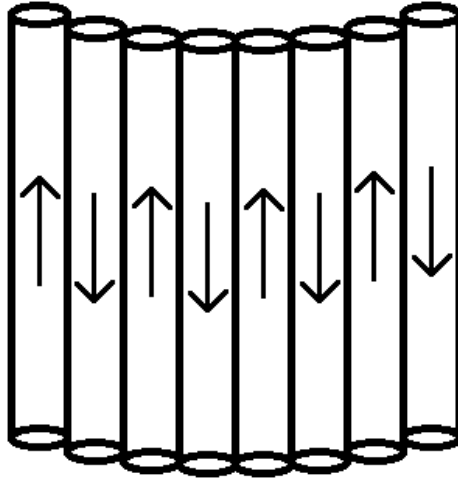


Figure 2.1: Illustration of a tube array used in a tube receiver.

continuous sheet of solid particles, fed by a bucket elevator and a hopper, falling inside the tower absorbs the solar radiation. The heat is then extracted from the particles. The solid particles can be heated to temperatures higher than the stability limit of molten salts. And, like molten salt, the solid particles would enable efficient thermal storage. Figure 2.1 shows a schematic of a solid particle receiver.

Probably the most notable historical example of power tower plants are the Solar One and Solar Two plants. Solar Two was actually a retrofit of Solar One. These experimental plants operated during the 1980's and 90's [3]. The receiver for these plants was a tube array composed of 20 to 80 mm diameter thin-walled tubes. Solar One used water/steam as the working fluid and Solar Two used molten salt. Since then, many commercial power tower plants have become operational.

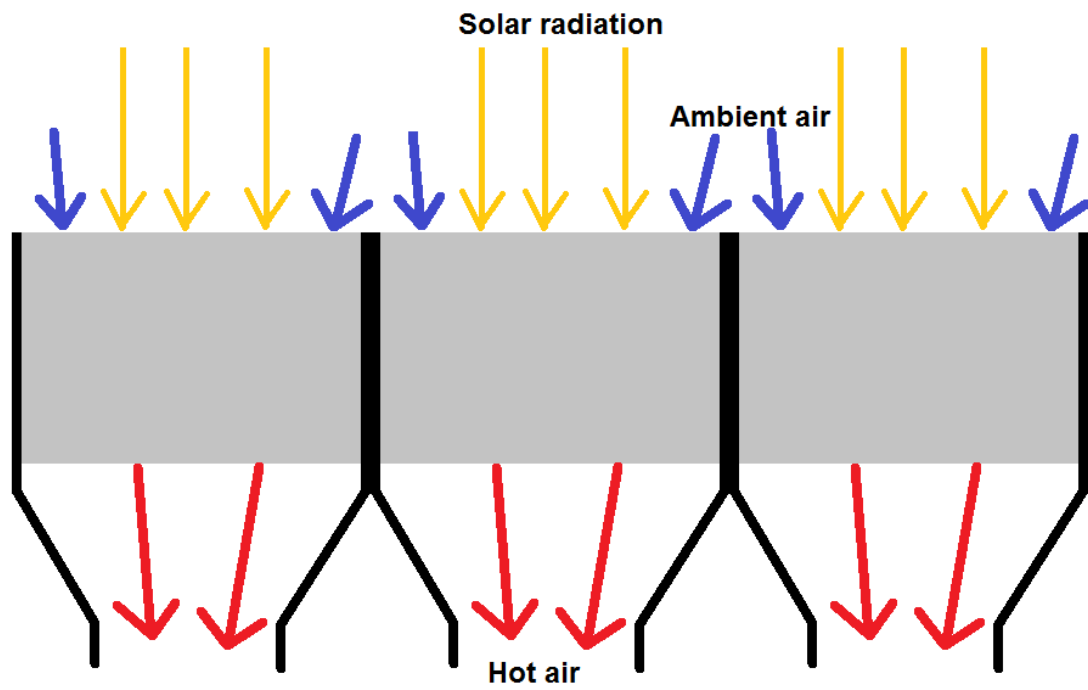


Figure 2.2: Illustration of a volumetric receiver.

Examples include Spain's first commercial plants: PS10, PS20, and Gemasolar [4].

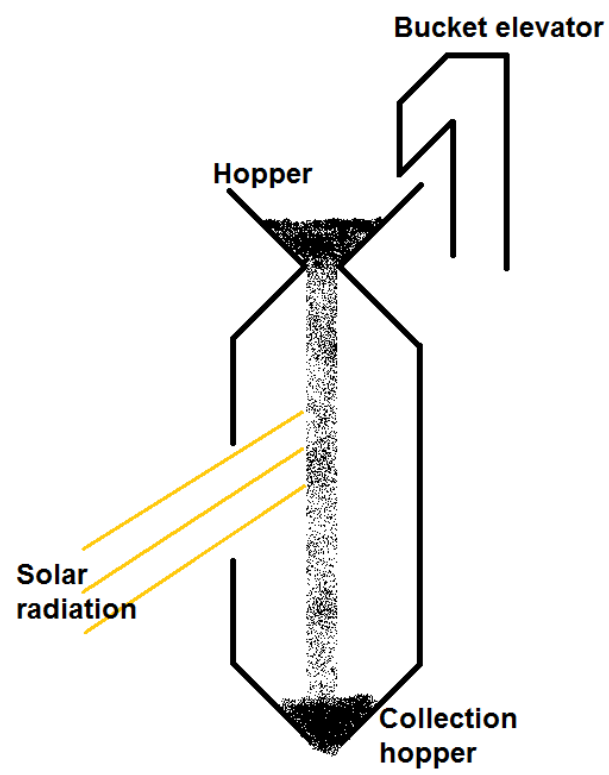


Figure 2.3: Schematic of a solid particle receiver.

## 2.2 Review of Working Fluids

### 2.2.1 Super-critical Carbon-Dioxide

A supercritical fluid is a substance at a temperature and pressure above the critical point. The substance exhibits properties of both gas and liquid. Figure 2.2.1 is a phase diagram for carbon-dioxide showing the supercritical phase.

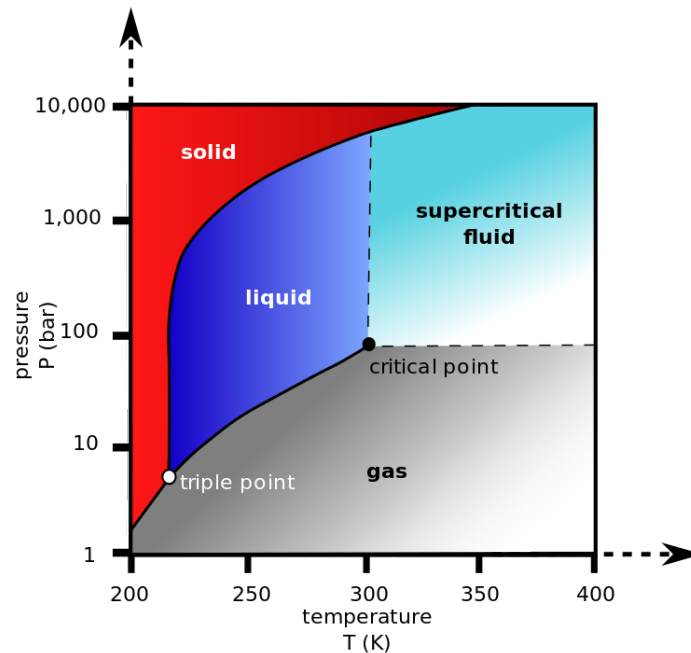


Figure 2.4: “Carbon dioxide pressure-temperature phase diagram” by Ben Finney, Mark Jacobs. Licensed under CC0.

Supercritical carbon-dioxide has been used extensively as an industrial solvent. Only relatively recently has it been used as the working fluid for a Brayton power cycle [8]. The motivation is potentially higher cycle efficiency resulting from the unique properties of a supercritical fluid.

### 2.2.2 *Molten Salt*

Molten salts have been used in power tower plants in the past; for example in the Solar Two plant in California [3]. These fluids have high density and high thermal conductivity, making them effective heat transfer fluids. They are also non-toxic, relatively inert and have relatively low cost and good commercial availability. These properties also make molten salt attractive for plants using thermal storage. The capacity for thermal storage is a major advantage of solar thermal power over PV solar power. However, since molten salt solidifies at room temperature, special procedures and equipment are needed for start-up and shut-down.

## 2.3 **Review of Microchannel Technology**

Since Tuckerman and Pease introduced microchannels for use in electronic cooling [9], the technology has been used in many other heat dissipation applications. The primary advantage of microchannels is higher heat transfer coefficient that leads to lower temperature difference between the channel walls and the fluid. The increased heat transfer coefficient is due to decreased diffusion length compared to macro-scale channels. The lower temperature difference leads to lower surface temperature for solar receivers. This decreases losses to the environment and increases efficiency. It can also allow for increased heat flux on a solar receiver, which allows for reduced receiver size and cost. Finally, from a structural standpoint, smaller channels allows for thinner walls. Thinner walls results in lower conduction resistance and lower receiver surface temperature, which further increases efficiency.

The primary disadvantage is higher pressure drop and pumping power than macro-scale channels. The power required to pump the working fluid subtracts from the net power generated, decreasing efficiency. Also, using microchannels results in a much greater number of channels for a given receiver area. This increases the complexity of the receiver.

Equations for heat transfer and pressure drop are needed in order to predict appropriate channel dimensions for our application. Correlations and analytical solutions from literature are used. Both rectangular channel and various pin-fin configurations are considered. Shah and London [10] give relationships between Fanning friction factor and Nusselt number in rectangular channels of any aspect ratio for laminar flow. In turbulent flow, an estimate for friction factor and Nusselt number can be found by using the hydraulic diameter with correlations for circular tubes.

The use of pin-fins in microchannel heat exchanger configurations has been studied and reported extensively in literature [11, 12, 13, 14, 15, 16, 17, 18, 19]. Pin-fin arrays have been shown to have substantially better combined heat transfer and pressure drop characteristics than straight channels, owing to increased surface area and disruption of boundary layers.

Many possible configurations exist for micro pin-fins. Sahiti et. al. studied various pin-fin shapes including circular, square and ellipse [17]. Moores et. al. studied the effect of varying pin-fin tip clearance [13]. Chiang et al. investigated using a jet impinging on the top of an open pin-fin array [20]. Most simple configurations can be divided into aligned or staggered arrays. More complicated configurations can include non-uniform or random arrangements and/or configurations in which pin size and shape vary along the length or width.

This work focuses on using an array of circular pin-fins in a uniform, staggered

arrangement. This is a simple and effective configuration seen often in literature. Correlations from literature are needed for the friction factor and Nusselt number for this pin-fin configuration. Unfortunately, there is considerable disagreement on the friction factor and heat transfer coefficient correlations between the numerical and experimental results from various authors [11]. Also, for the SCO<sub>2</sub> designs, literature pertaining to micro-pin-fin arrays involves significantly lower Reynolds numbers than are involved in the current research.

## CHAPTER 3. SUPERCRITICAL CARBON-DIOXIDE DESIGNS

---

Design of SCO<sub>2</sub> receivers is discussed in the following sections. The first five sections discuss aspects of the design that must be dealt with before designing a complete receiver. The next three sections present three complete receiver designs. The conclusion summarizes the key characteristics of these designs.

### 3.1 Limitations of Manufacturing Processes

The limitations of two manufacturing methods are discussed in the following sections.

#### 3.1.1 *Chemical Etching*

At the beginning of this project, it was decided that chemical etching should be used to manufacture the microchannels. In chemical etching, you start with a (usually thin) sheet of material. A mask is applied to one side of the sheet. The mask covers the areas of the sheet which should not be etched. Acid is applied to the masked side of the sheet, dissolving material to form channels. The length of time for which the material is exposed to the acid determines the depth of the etch. The mask is removed and the process is complete.

The first step in the design process is to consider the limitations associated with this manufacturing method. The type of etching to be used is isotropic

etching, in which the material is submerged in a tank of acid. This means that the material is etched equally in all directions. Consequently, the maximum depth of any etched feature is twice the width. It was decided that microchannels could be etched in two halves in separate plates then bonded together, effectively doubling the depth of the microchannels.

An isotropic etch also means that etched features will have rounded, instead of sharp, corners and edges. For example, if one were to etch a straight slot of greatest possible depth, the slot would have a semi-circular cross-section. Figure 3.1 is a simple diagram of a cross-section of a sheet of material at three stages in the isotropic etching processes.

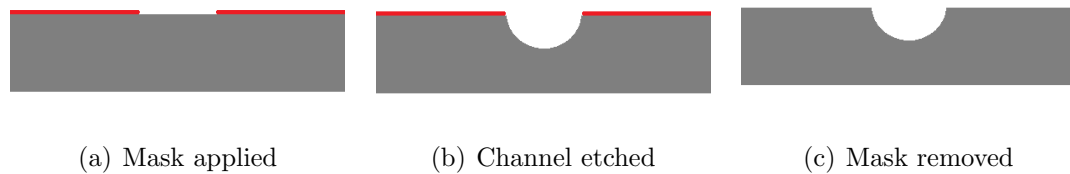


Figure 3.1: Cross-section of a sheet of material at three stages in the isotropic etching process. Gray is the solid material and red is the mask.

### 3.1.2 *Diffusion Bonding*

Another decision was to use diffusion bonding to join the sheets of metal that form the device. Diffusion bonding is a solid-state welding process in which two parts (at least one of which is metallic) are joined by heating and applying external pressure. Elevated temperature allows the metal to deform at a molecular scale and fill in the microscopic gaps between the materials. When using the same metal for both parts, the bond can be indistinguishable from the parent material. Diffusion bonding is ideal for microchannel devices because the process works at

practically all scales.

There are two concerns when using diffusion bonding to bond sheets of metal to form microchannel devices. The first is the uniformity of the thickness of the sheets. If a sheet has a region that is sufficiently thinner than average, this region may not come in contact with the adjacent sheet and not bond. In a microchannel device, this could cause structural failure and leakage.

The second concern is transfer of the external pressure applied during the bonding process. If this pressure is not distributed evenly across the entire bonding interface, regions with lower pressure may not fully bond. An example of how this could happen is if the microchannel device is composed of multiple layers with channels in each layer. The external pressure will not be transferred through the open region which forms the channel. Figure 3.2 illustrates the issue. In this figure, there are three plates being bonded. The bottom and middle plates have channels etched in them. The bottom plate has one wide channel and the middle plate has four smaller channels. The external pressure is not transferred through the large channel in the bottom plate. Therefore, the pressure at the bonding interface near the smaller channels may be too small.

This issue could be investigated using FEA. However, for this work, the devices are designed to avoid this issue. This is done by not overlapping large channels and regions where bond strength is critical.

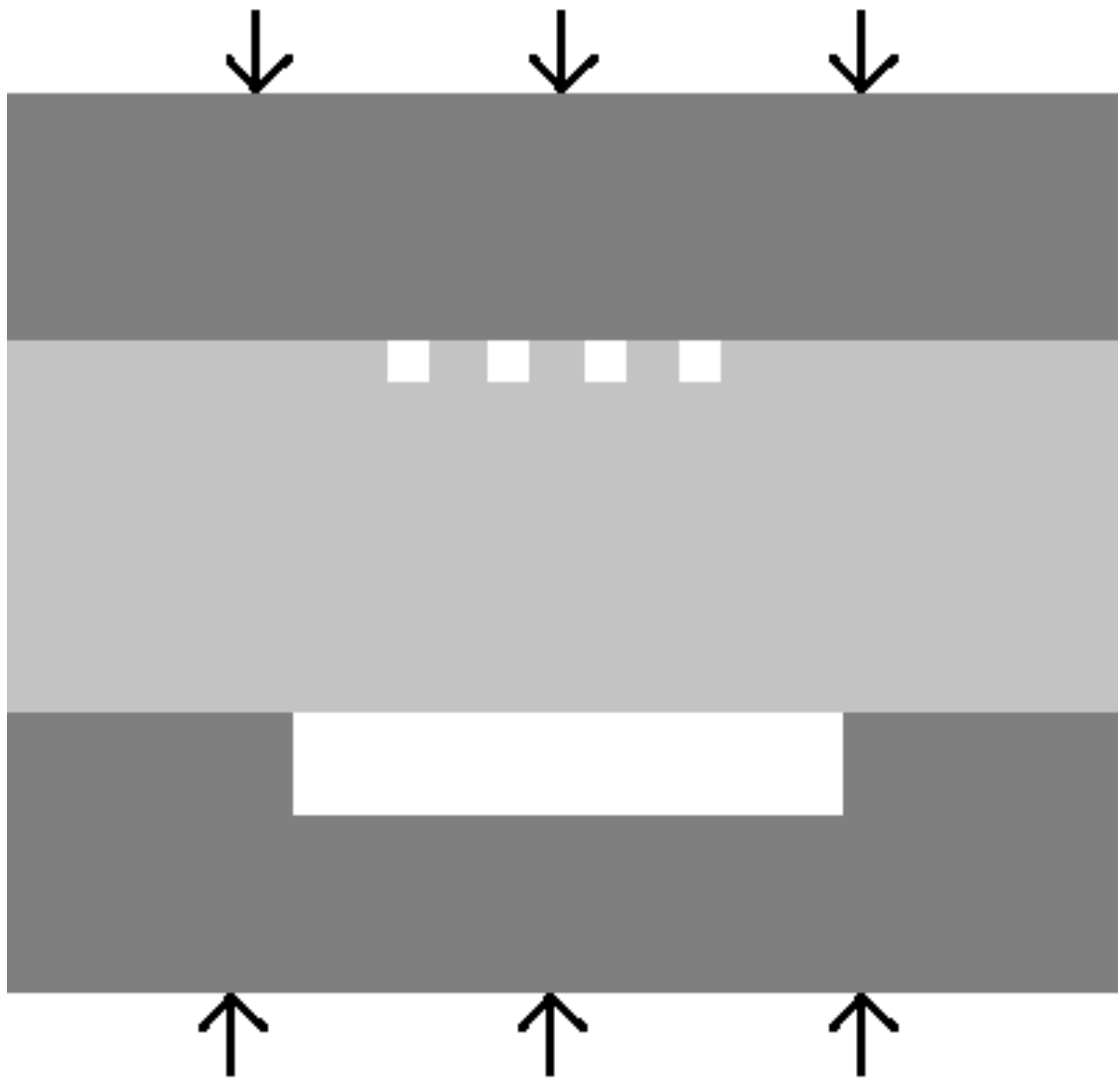


Figure 3.2: Cross-section of a microchannel device composed of three sheets. The white open regions are the channels. The arrows represent the external pressure used in diffusion bonding.

## 3.2 Single-Channel Simulations

The following sections discuss CFD simulations used to determine the optimal channel configuration and dimensions before beginning the design of a complete receiver.

### 3.2.1 Introduction

The second step in the design process is to determine whether to use a constant cross-section rectangular channel or a pin-fin array. Figures 3.3 and 3.4 illustrate the concept for these two types of channel. To do this, CFD simulations are used to compare pressure drop and temperature profile.

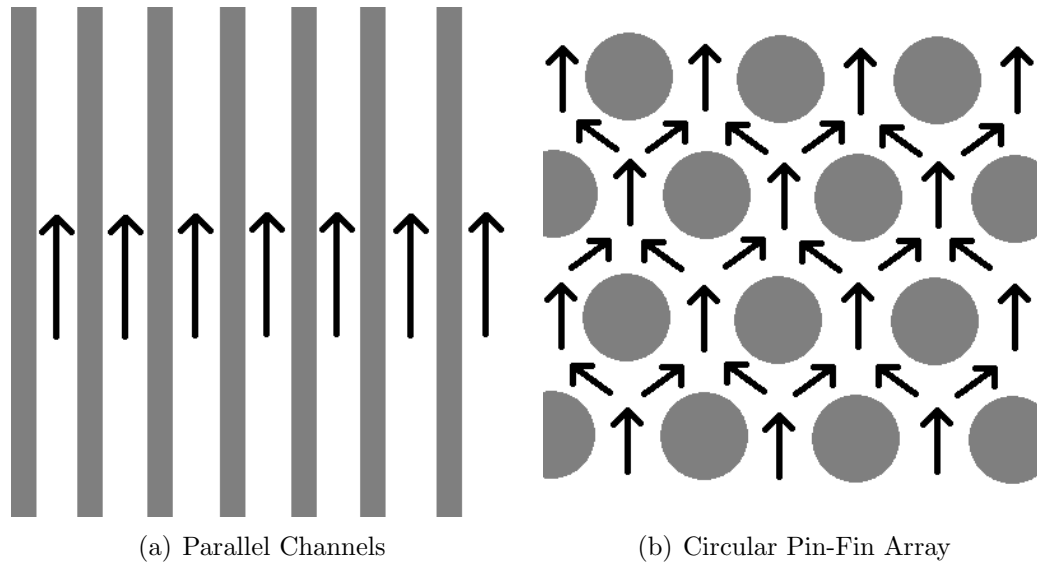


Figure 3.3: Topview of two sample channel concepts: parallel channels and a circular pin-fin array. Gray represents the solid material, white is the channel, and the arrows represent the direction of fluid flow.

Multiple pin-fin array configurations are considered. These include circular and square pins and staggered and aligned arrays.

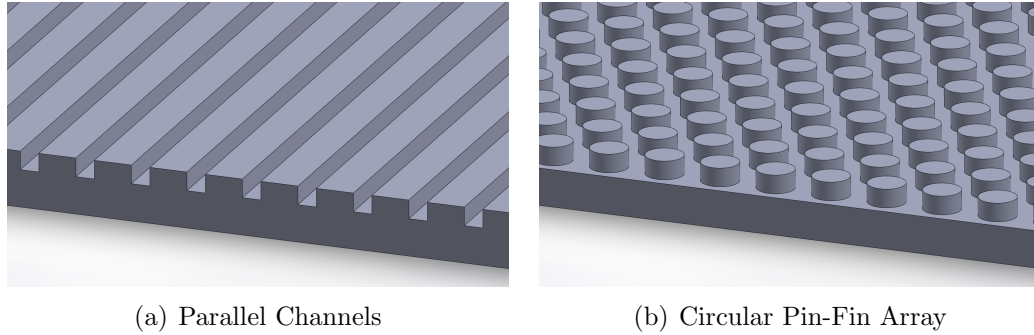


Figure 3.4: Solid models illustrating two sample channel concepts: parallel channels and a circular pin-fin array.

### 3.2.2 *Channel Parameters*

For the channel dimensions, a starting point is needed in order to begin CFD analysis. These initial parameters are determined using hand calculations similar to those described in 1.3.4. The length of the microchannels is determined based on the capabilities of the solar simulator which is used to test the manufactured devices. The width and height of the channels, number of channels, and other parameters are determined based on hand calculations.

At first, rectangular channels with high aspect ratio (depth to width ratio) were considered. High aspect ratio channels have the advantage of lowering pressure drop and increasing surface area for heat transfer, while maintaining a small diffusion length. In order to estimate heat transfer in these channels, fin analysis was used. Fins, in this case, refer to heat-transfer enhancement features in external flow, such as fins on a heat sink. The analysis takes into account the decrease in temperature from the base to the tip of the fin. This can be applied to a high aspect ratio channel. The fins, in this case, are the walls between the channels. As you move away from the heated surface of the receiver, the channel wall temper-

ature decreases and the heat transfer rate to the fluid also decreases. The result is diminishing returns from making the channel deeper. If all other parameters are held constant, then increasing the channel depth decreases the average fluid velocity which then decreases heat transfer coefficient. There is, in this case, an optimal channel depth.

A range of values is chosen for the initial channel dimensions. For rectangular channels, initial channel dimensions based on these calculations have widths from 50 to 1000 micron, heights from 50 to 250 micron, and lengths from 0.7 to 2.3 cm. The Reynolds number for these channels ranges from 700 to 2500. For the pin-fin designs, the pin diameter ranges from 100 to 500 micron, and the transverse and longitudinal pitches are 1.5 or 2.0.

Later, it was learned that high aspect ratio channels could not be pursued due to manufacturing limitations which will be described in section 3.1.1. Channel designs were limited to low aspect ratio designs for both rectangular and pin-fin configurations.

### 3.2.3 *Setup*

For constant cross-section channels, the simulation geometry consists of a single channel and the surrounding solid material. For a pin-fin array, it consists of a section of the array one transverse spacing wide. All simulations features a small portion of header (hypothesized design of the header near the channels) to accurately model developing flow and the 90-degree turn from header to channel layer. Some simulations model the fluid only and others model both the fluid and solid domain. Simulations in which both solid and fluid are modeled are referred to as conjugate. In these cases, the CFD software automatically calculates heat

transfer across the interface between solid and fluid.

It is necessary to determine the flow regime for these simulations (laminar or turbulent). Determining the flow regime requires calculation of the Reynolds number. The Reynolds number requires information about the geometry of the channel as well as the mass flow rate. Mass flow rate depends on the fixed requirements of heat flux and fluid temperature as well as the overall size of the device. Section A.2.2 discusses in detail how the Reynolds number is calculated. The key unknowns in calculating the Reynolds number are the geometric variables. For the range of channel dimensions considered, the flow regime ranges from laminar to turbulent.

For those cases in which the flow is turbulent, a turbulence model to use in the CFD software needs to be chosen. In the Ansys software, several turbulent models are available. Two commonly used models for this type of application are K-epsilon and K-omega. These are Reynolds-averaged models and have a good balance of accuracy and computational cost. The K-epsilon model has better performance in external flow and the K-omega model has demonstrated better performance in near-wall regions with adverse pressure gradients [21]. Therefore, the K-omega model may be better suited to our application and is used in all SCO<sub>2</sub> CFD simulations in which the flow is turbulent.

These and future simulations are modeled as steady-state. It is possible that oscillations in the velocity field could exist in certain regions of the device, especially in a pin-fin design. However, it is expected that the effect of these oscillations on the time-averaged quantities of pressure drop and heat transfer are small.

The fluid is assumed incompressible but temperature dependent. Though the properties of SCO<sub>2</sub> are pressure dependent, the pressure drop through the device is

small enough that the effects are negligible. More information on fluid properties can be found in appendix B.

Initially, grid size is chosen based experience with CFD analysis. In the microchannels, the grid size is chosen in order to have a sufficient number of cells across the channel in order to resolve the velocity profile. The grid is also refined near the walls in order to resolve the velocity gradient near the wall. Later in the course of this work, grid convergence studies are conducted in order to estimate the error from insufficient grid resolution (see section 5). In rectangular channel designs, a structured grid can be used. This grid consists entirely of rectangular parallelepiped cells. Structured grids are less computationally expensive than unstructured grids both for grid generation and the CFD solver. For pin-fin designs, due to the complex shape of the array, unstructured grids must be used. Unstructured grids are generally composed of four, five, and six-sided irregularly shaped cells. Low quality cells are often created, which can lead to inaccuracy in the CFD solution. Two computer programs are used for grid generation: the grid generation software packaged with Ansys Workbench and Pointwise. Pointwise, with its scripting capabilities, was found to be useful for generating grids for simple geometries. The Ansys grid generation software was found to be more useful for complex geometries in which unstructured grids were used.

The exterior walls of the receiver (those not heated by solar radiation) are modeled as insulated, meaning no heat enters or exits the receiver through them. In experiments, these walls will be insulated and heat transfer through them should be small. It is impossible at this stage to accurately estimate how much heat will exit the receiver through these walls. A constant, uniform heat flux is applied to the heated surface of the device. Therefore, heat loss to the environment from the heated surface is not modeled in the simulation, but estimated as a post-processing

step. One advantage of using a constant heat flux input is direct control of the fluid inlet and outlet temperature. The inlet boundary condition is a constant velocity profile calculated using analytical solutions or empirical correlations depending on the flow regime. The turbulence values at the inlet are left at their default values in the CFD software. The inlet temperature is set to 773.15 K. The outlet is a constant pressure outlet of 0 Pa. Symmetry boundary conditions are used in both the rectangular channel and pin-fin configurations. For rectangular channels, the single channel is cut in half by a symmetry plane at the center of the channel. For the pin-fin array, two symmetry planes were used on either side of the geometry. The symmetry planes are aligned with the centers of the pins, cutting them in half. As a result of the chosen geometry, the recirculation regions behind the pins are also cut in half. The resulting recirculation patterns may be different than in reality.

Figure 3.5 shows a schematic of the boundary conditions for a single channel simulation. In this schematic, only the fluid volume is present. In some simulations, a region of solid material would also be modeled, making a conjugate simulation. A key difference between a fluid-only and conjugate simulation is that the solar flux would be incident on the solid material instead of the channel wall.

### 3.2.4 *Results*

The range of receiver efficiency for the configurations considered was fairly small: 88% to 91% . However, the results showed that the circular staggered pin-fin array had a slightly higher receiver efficiency for any given pressure drop. Since receiver efficiency generally increases with pressure drop, the channels should be designed to match the pressure drop goal for the desired channel length. Pressure

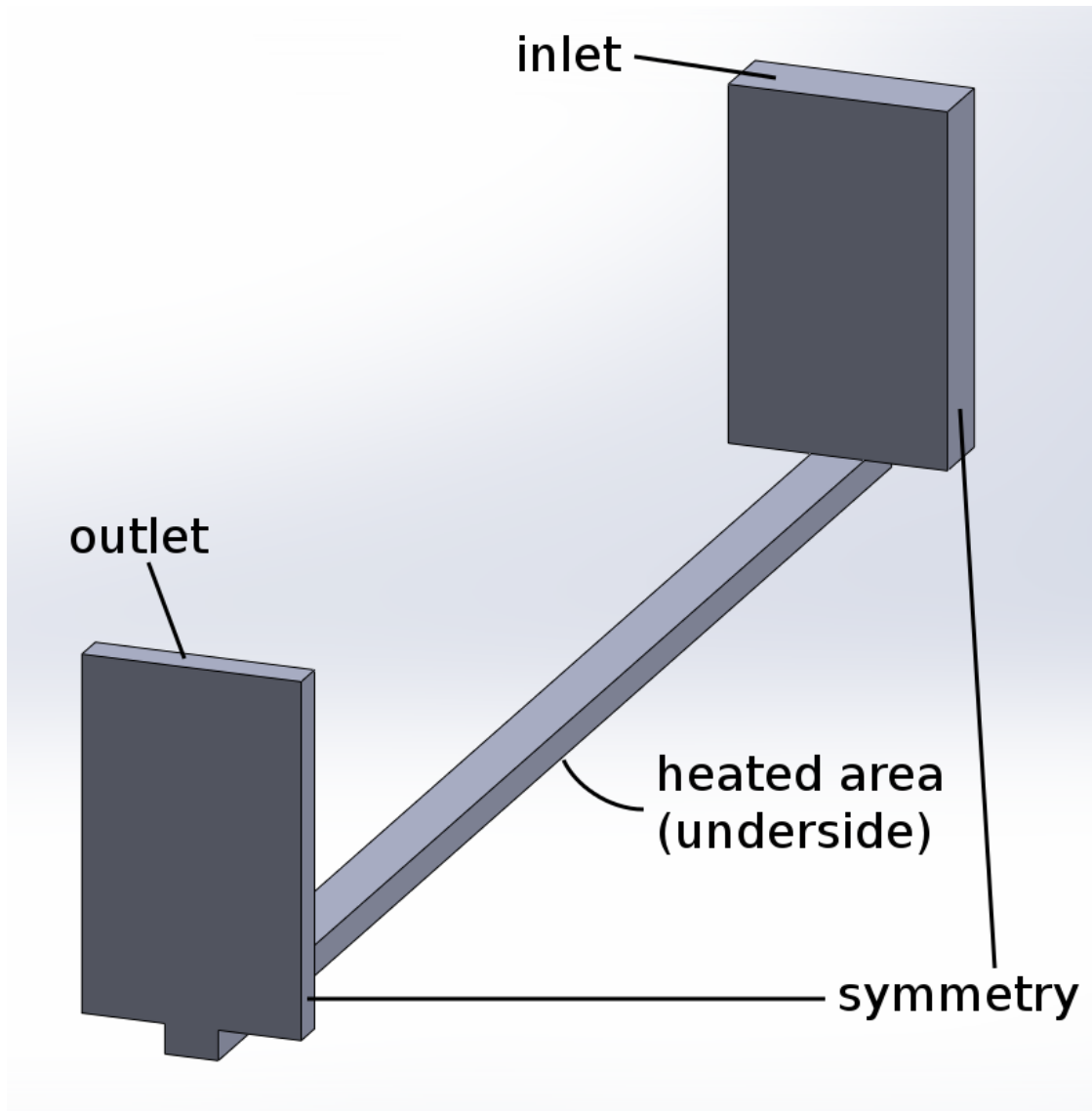


Figure 3.5: Schematic of single channel boundary conditions. Geometry shown is fluid volume; no solid material is shown.

drop was higher than predicted by hand calculations. The pin diameter was increased until a 1 cm long array met the pressure drop goal. A pin diameter of 700 micron matched the pressure drop goal for a 1 cm long array. This length is based on the capacity of the solar simulator (discussed further in section 3.6).

### 3.3 Structural Analysis of Pin-Fin Array

Before continuing with the design of a complete device, structural analysis of the pin-fin array is performed. Two-dimensional axis-symmetric FEA of a single pin is used. The purpose of this analysis is to determine the relationship between pin-fin dimensions (such as pin diameter and pitch) and stress in a single pin. Pressure equal to the operating pressure of the fluid is applied to the fluid-solid interface. Constant temperature and heat flux conditions are used to generate temperature gradients matching those observed in the CFD simulations in section 3.2. These temperature gradients create thermal stress.

The FEA shows that the dimension that determines the stress in the pin is the pitch (ratio of pin-fin spacing to diameter). Pitch determines the ratio of bonded area to unbonded area which is directly proportional to average stress in the pin. A pitch of 1.5 was found to result in a structural safety factor of 1.5. Figure 3.6 shows an example of a plot of von Mises stress from the FEA. The model is two-dimensional and axisymmetric. The left edge of the model is the centerline of the pin. The color scale is arbitrary; stress increases from blue to red. The highest stress occurs in the curved section.

Some simple equations can be used to support the result that the stress in the pins depends only on pitch. Average stress in a pin is given by

$$\sigma = \frac{(A_{\text{total}} - A_{\text{pin}}) P}{A_{\text{pin}}} \quad (3.1)$$

where  $A_{\text{total}}$  is the planform area associated with a single pin,  $A_{\text{pin}}$  is the cross-sectional area of that single pin, and  $P$  is the fluid pressure. The areas are given

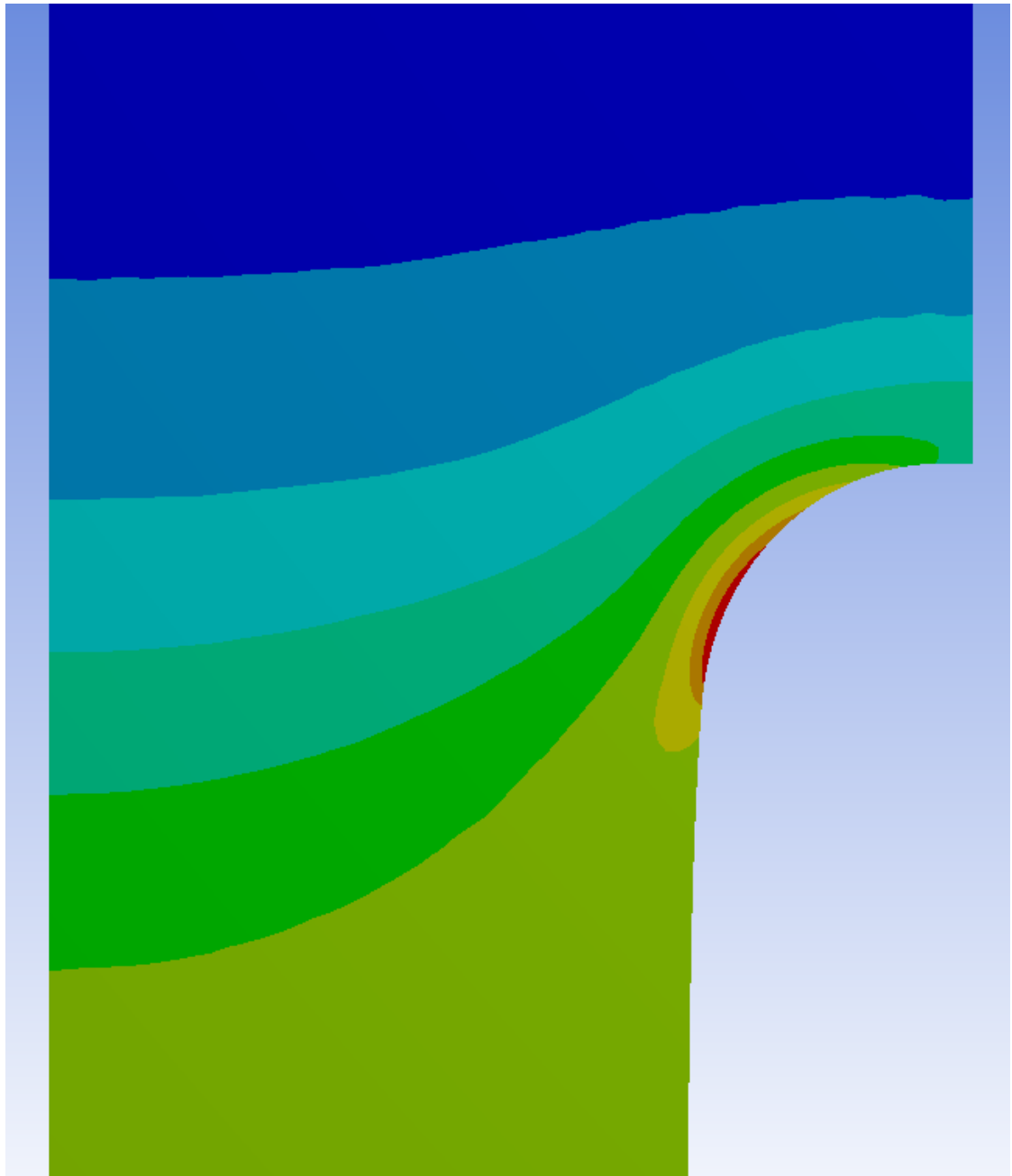


Figure 3.6: Contour plot of von Mises stress from FEA of a single pin. The model is two-dimensional and axisymmetric. The left edge of the model is the centerline of the pin. The color scale is arbitrary; stress increases from blue to red.

by

$$A_{\text{total}} = S_T S_L = P_T P_L D^2 \quad (3.2)$$

and

$$A_{\text{pin}} = \frac{\pi D^2}{4} \quad (3.3)$$

where  $S_T$ ,  $S_L$ ,  $P_T$  and  $P_L$  are the transverse and longitudinal spacing and pitch and  $D$  is the pin diameter. Substituting these into (3.1) gives

$$\sigma = \frac{\left(P_T P_L D^2 - \frac{\pi D^2}{4}\right) P}{\frac{\pi D^2}{4}} \quad (3.4)$$

$$= \frac{\left(P_T P_L - \frac{\pi}{4}\right) P}{\frac{\pi}{4}} \quad (3.5)$$

To get the maximum stress, we must consider the concentration factor caused by the transition between pin and channel wall. The maximum stress is given by

$$\sigma_{\text{max}} = C\sigma = f\left(\frac{a}{D}\right)\sigma \quad (3.6)$$

where  $C$  is the concentration factor and  $a$  is the radius of curvature of the transition.  $f$  represents an unknown function. The ratio can be simplified as

$$\frac{a}{D} = \frac{G}{2D} = \frac{S_T - D}{2D} = \frac{P_T D - D}{2D} = \frac{P_T - 1}{2} \quad (3.7)$$

We can see that the maximum stress depends only on pitch. This makes sense because, with the pitches fixed, all dimensions scale with diameter, resulting in no affect on the maximum stress.

### 3.4 Material Selection

One of the prerequisites to finalizing a design is selecting a solid material. The properties of the solid material must be known in order to perform conjugate CFD simulations and to calculate the structural safety factor.

Material selection is based on strength at temperature, ability to be chemically etched and diffusion bonded, cost, and availability. The factor of safety is used to determine if a material has sufficient strength. Factor of safety is calculated as

$$FOS = \frac{\textit{failurestress}}{\textit{appliedstress}} \quad (3.8)$$

The failure stress is the stress at which failure will occur. The applied stress is the maximum stress in the device. In high temperature applications, such as a solar receiver, creep strength is used as the failure stress. Creep strength will be used in the present work. Creep strength deals with the plastic deformation (and eventually failure) over long periods of time. This deformation is accelerated by high temperature. A typical creep strength value would be the stress required for a given percentage of deformation (or failure) at a given temperature in a given amount of time. For example, the stress required to produce 2% elongation in 100 hours at 700 C. In the present work, the failure stress is the stress to produce failure in 1000 hours at a temperature equal to the maximum temperature in the solid material.

SS (Stainless steel) was considered because it can be etched and bonded and has been used in similar microchannel applications. However, SS does not have sufficient strength at high temperature. Instead, refractory metals produced by Special Metals and Haynes were considered. The first criteria for selection was

creep strength at temperature. The second criteria was the ability to etch and bond the material. The first choice was Haynes 214. A manufacturer was found who has some experience chemically etching this alloy. Unfortunately, we were unable to purchase this alloy in small enough quantities. We settled on Haynes 230. Haynes 230 has similar high temperature strength to Haynes 214 and can be purchased in the small quantities needed for this project. However, there was uncertainty as to whether or not it could be chemically etched. As a result, additional receiver designs were developed which did not rely on chemical etching. These designs are discussed in a later section.

The relevant properties for these materials are presented in appendices B.3, B.4, and B.5.

## **3.5 Header Design**

The header channels carry fluid from the global inlet and outlet of the device to the microchannel layer. The following sections discuss the approach to the design of the header channels and the final design.

### *3.5.1 Introduction*

The design of the header channels is largely independent of the details of the microchannel design. The key pieces of information for designing header channels is the size of the microchannel array and the shape and location of the inlet(s) and outlet(s) to the microchannel layer. In all of the designs developed, the microchannel array is rectangular.

Depending on the desired length of the channels, two configurations of inlets and outlets to the microchannel array are considered. In the first, fluid enters and exits along opposite edges of the array. In the second, fluid enters through two regions at opposite edges of the array and exits through a common outlet between the two inlets.

For both configurations, the most obvious header solution is a header channel placed adjacent to each of the inlet(s) and outlet(s) of the microchannel array (perpendicular to flow in the microchannels). Figure 3.7 shows a three-dimensional wire-frame view of a complete device using the first configuration. The details of the header and channels will be discussed later; this figure is meant to explain the overall concept. Fluid enters through the large hole in the upper left, flows through the inlet header, into the microchannel array, into the outlet header, along the outlet header toward the large hole in the lower right, and finally exits the device. Figure 3.8 shows a three-dimensional wire-frame view of a complete device using the second configuration. The flow through the second configuration is very similar to the first.

### 3.5.2 *Original Header*

The original concept was to use a tall narrow header channel adjacent to the inlet and outlet of the array. The reason for the channel being narrow is that the flux plate (the plate in which the microchannels are etched) is thin. A wide header channel adjacent to this thin plate would cause failure in the flux plate. Since it is narrow, the header channel must be tall in order to have sufficiently low pressure drop.

Figure 3.9 shows a cross-section view of a microchannel device showing the

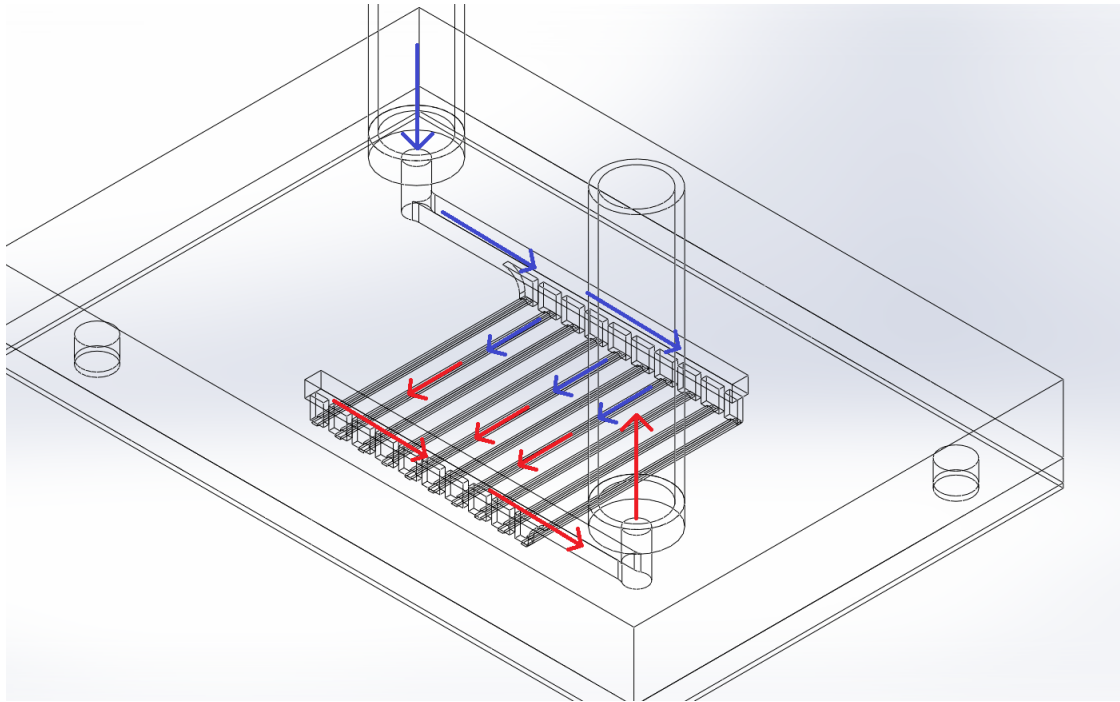


Figure 3.7: Three-dimensional wire-frame view of a header concept with one inlet and one outlet to the microchannel array.

original header concept. This cross-section is parallel to the microchannels and perpendicular to the header channels. In this diagram, the microchannels are horizontal and are indicated by the horizontal arrows. Solar flux is indicated by the yellow arrows. The two vertical open areas are header channels. The vertical area on the right is an inlet header and the area on the left is an outlet header. In this particular concept, there are two separate microchannel arrays placed side-by-side. There is an additional inlet header, to the left of the outlet header, which is not shown. One can see the flow from the two microchannel arrays converging on the outlet header. Flow in the header channels is not only vertical, as indicated by the arrows, but also into the page. The header channels run along the width of the microchannel array, connecting the inlet or outlet of each channel.

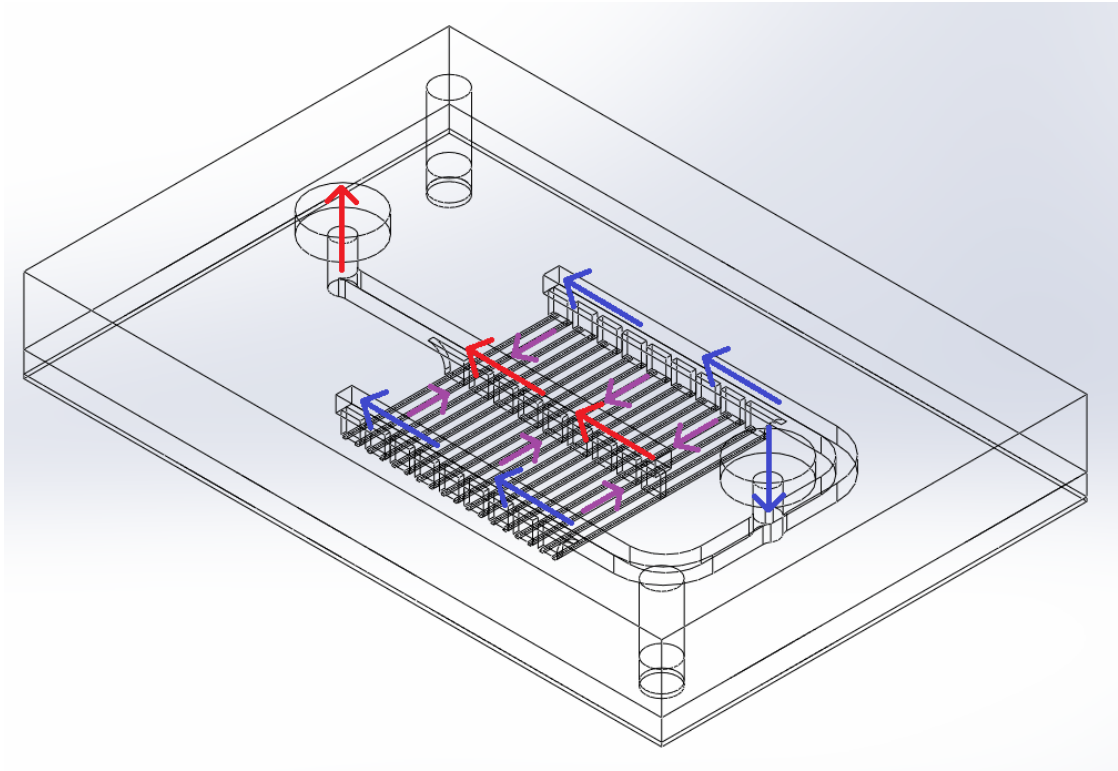


Figure 3.8: Three-dimensional wire-frame view of a header concept with two inlets and one outlet to the microchannel array.

Figure 3.10 shows a contour of von Mises stress from a two-dimensional FEA of such a slice. Due to the height of the header channels, the area of the side walls have substantial area. The resulting force pushes the walls of the header channel apart, causing high stress in the thin flux plate.

While performing this stress analysis, we encountered the issue of stress concentration at sharp interior corners in the model. These sharp corners occur in machined slots where the milling bit will presumably create sharp corners. In theory and in the FEA software, perfectly sharp corners result in infinite stress concentration [22]. In reality, a small curvature exists at these sharp corners which distributes the stress. In FEA, the issue is often dealt with by modeling that small

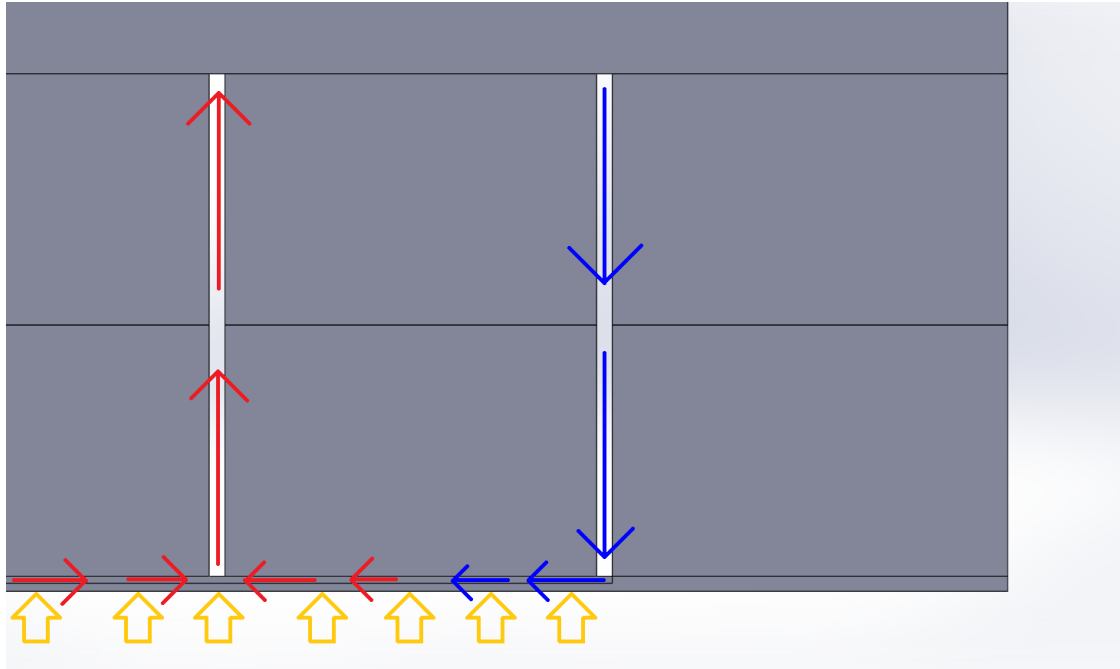


Figure 3.9: SCO<sub>2</sub> Header Design: Original header concept: Slice of a microchannel device showing an inlet and outlet header channel. Blue and red arrows indicate the direction of flow of cold and hot fluid. Yellow arrows indicate the direction of solar flux.

curvature. Determining an accurate value of this radius can be difficult given its extremely small size. Instead, a reasonable approximation is often used.

The radius of curvature used in this and future FEA was 5 micron. This is a reasonable approximation of the actual radius. Depending on which part of the receiver you are looking at, this is around 0.5-1.5% of the size of the channel.

Another way this can be dealt with is by modeling a sharp corner and modeling plastic deformation. The plastic deformation allows a realistic radius to naturally form in the FEA model. This method or accurate measurement of the actual radius may be used in future work.

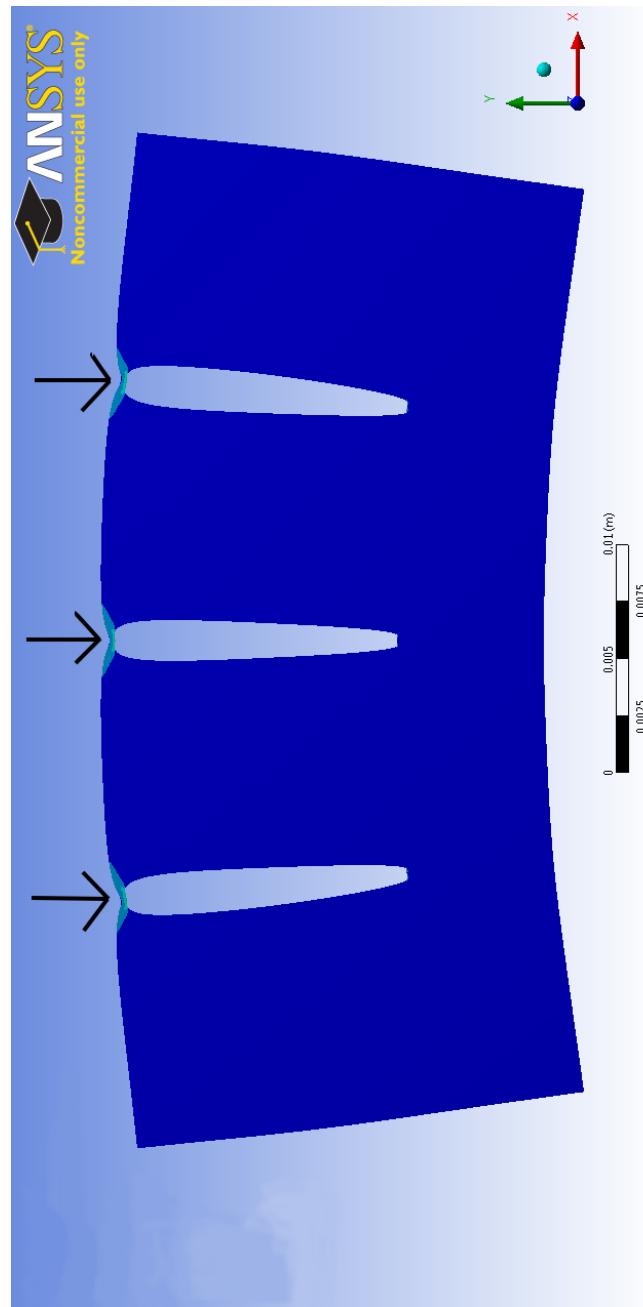


Figure 3.10: SCO<sub>2</sub> Header Design: Original header concept: Contour plot of von Mises stress with exaggerated deflection. The arrows point to the areas of highest stress. Blue indicates minimum stress and red indicates maximum stress. The exact values of stress in this plot are not of interest, only the locations at which high stress occurs.

### 3.5.3 Redesigned Header

Figure 3.11 shows a slice of a microchannel device showing the redesigned header concept. The header channel is split into two sections. The first is a narrow slot, but shorter than that in the original design. This slot is not continuous along the length of the header channel (along the width of the microchannel array). It is instead composed of several slots placed end-to-end along the width of the array (imagine a perforated sheet of paper). The extra solid material prevents the type of stress observed in the original design. Consequently, the first section of the header channel does not contribute significantly to flow distribution.

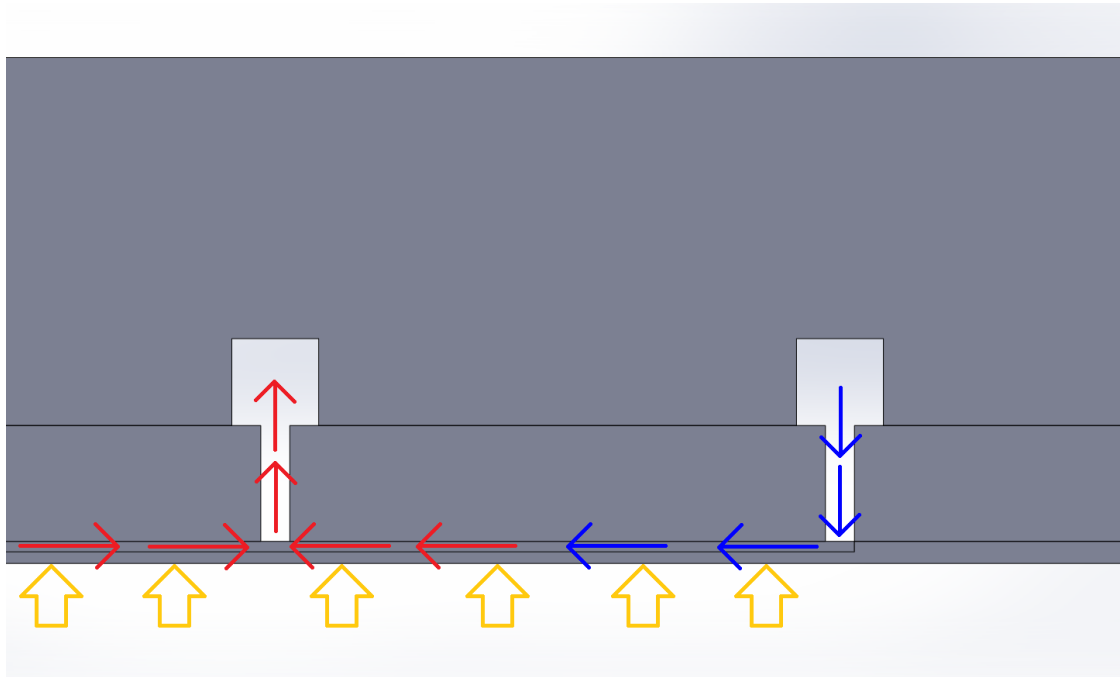


Figure 3.11: SCO<sub>2</sub> Header Design: Redesigned header concept: Slice of a microchannel device showing an inlet and outlet header channel. Blue and red arrows indicate the direction of flow of cold and hot fluid. Yellow arrows indicate the direction of solar flux.

The second section (the square area in the figure) is where the flow is distributed. This section is continuous along the width of the microchannel array. A

square is the optimal shape for reducing both pressure drop and mechanical stress (given the available manufacturing methods).

Three-dimensional FEA of one complete header channel was used to evaluate the stress in the header. The geometry in the analysis consists of one half of the device, but only one header channel is modeled; none of the microchannels are modeled. Figure 3.12 shows a contour plot of von Mises stress from this analysis, zoomed-in on the header channel. The highest stress occurs in the corners of the square section of the header channel.

Initially, stress in the square section was still too high, though less than that in the origin header design. The width of the square section was reduced until an acceptable stress was reached. A width of 1.2 mm resulted in a safety factor of 1.3. Though a higher safety factor is desirable, a smaller header channel results in flow maldistribution.

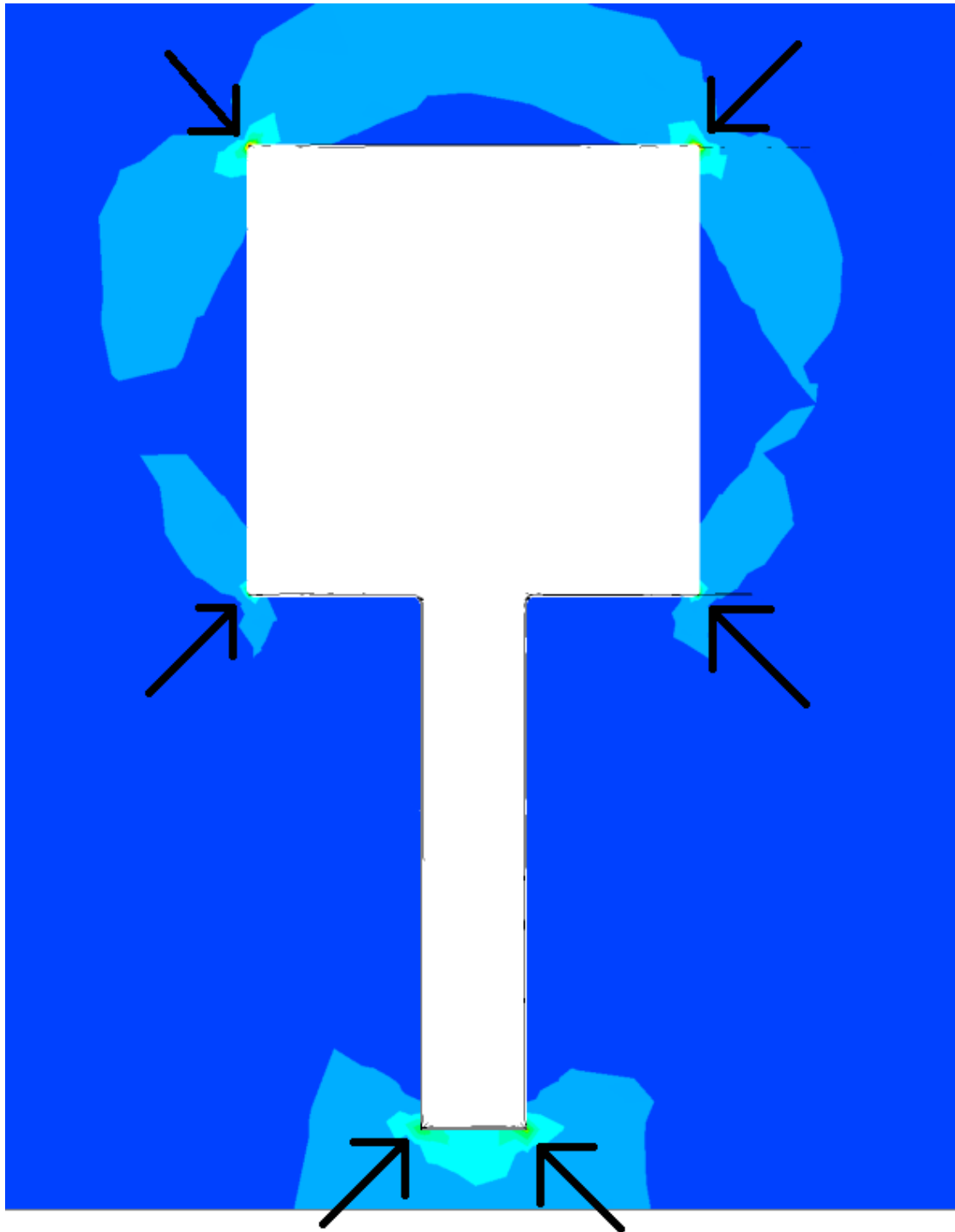


Figure 3.12: SCO<sub>2</sub> Header Design: Redesigned header concept: Contour plot of Von-mises stress. The arrows point to the areas of highest stress. Blue indicates minimum stress and red indicates maximum stress. The exact values of stress in this plot are not of interest, only the locations at which high stress occurs.

## 3.6 Pin-Fin Array

The following sections describe the SCO2 pin-fin design.

### 3.6.1 *Introduction*

This section describes the pin-fin design to be manufactured and tested. This design is considered to have the highest manufacturing difficulty and complexity. This is due to the uncertainty of the success of both chemical etching and diffusion bonding.

Figure 3.13 shows a CAD model of the SCO2 pin-fin receiver. The design consists of three plates of increasing thickness. Plate 1 or the “flux plate“ is the plate that absorbs the incident solar flux. This is also where the channels are machined. This plate should be as thin as possible to reduce conduction resistance. However, the plate must be thick enough to avoid structural failure. Plate 2 moves fluid away from plate 1 and into plate 3. It features two or three tall, narrow slots positioned over the inlet(s) and outlet of the channel layer. Each slot is separated into several shorter slots. The extra metal provides necessary structural support. This layer makes little to no contribution to distributing the flow. Plate 3 contains the second part of the header and the global inlet and outlet holes. It features a square cross-section slot adjacent to the slots in plate 2. This slot moves fluid perpendicular to the channel flow direction. These slots extend outside the heated area and connect to the global inlet/outlet holes. Some designs feature two inlet slots on opposite sides of the device and a single outlet slot at the center of the device. Other designs have one inlet and one outlet slot on opposite edges of the

array. In two-inlet designs, extending the header channel outside the heated area allows the two inlets to merge. If one wanted to keep the header channels within the footprint of the heated area, an additional header layer would be needed in order to merge the two inlet headers. Another benefit of extending the header channels outside the heated area is avoiding the issue of transferring pressure during diffusion bonding as described in section 3.1.2.

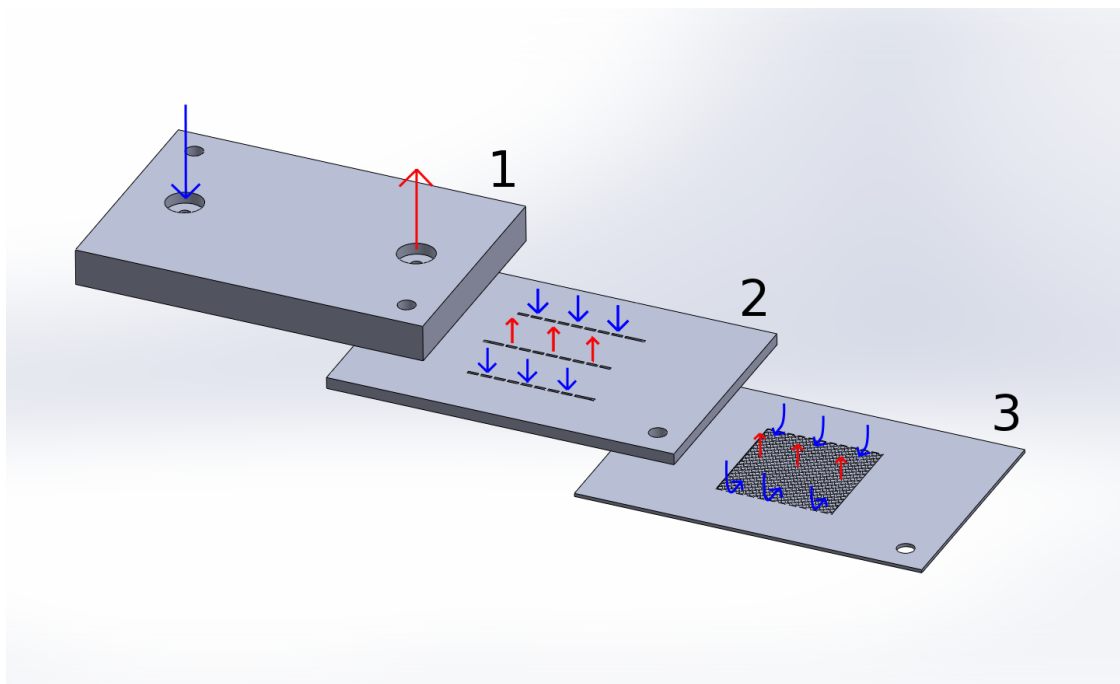


Figure 3.13: SCO<sub>2</sub> Pin-Fin Design: Diagram of pin-fin design. Blue arrows show the path of the cold fluid and red arrows show the path of the hot fluid.

Figure 3.14 shows a photograph of a plate with the pin-fin array which has been manufactured. This plate will be bonded to the other two plates to form the receiver.

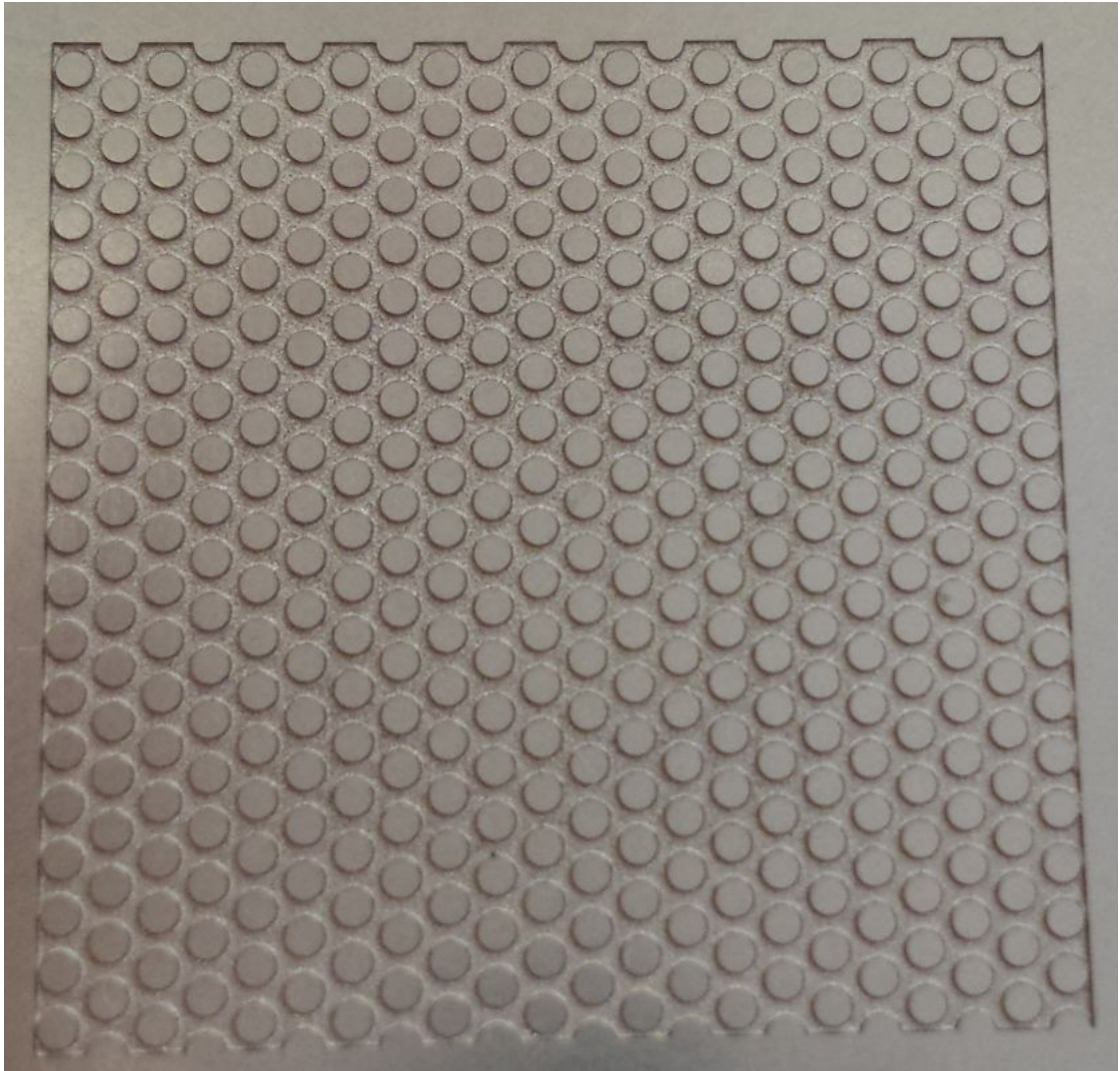


Figure 3.14: SCO<sub>2</sub> Pin-Fin Design: Photograph of a manufactured plate featuring the pin-fin array.

### 3.6.2 *Design Parameters*

Based on analysis described in section 3.2, a circular, staggered, uniformly-spaced configuration is chosen. Based on that and other analyses, the following design parameters are chosen for the final SCO<sub>2</sub> pin-fin design. This is the design

that is to be manufactured and tested using the solar simulator.

The pitch of the pin-fin array is 1.5. This value is based on structural analysis described in section 3.3. The pitch is directly proportional to the ratio of bonded and unbonded area and average mechanical stress in the pins. The pin diameter is 700 micron. This is designed, using single-channel simulations, to meet the pressure drop goal. Note that this is the only design parameter left after manufacturing and structural considerations. The etch depth is 175 micron and the height of the pins is 350 micron. The etch depth is equal to half the edge-to-edge distance between pins as described in section 3.1.1. The dimensions of the heated area are 2 by 2 cm. This is the maximum square area over which the solar simulator can generate an average flux of  $100 \text{ W/cm}^2$ . The length of the fluid path through the pin-fin array was chosen to be 1 cm. This allows the pins to be significantly smaller than if the fluid path was 2 cm long, due to the pressure drop goal. Therefore, the array is divided into two 1 by 2 cm sections. Fluid enters the array through two separate inlets at opposite edges of the device. Fluid flows toward the center of the array and exits through a single outlet.

The design of the headers is described in section 3.5. The solid material is Haynes 230 (see section 3.4).

### 3.6.3 *Analysis*

#### **Setup**

CFD simulation of the complete design is used to evaluate flow distribution and receiver efficiency. The geometry is three-dimensional and includes the fluid and solid domains. A complete 2 by 2 cm pin-fin array is modeled. The device is truncated where the square header in plate 3 extends beyond the heated area.

This is done to reduce computational cost. The pressure drop in this unmodeled section is insignificant compared to pressure drop in the channels. Since exterior faces of the device are treated as insulated, the only unmodeled heat transfer is that between the fluid and the unmodeled header sections. This heat transfer is very small due to the distance from the header surface and low heat transfer coefficient compared to the channels.

The inlet, outlet, and heated area boundary conditions are treated the same as in the single channel simulations. A constant heat flux is applied to the heated area and losses to the environment area not modeled. All other exterior surfaces of the device are insulated. Figure 3.15 shows an illustration of the device and these four boundary conditions. This illustration is the complete device with no symmetry plane, but most simulations also have a symmetry boundary condition where the device is cut in half.

## Results

Table 3.1 shows some of the design parameters for the final pin-fin design and the CFD simulation results. The resulting receiver efficiency is 88.9% (at 95% emissivity). Appendix A.3.1 discusses how this efficiency is calculated for this and all other analyses. Figure 3.16 shows a plot of mass flow rate for each pin-fin gap. A gap is the flow area between two adjacent pins. This flow area is perpendicular to the net flow in the array. The flow distribution is acceptable. However, the flow rate is low near the edge of the array. This is likely due to increased resistance where flow interacts with the wall. The high data point near the right side of the array could be due to inadequately resolved velocity near the exit of the pin-fin array. The flow rate increases slightly from left to right since the right side of the array is closer to the global exit of the model.

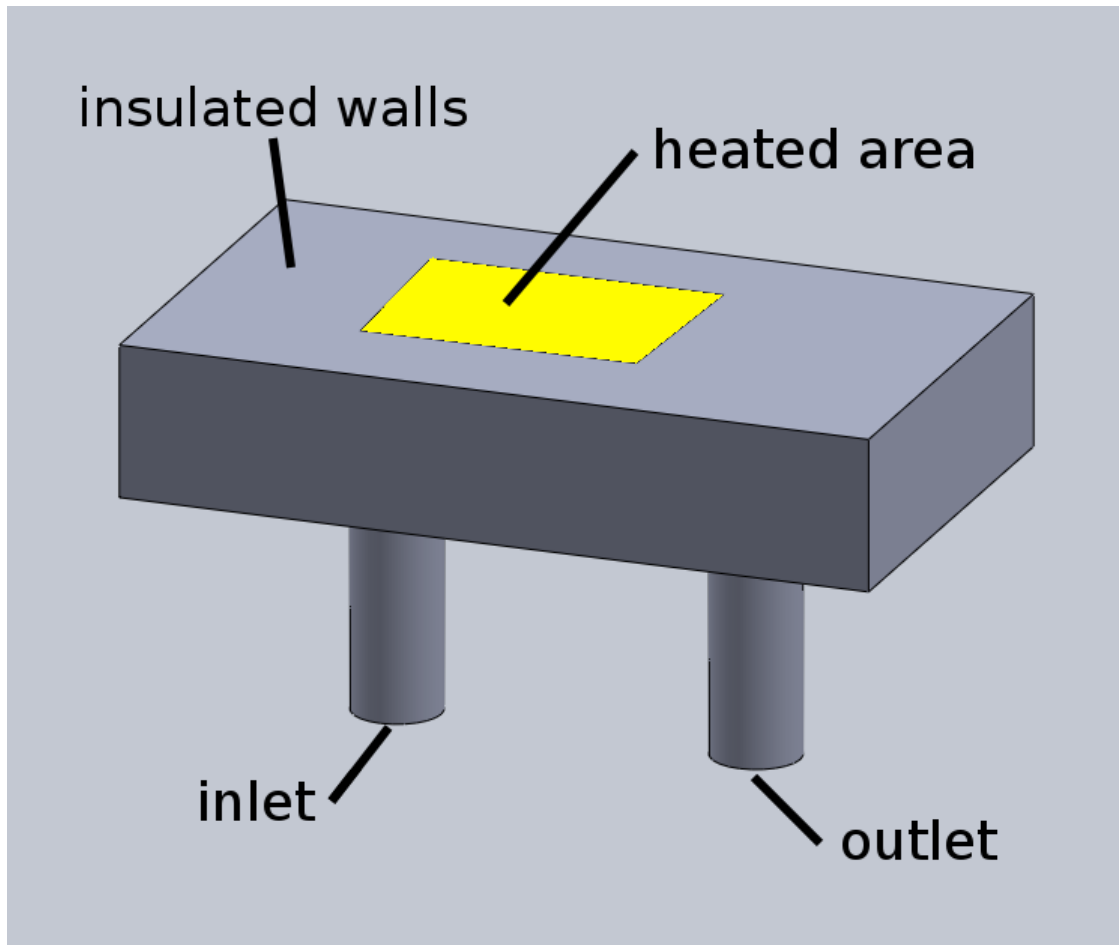


Figure 3.15: Schematic of full-design simulation boundary conditions.

Figure 3.17 shows a contour plot of temperature for a cross-section of the device. The plot is only for the solid region. The circular unfilled areas are the fluid region between the pins. The bottom edge of the plot is the heated surface; the yellow arrows represent the solar flux. There is a slight increase in temperature from left to right. This is because the global outlet of the device is on the right.

pin diameter	700 micron
transverse pitch	1.5
Reynolds number	$1.12 \times 10^4$
pressure drop	0.1 bar
heated surface temperature	1021 Kelvin
receiver efficiency (at 95% emissivity)	88.9%

Table 3.1: Parameters and results of full-design CFD simulation of the SCO2 pin-fin design.

### 3.6.4 *Manufacturing Issues*

After completing this design, manufacturing began. As was feared, Haynes 230 cannot be chemically etched. The following sections discuss two alternative designs that do not depend on chemical etching.

Eventually, it was learned that sinker EDM (electric discharge machining) could be used to manufacture the pin-fin design. In sinker EDM, a high voltage is created between a very thin wire electrode and the metal sheet to be machined. When the electrode is brought close to the sheet, an electric arc forms and a small amount of metal in the sheet is vaporized. This is done repeatedly until the sheet is machined. Devices have since been manufactured but have not yet been tested.

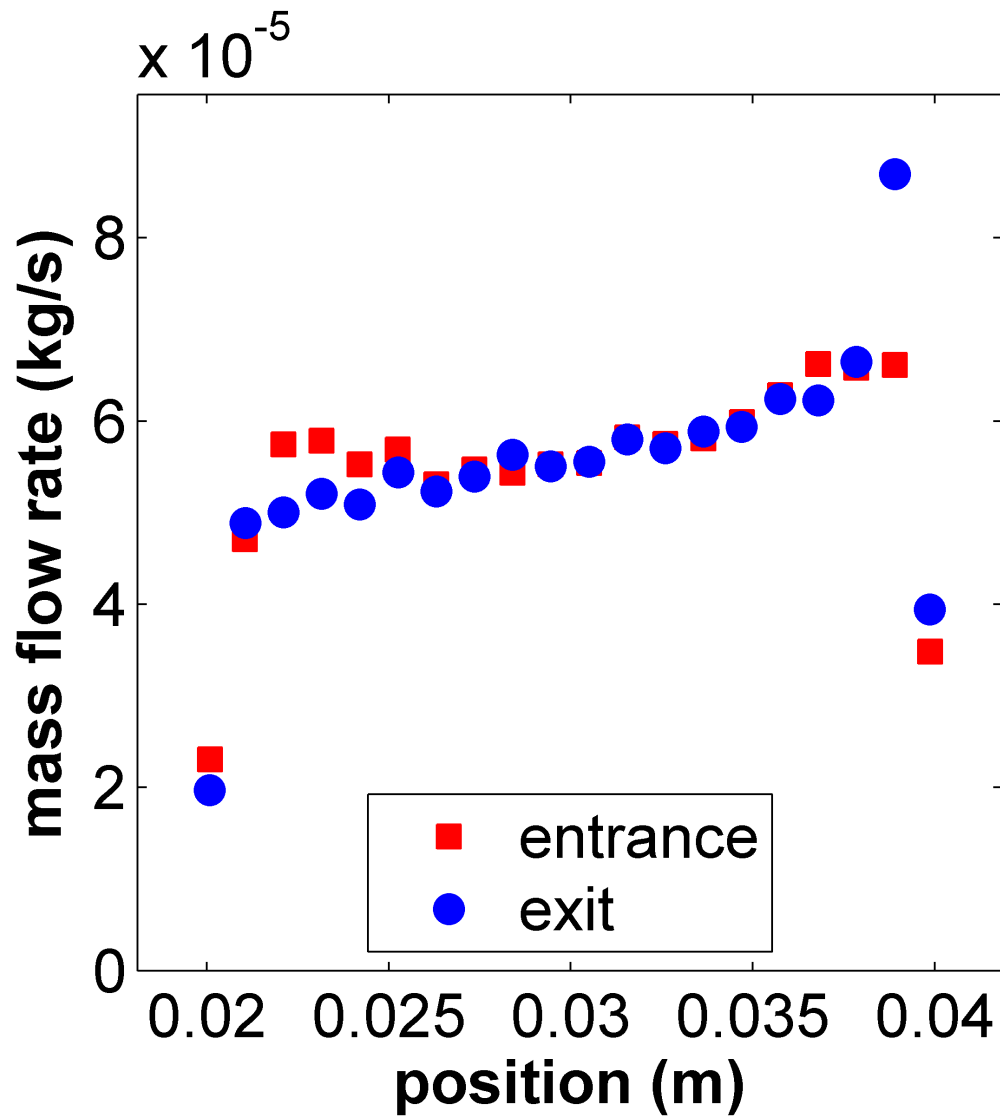


Figure 3.16: SCO2 Pin-Fin Design: Plot of mass flow rate for each pin gap at the inlet and outlet of the pin-fin array.

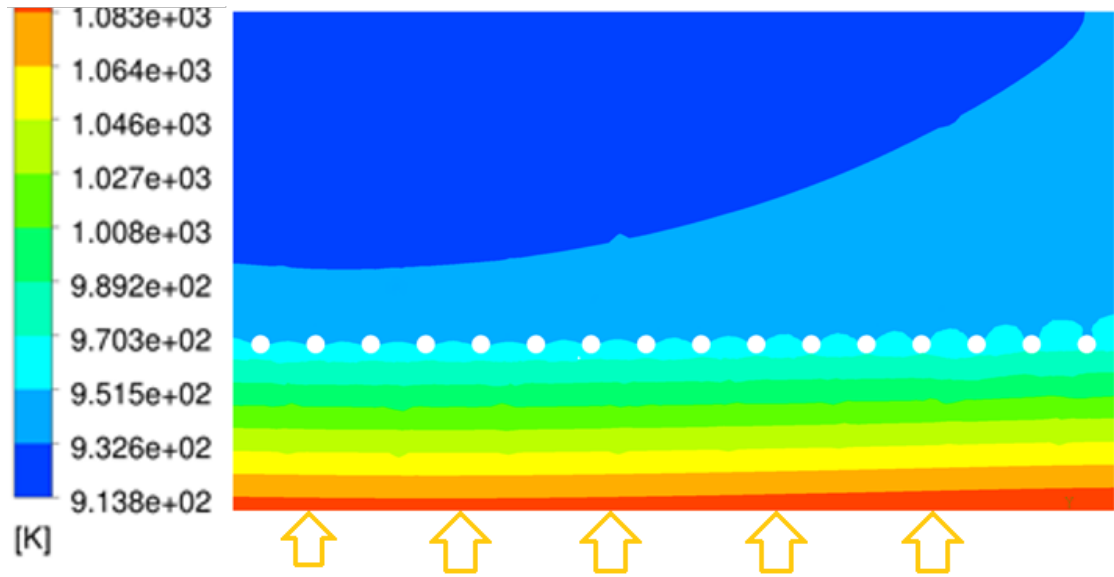


Figure 3.17: SCO2 Pin-Fin Design: Contour plot of temperature of the solid material at a cross-section of the device midway along the length of the pin-fin array.

## 3.7 Circular Channels

The following sections describe the SCO2 circular channel design.

### 3.7.1 *Introduction*

The first alternative design has drilled circular channels and parts that are welded together. The device involves no chemical etching or diffusion bonding. It, therefore, has the lowest manufacturing difficulty and complexity of any design.

The design consists of three parts: two header parts and one channel part. The channel part slides into the machined cavity in each of the header parts and is welded. Tubes are welded to large holes in the header parts to serve as the global inlet and outlet. Figure 3.22 shows an exploded view of the design. Note that this design is not scalable and therefore cannot meet all of the goals of the project. Figure 3.19 shows a top wire-frame view of the device. This figure more clearly illustrates how the fluid moves through the device and gives a better view of the channels.

Figure 3.20 is a photograph of the manufactured and assembled receiver before being welded.

### 3.7.2 *Design Parameters*

Many of the parameters for the circular channel design are limited by manufacturing capabilities. The channel diameter is 500 micron. This is the smallest available drill size. The length of the microchannels is 1.8 cm (only 1 cm of which

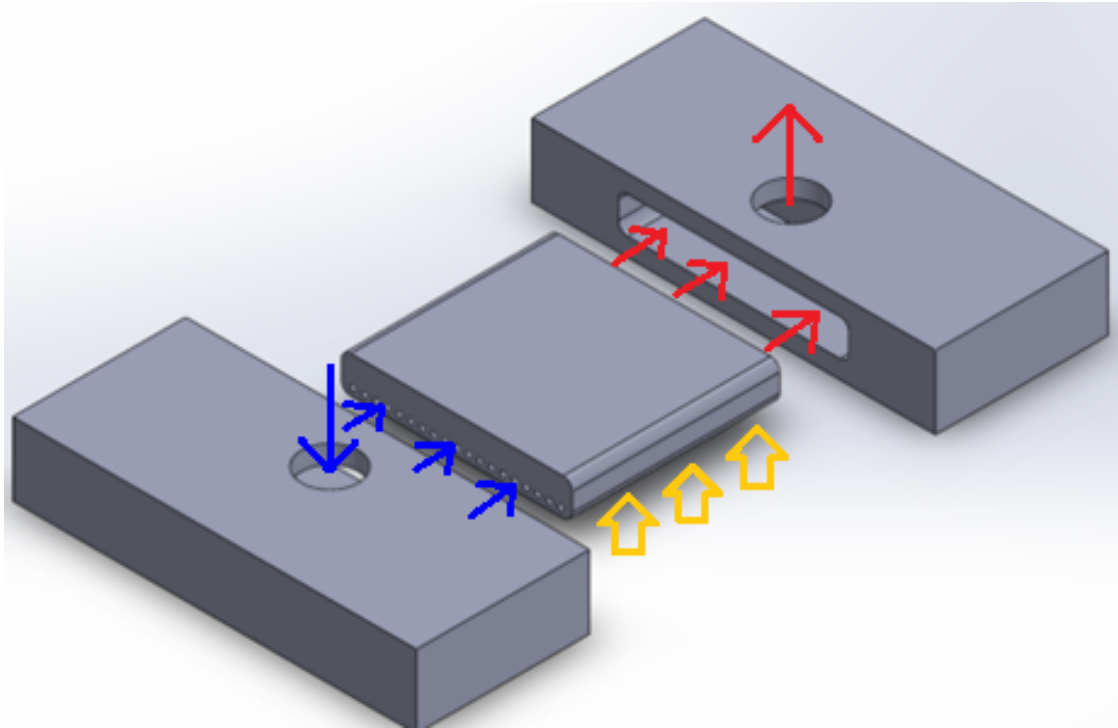


Figure 3.18: SCO<sub>2</sub> Circular Channel Design: Exploded view of the design. Blue arrows show the path of the cold fluid and red arrows show the path of the hot fluid. Yellow arrows show the direction of the solar flux.

is heated). This is maximum possible drill depth at the chosen diameter. The width of the microchannel array is 2 cm. As stated earlier, this is based on the capability of the solar simulator. The flux plate thickness is 450 micron. This is based on structural analysis of the microchannels. The width of the wall separating adjacent channels is 500 micron. This value is also based on structural analysis of the microchannels.

The header length is 6 mm (direction parallel to channel flow). This value was determined by trial and error using CFD simulations. It is designed to give adequate flow distribution in the channels. The solid material is Haynes 230.

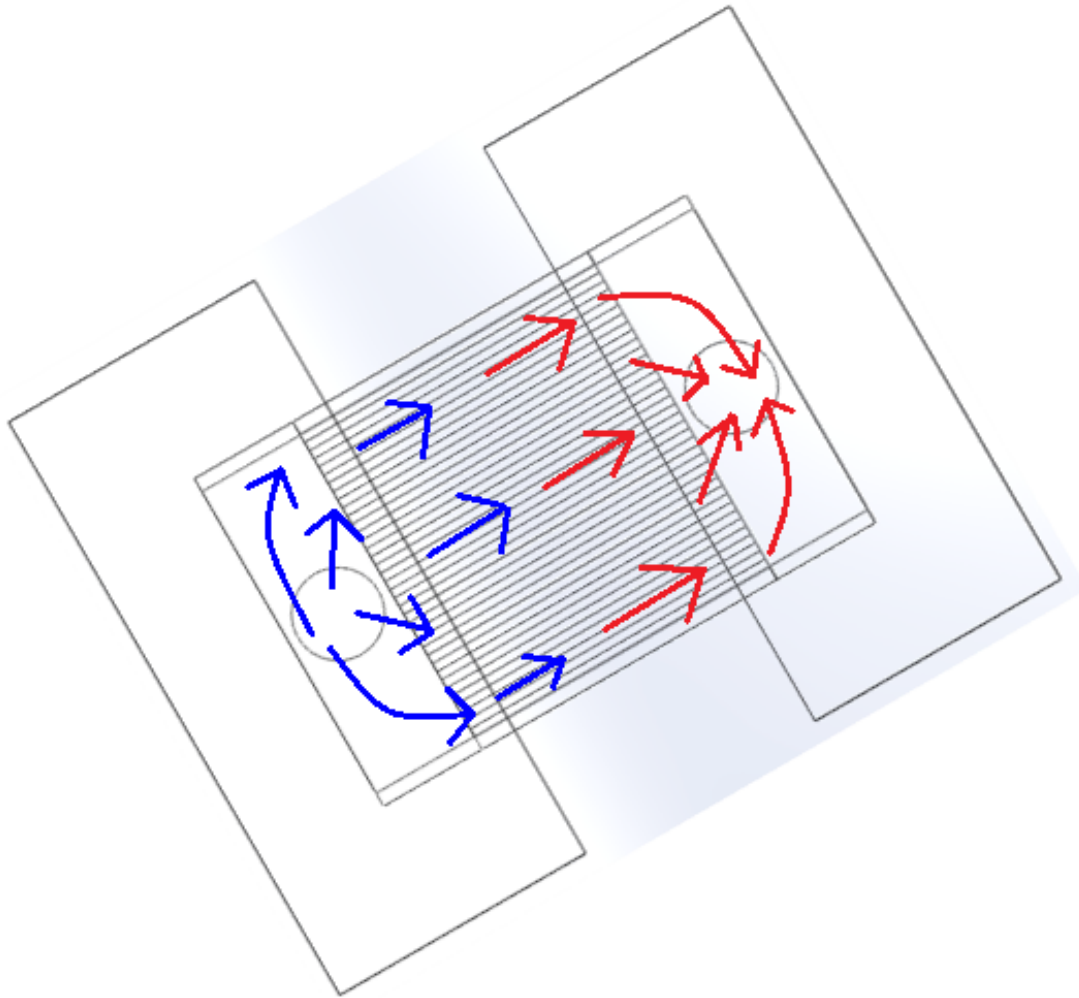


Figure 3.19: SCO<sub>2</sub> Circular Channel Design: Top wire-frame view. Blue arrows show the path of the cold fluid and red arrows show the path of the hot fluid.

### 3.7.3 Analysis

#### Full-design, Conjugate, CFD Simulations

Full-design, conjugate, CFD simulations are used to assess pressure drop, receiver efficiency, and flow distribution. Both the solid and fluid domains are modeled. The simulation geometry includes the entire device except for the inlet



Figure 3.20: SCO2 Circular Channel Design: Photograph of assembled device prior to welding of the three parts and inlet and outlet tubes.

and outlet tubes. Symmetry is used to cut the model in half. Though the geometry is different, the boundary conditions are identical to those used in the SCO2 pin-fin full-design simulations.

Table 3.2 shows the design parameters and CFD simulation results. The dimensions of the channels are restricted by manufacturing capabilities and otherwise would have been designed with higher pressure drop and efficiency. Flow is adequately distributed as seen in figure 3.21.

channel diameter	500 micron
wall width	500 micron
Reynolds number	$3.91 \times 10^3$
pressure drop	0.07 bar
heated surface temperature	1082 Kelvin
receiver efficiency	87.5%

Table 3.2: Parameters and results of full-design CFD simulation of the SCO2 circular channel design.

### FEA

Three-dimensional FEA was performed on one of the header parts. The geometry included one header part, a truncated channel part, and an idealized weld bead. The weld bead provides necessary structural support and eliminates stress concentrations at some of the sharp corners on the exterior of the device. Only mechanical stress is considered since thermal gradients are small in the header.

Two-dimensional FEA is performed for a cross-section of the channel part. The temperature results from the CFD simulation are applied in order to model the thermal stress. The minimum structural safety factor from both of these analyses is 1.3. The highest stress occurs in one of the channel walls, primarily due to thermal stress. Thermal stress is higher in the circular channel design than other designs because of the relatively large channels. Larger channels have less total surface area and higher average flux at the channel walls.

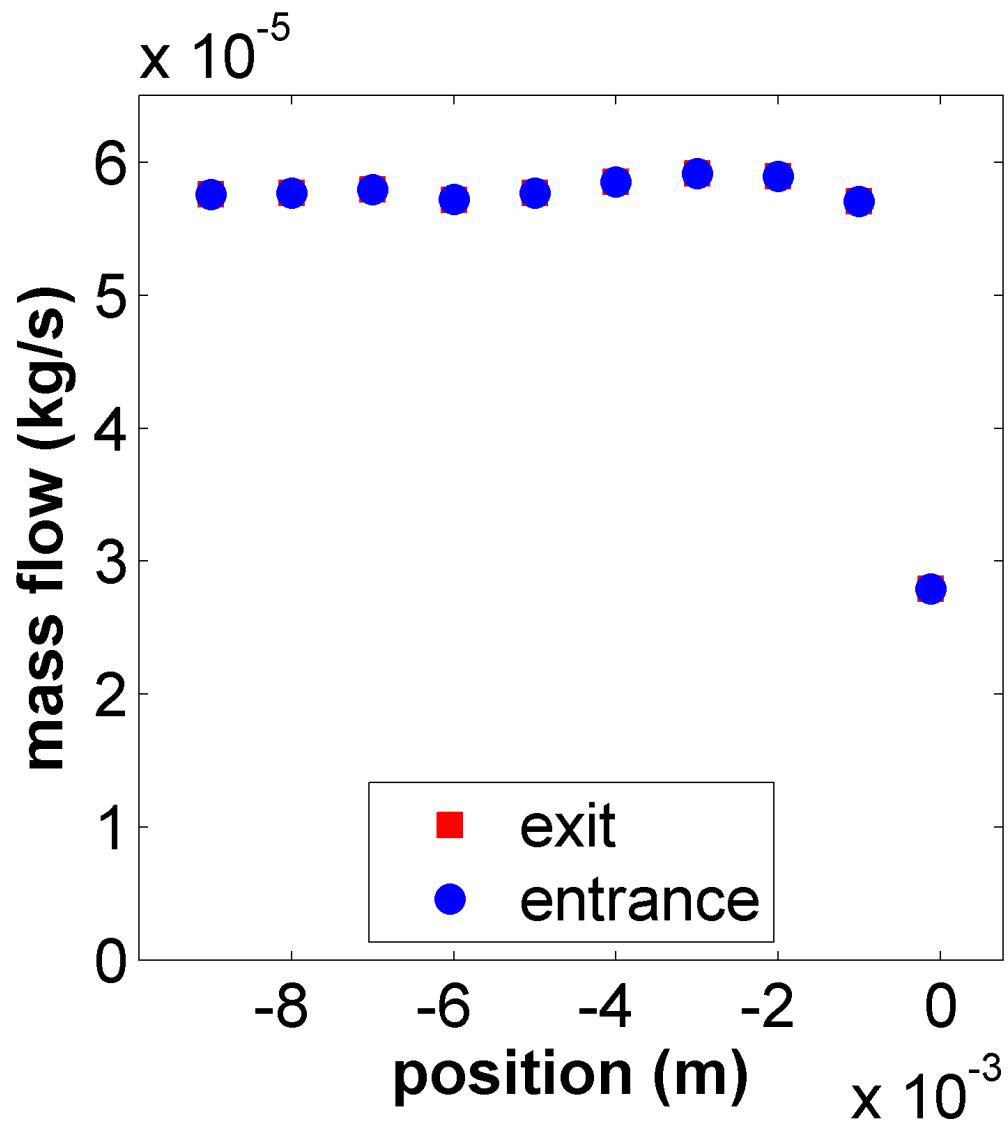


Figure 3.21: SCO2 Circular Channel Design: Plot of mass flow rate for each individual channel.

## 3.8 Rectangular Channels

The following sections describe the SCO2 rectangular channel design.

### 3.8.1 *Introduction*

The second alternate design is similar to the pin-fin design. Instead of a pin-fin array, it features parallel rectangular channels which are machined instead of chemically etched. This design is higher risk than the circular channel design because it features diffusion bonding, the strength of which is uncertain for Haynes 230.

Figure 3.22 shows a CAD model of the SCO2 rectangular channel receiver. The blue and red arrows represent the path of the cold and hot fluid. The solar flux is incident on the underside of the bottom-most plate. The large holes on the top-most plate are the global inlet and outlet of the device. Fluid is distributed in header channels on the underside of this plate before flowing down through the middle plate and into the microchannels.

Some designs have channels machined in two halves in the bottom and middle plates. This moves the diffusion bond seam to the middle of the channel, away from the corners where high stress occurs. Other designs have channels machined entirely in the bottom plate.

Figure 3.23 shows a top wire-frame view of the receiver. This plot better illustrates flow through the receiver. The three horizontal channels are the header channels; two inlet and one outlet.

Figure 3.24 is a photograph of a plate with the machined microchannels.

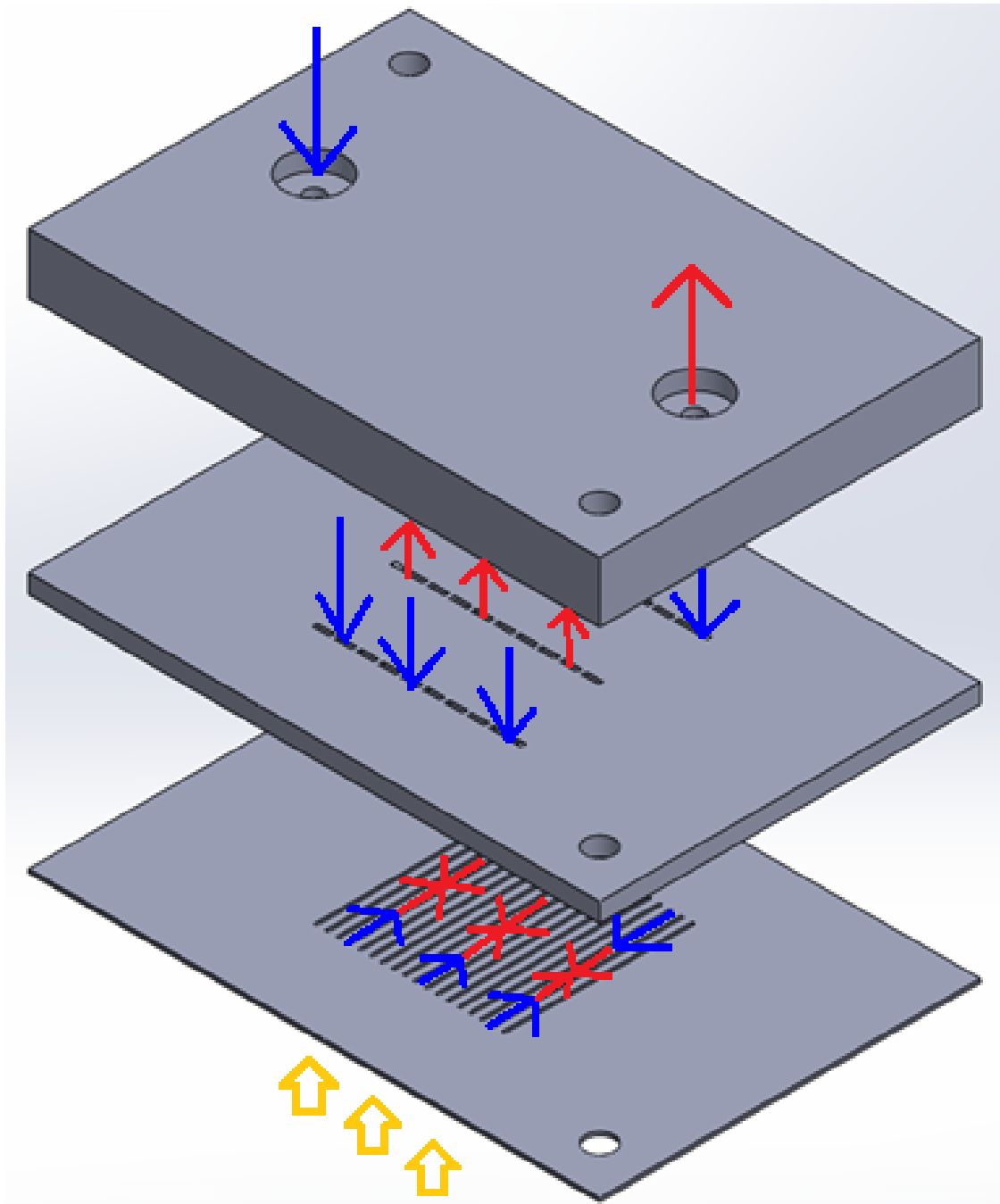


Figure 3.22: SCO<sub>2</sub> Rectangular Channel Design: Exploded diagram of the three plates. Blue arrows show the path of the cold fluid and red arrows show the path of the hot fluid. Yellow arrows show the direction of the solar flux.

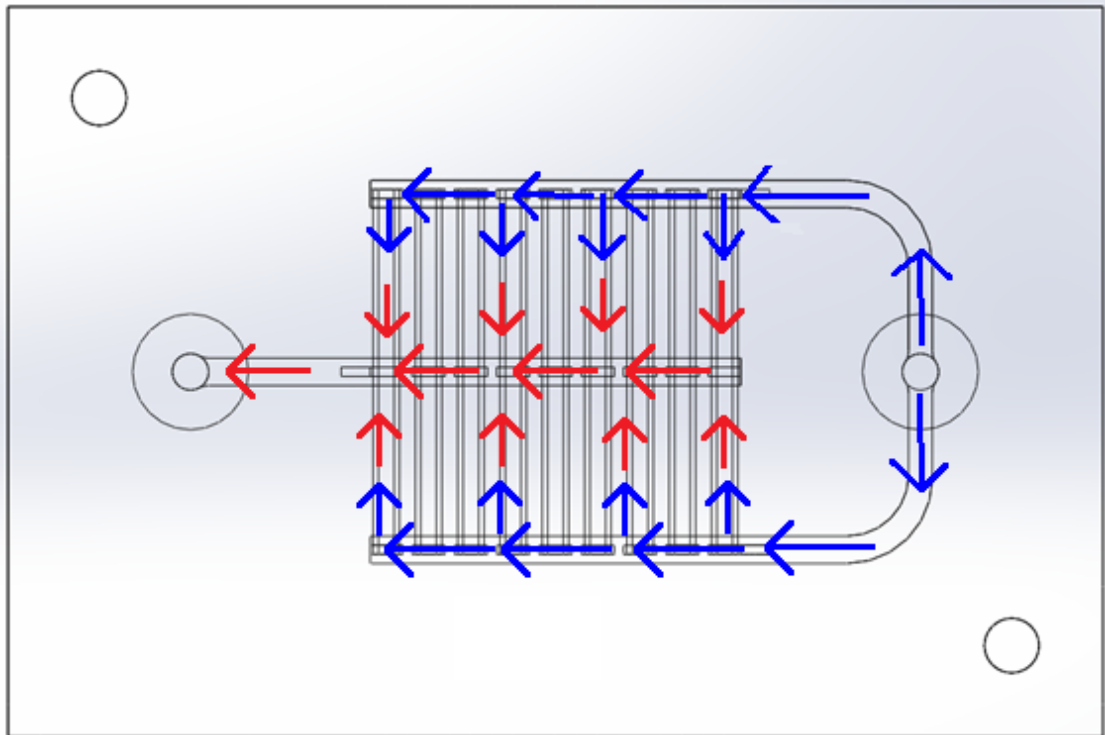


Figure 3.23: CO<sub>2</sub> Rectangular Channel Design: Top wireframe view. Blue arrows show the path of the cold fluid and red arrows show the path of the hot fluid.

This plate will be bonded to the other two plates to form the receiver.

### 3.8.2 *Design Parameters*

Some of the design parameters cover a range of values or have multiple configurations. These variants will be manufactured in order to test the effects of various parameters.

The solid material is Haynes 230. Channel height ranges from 110 to 260 micron. Channel width ranges from 300 to 500 micron. For each design variant, the flow area is designed to meet the pressure drop goal. The number of channels

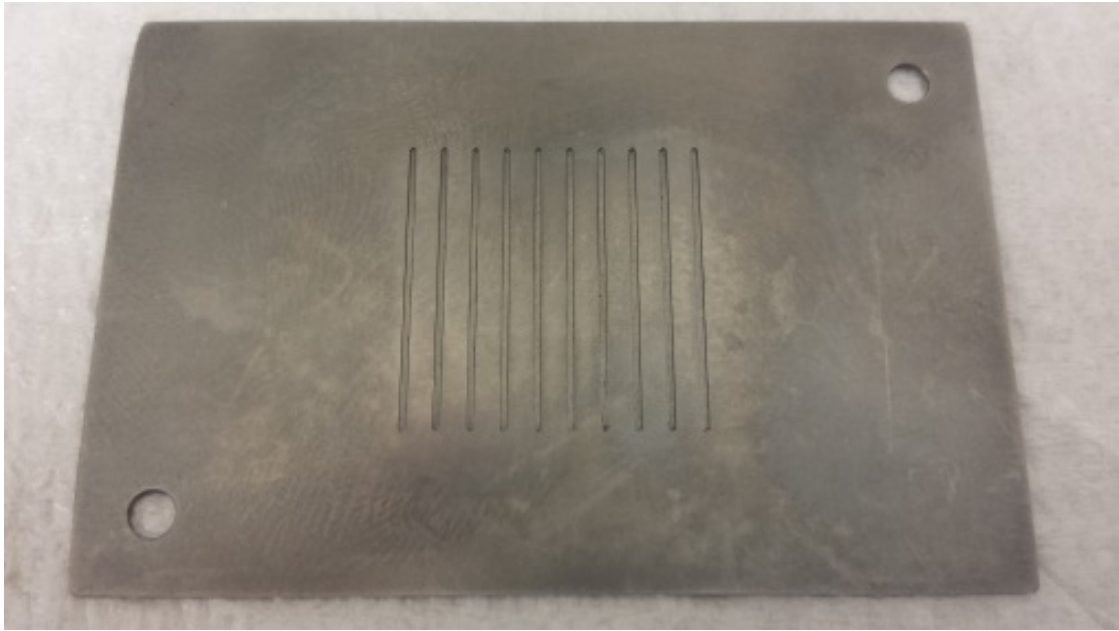


Figure 3.24: SCO<sub>2</sub> Rectangular Channel Design: Photograph of a manufactured microchannel plate.

ranges from 9 to 32. The number of channels changes with channel width and is used in conjunction with channel height to control the pressure drop.

The dimensions of the microchannel array are 2 by 2 cm. As described earlier, this is determined by the capacity of the solar simulator. The length of the channels is either 1 or 2 cm. If the length is 1 cm, fluid enters the microchannels at opposite edges of the array and converges at the center (two inlet and one outlet). If the length is 2 cm, fluid enters at one edge and exits at the opposite edge. The thickness of the flux plate ranges from 300 to 500 micron. This is determined by structural analysis.

channel width	300 micron
channel height	180 micron
wall width	931 micron
Reynolds number	$7.15 \times 10^3$
pressure drop	0.02 bar
heated surface temperature	980.3 Kelvin
receiver efficiency	89.7%

Table 3.3: Parameters and results of full-design CFD simulation of the SCO<sub>2</sub> rectangular channel design.

### 3.8.3 Analysis

#### Full-Design, Conjugate CFD Simulation

Three-dimensional CFD simulations are used to evaluate receiver efficiency and flow distribution for one of the design variants. The setup for this simulation is nearly identical to the CFD simulation for the pin-fin design. The geometry includes the fluid and solid domain up to where the square header in plate 3 extends beyond the heated area. The length of the channels is 1 cm, resulting in two 1 by 2 cm arrays placed side-by-side. Table 3.3 shows the design parameters and CFD simulation results. Figure 3.25 shows a contour plot of temperature of the solid region for a cross-section of the device. The flow distribution is adequate as seen in figure 3.26.

#### FEA

Two-dimensional FEA is performed for a cross-section of the microchannel array. Both thermal and mechanical stresses are considered. The resulting stress is much lower than that in the header channels as described in section 3.5.

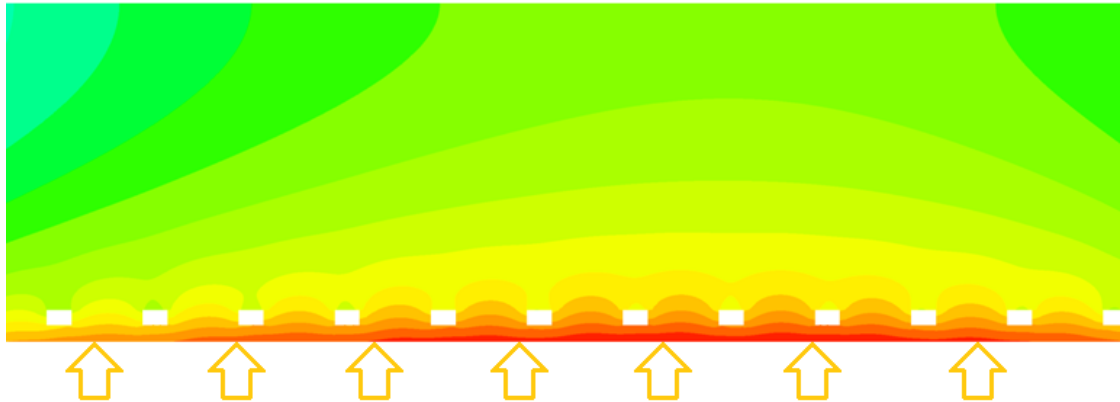


Figure 3.25: SCO<sub>2</sub> Rectangular Channel Design: Contour plot of temperature of the solid at a cross-section midway along the channels. Flow is into the page and solar flux is indicated by the yellow arrows.

### 3.9 Conclusion

Based on CFD simulations, receiver efficiencies are 88.9% for the pin-fin design, 87.6% for the circular channel design, and 89.7% for the rectangular channel design. These are very close to the goal of 90%. The other goals and requirements, such as flow distribution and structural integrity, are also met. Table 3.4 summarizes the three SCO<sub>2</sub> designs with some key characteristics.

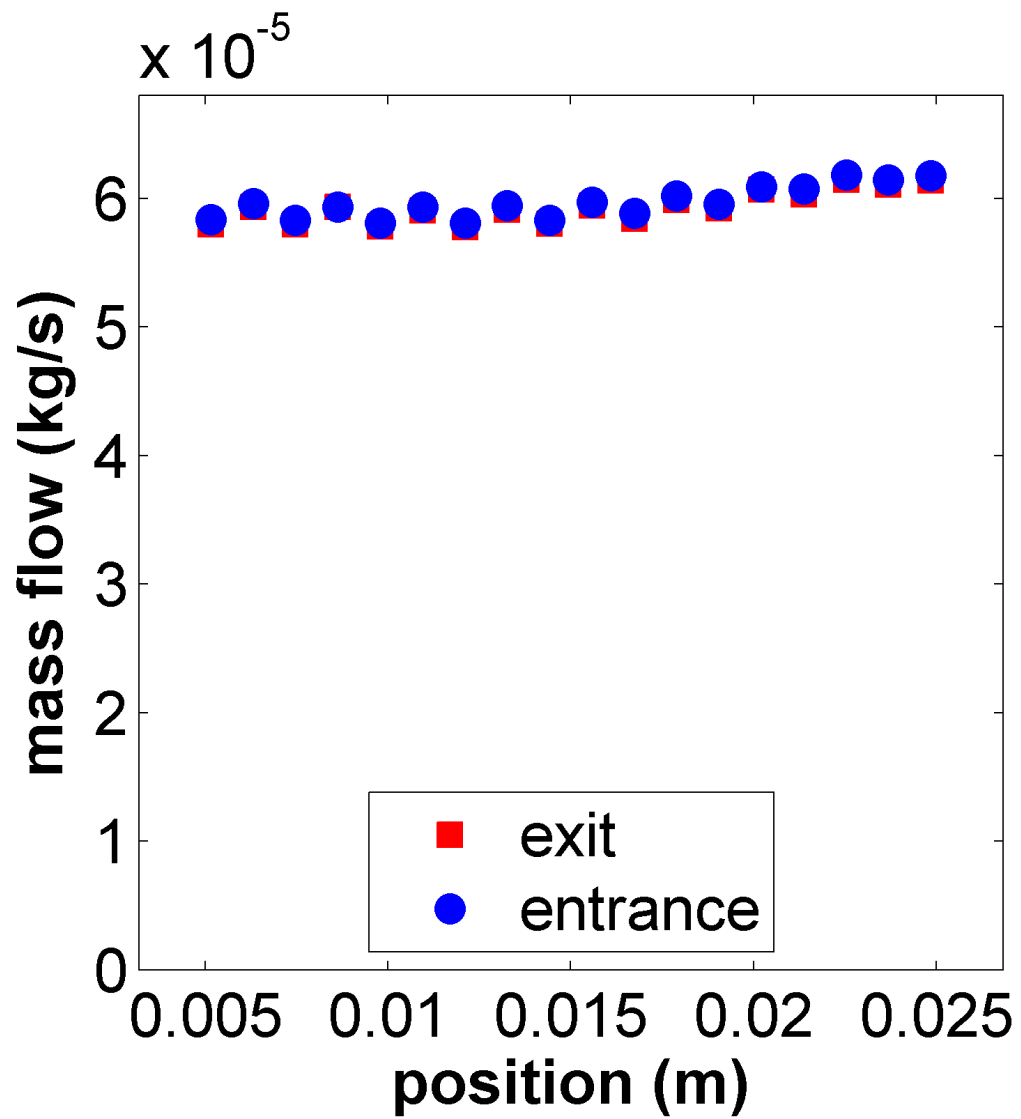


Figure 3.26: SCO<sub>2</sub> Rectangular Channel Design: Plot of mass flow rate for each individual channel.

Design	Manu. Methods	Manu. Complexity	Stress	Flow Dist.	Pressure Drop	Scalable
Design pin-fin	chemical etching (or sinker EDM) and diffusion bonding	high (medium for sinker EDM)	stress in pins is low if well aligned; highest stress is in header	good	larger pressure drop due to limits of isotropic etching on channel depth (not an issue with sinker EDM)	yes
circular channels	drill and welding	low	stress in channels is low; header design needs careful thought to minimize stress	good	low (relatively large channels)	no
rectangular channels	milling and diffusion bonding	medium	stress in channels is low; highest stress is in header	good	could be low if low aspect ratio (deeper) channels used	yes

Table 3.4: Comparison of SCO2 Designs

## CHAPTER 4. MOLTEN SALT DESIGNS

---

### 4.1 Rectangular Channels

#### 4.1.1 *Introduction*

The first molten salt design is a rectangular channel design similar to the SCO<sub>2</sub> rectangular channel design. The design features rectangular channels machined in a thin plate and additional plates for header channels. The plates are then diffusion bonded. There are three plates in the design. Plate 1, or the “flux plate”, is where the channels are machined and the solar flux is incident. Plates 2 and 3 are essentially identical to plates 2 and 3 in the SCO<sub>2</sub> rectangular channel and pin-fin designs. Figure 4.1 shows an exploded view of the design. Figure 4.2 shows a top wire-frame view of the design. This figure clearly shows the path of the fluid through the device: from the cold inlet on the left, to the hot outlet on the right.

#### 4.1.2 *Design Parameters*

The lower average fluid temperature and operating pressure than SCO<sub>2</sub> makes it possible to use SS for the solid material. Using SS lowers cost and fabrication time of the device and allows for the use chemical etching. However, for the first MS devices manufactured, Haynes 230 is still used and the channels

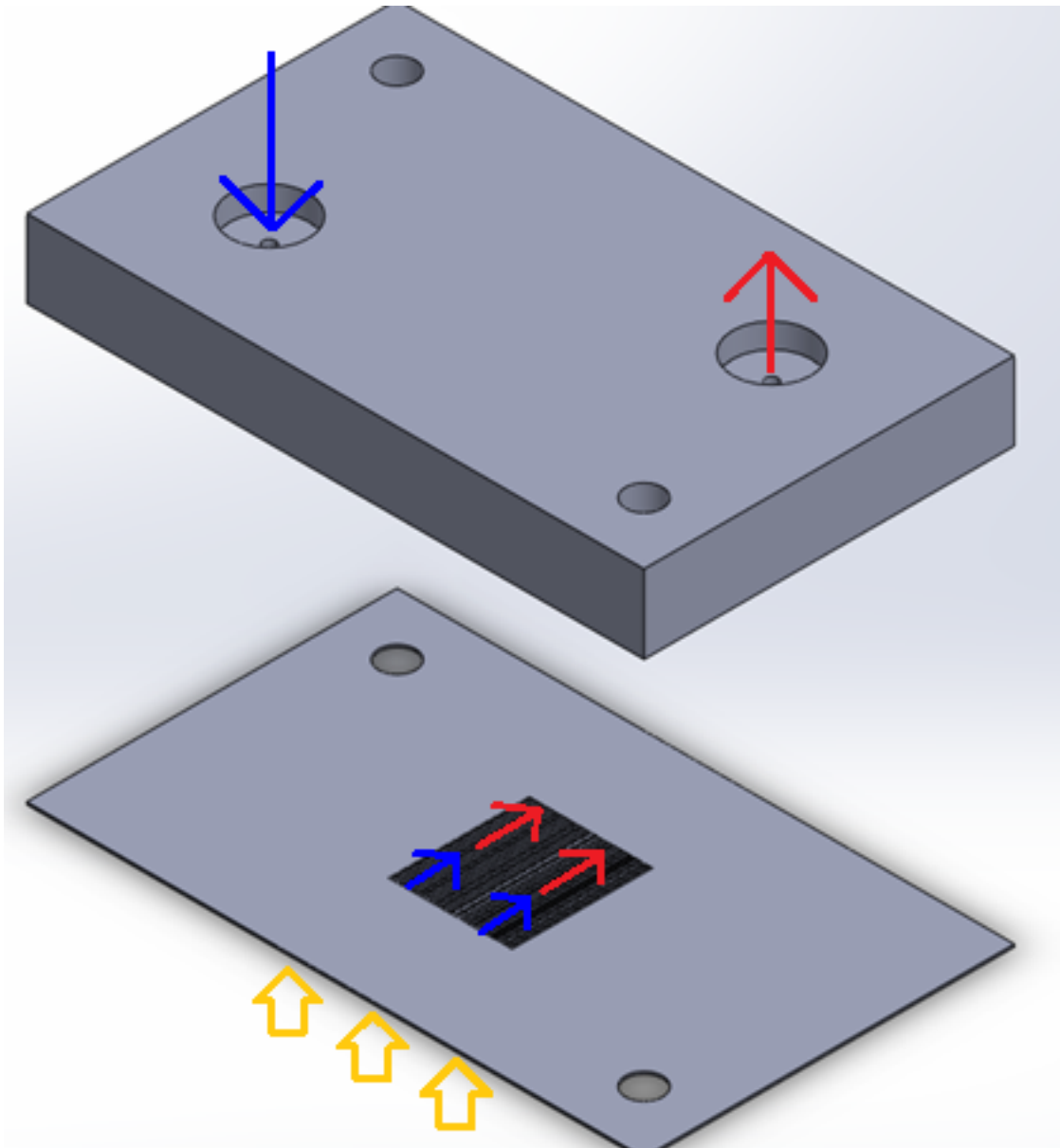


Figure 4.1: MS Rectangular Channel Design: Exploded view showing the design without the middle header plate. Blue arrows show the path of the cold fluid and red arrows show the path of the hot fluid. Yellow arrows show the direction of the solar flux.

are machined as stated early. The heated area is 1 by 1 cm. This is the maximum square area over which the solar simulator can provide an average incident flux of

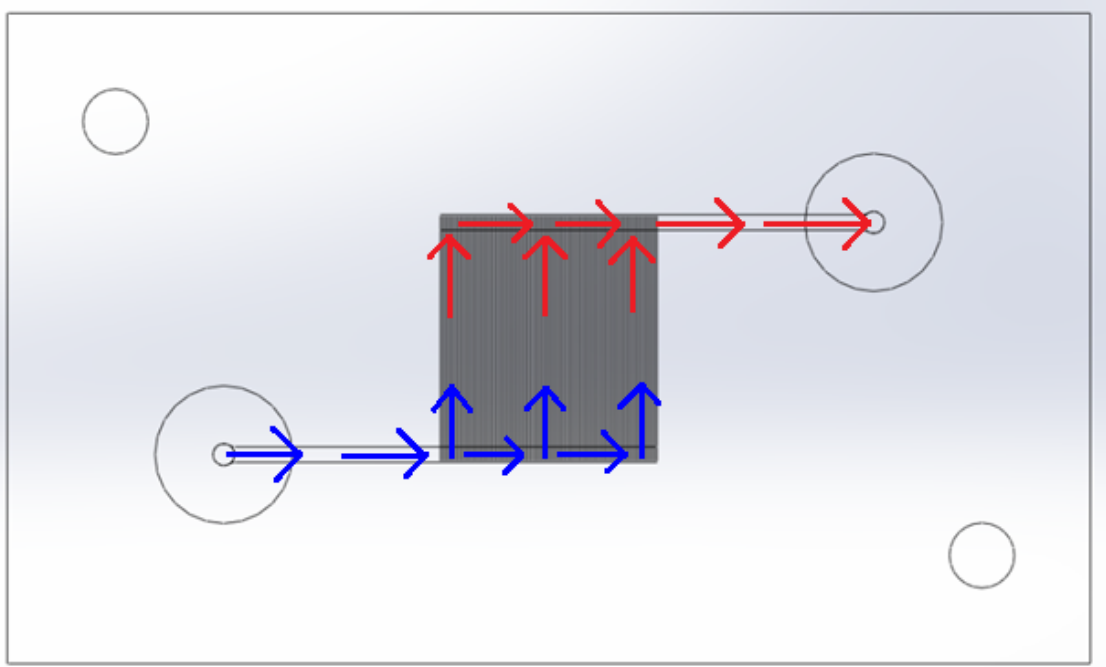


Figure 4.2: MS Rectangular Channel Design: Top wire-frame view. Blue arrows show the path of the cold fluid and red arrows show the path of the hot fluid.

400 W/cm<sup>2</sup>. The channel length is 1 cm. The length is limited by the solar simulator as described above. The channels could be longer and still meet the pressure drop goal and will be made longer in scaled-up design. The channel cross-sectional dimensions are 100 by 100 micron. These dimensions are limited by manufacturing capabilities. The channels can be smaller and still meet the pressure drop goal, given the channel length of 1 cm. The flux plate is 100 micron thick. This is based on structural analysis performed to ensure structural integrity near the flux plate.

When designing the SCO<sub>2</sub> header for the pin-fin and rectangular channel designs, the high operating pressure was an obstacle. The middle plate was necessary in order to separate the large header channel from the thin flux plate. If the same design is used with MS, even with SS as solid material, structural integrity in the

headers will not be as severe of an issue due to the reduced operating pressure. It may even be possible to eliminate the middle plate and still have adequate structural integrity. Additional structural analysis is needed to determine if the flux plate will fail if the large header channel is adjacent to it. Figure 4.1 shows an exploded view of the design with the middle plate removed.

### 4.1.3 Analysis

#### **FEA**

In the absence of high operating pressure, thermal stresses are higher than mechanical stresses. As a result, three-dimensional FEA of mechanical stress in header (as was performed for SCO<sub>2</sub>) is not necessary. Instead, only two-dimensional FEA of a cross-section of the microchannels is performed. The primary concern is thermal stress in the channel walls due to the high incident flux in the MS designs. The resulting safety factor was 2.5.

#### **CFD**

Similar to the SCO<sub>2</sub> rectangular channel and pin-fin designs, a three-dimensional CFD simulation of the complete design is performed. The geometry includes the fluid and solid domain up to where the header channels extend beyond the heated area. The primary purpose of this simulation is to estimate efficiency and flow distribution.

Table 4.1 shows the parameters and CFD simulation results. Figure 4.3 shows a contour plot of temperature of the solid at a cross section of the microchannels. Figure 4.4 shows a plot of mass flow rate. The flow rate increases toward the global outlet of the device but is not severely maldistributed.

channel width	100 micron
channel height	100 micron
wall width	100 micron
Reynolds number	93
pressure drop	0.5 bar
heated surface temperature	800 K
receiver efficiency (95% emissivity)	94.3%

Table 4.1: Parameters and results of full-design CFD simulation of the MS rectangular channel design.

In the mass flow rate plot, there is a small difference between the total mass flow rate between the inlet and outlet. This error is due to the post-processing used to calculate the mass flow rate. In this particular simulation, mass flow rate could not be directly extracted from the CFD software. Instead, velocities at individual cells were extracted. The cross-sectional area of the channel associated with each of these cells also could not be extracted. Therefore, that area had to be estimated, a difficult task due to nonuniform distribution of cells (due to refinement near the walls). The error in the assumed area resulted in the error in the mass flow rate. However, the comparison between the flow rate in individual channels at the either the inlet or exit is still accurate, and an assessment of flow distribution can still be made. This issue is avoided in other CFD simulations by creating the initial geometry in such a way that the mass flow rate can be directly extracted.

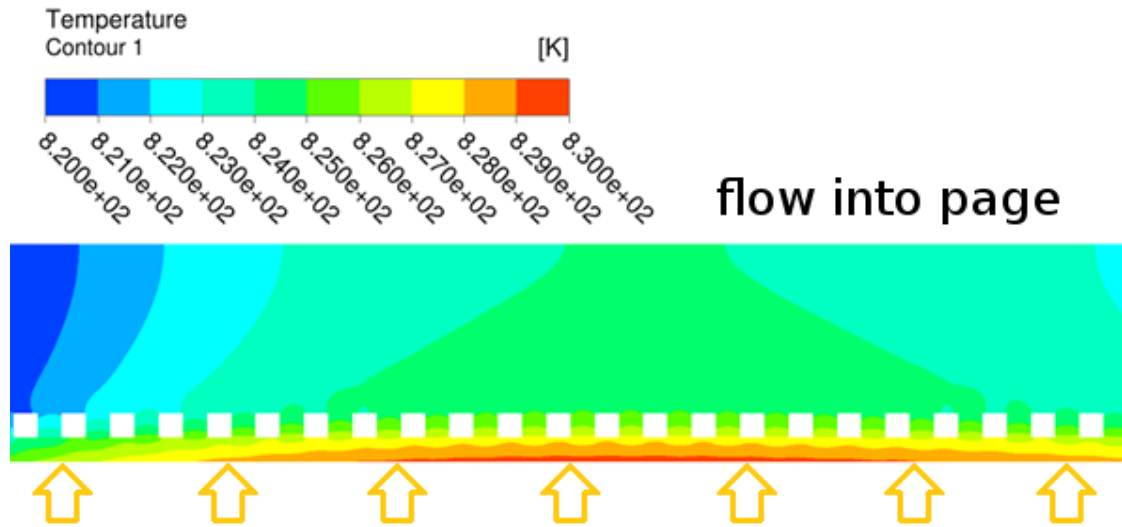


Figure 4.3: MS Rectangular Channel Design: Contour plot of temperature of the solid at a cross-section midway along the channels. Flow is into the page and solar flux is indicated by the yellow arrows.

## 4.2 Pin-Fin Array

### 4.2.1 Introduction

Development recently began on a pin-fin design for MS which will be similar to the SCO<sub>2</sub> pin-fin design. The design features a chemically etched pin-fin array. Chemical etching is possible due to the use of SS as the solid material (see previous section).

### 4.2.2 Single Channel Simulations

Single channel simulations, similar to those discussed in 3.2, are used to characterize pressure drop. These simulations consists of the fluid region for a one-

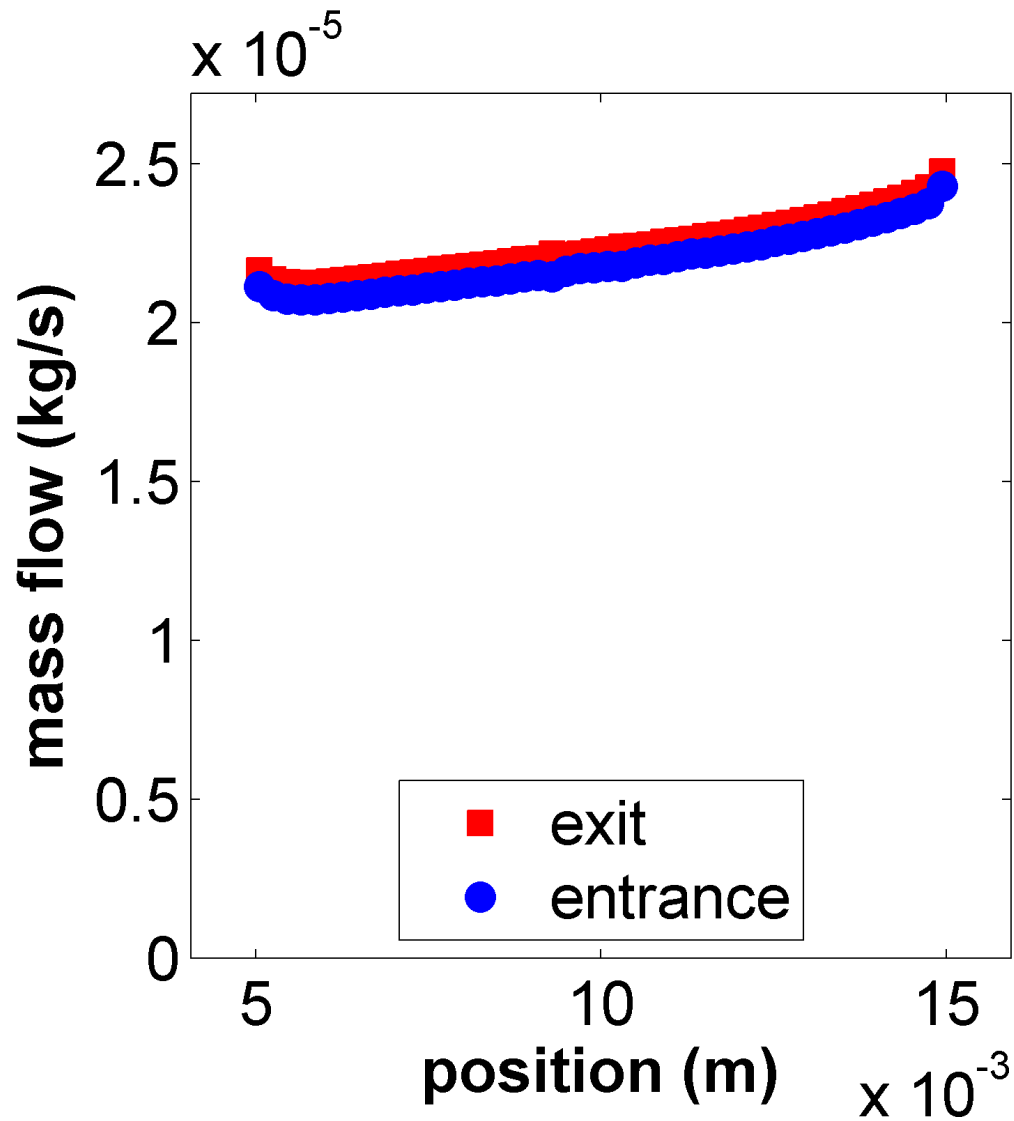


Figure 4.4: MS Rectangular Channel Design: Plot of mass flow rate for each individual channel (difference between inlet and outlet due to error in post-processing, description in text).

transverse-spacing-wide section of the pin-fin array. Figure 4.5 shows an example of the simulation geometry used.

The independent variables are pin diameter and pitch and the dependent variable is friction factor. Pressure drop is extracted directly from the simulations

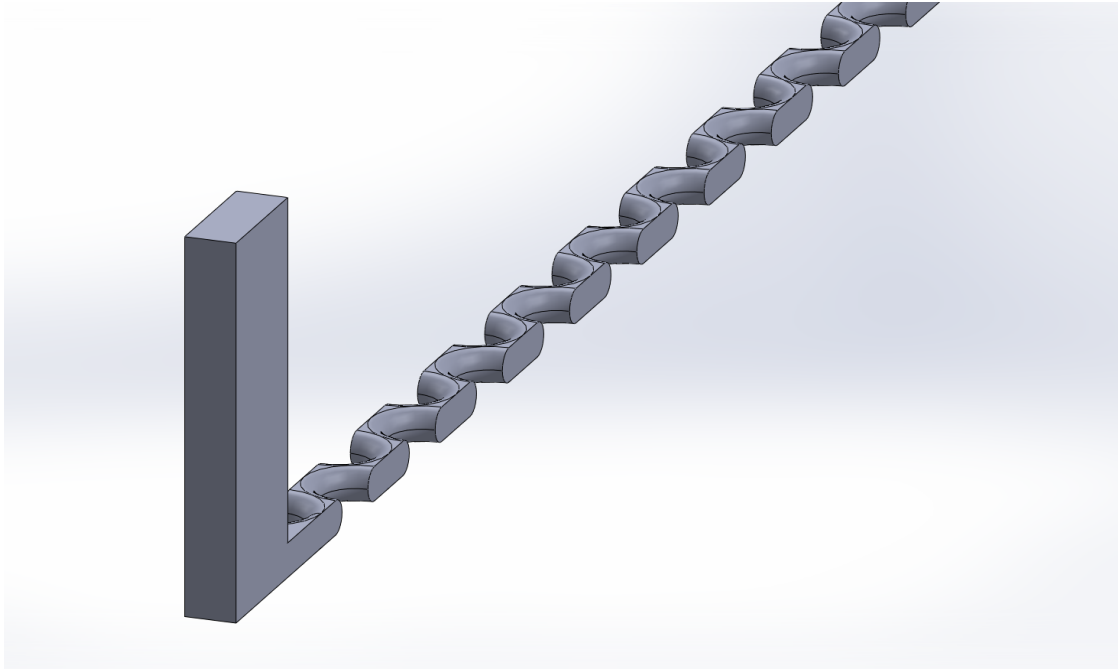


Figure 4.5: MS Pin-Fin Design: Diagram showing one end of the single channel geometry. This is the fluid volume.

and used to calculate friction factor. Table 4.2.2 shows the values of each variable. There are four data points, one for each combination of the two values of pin diameter and pitch. Based on these data, the friction factor is fit to a curve of the form

$$f = AD^B P^C \quad (4.1)$$

where  $f$  is friction factor,  $D$  is diameter,  $P$  is pitch, and  $A$ ,  $B$ , and  $C$  are coefficients determined by a least squares regression. With this equation for friction factor, one can estimate the values of pitch and diameter that will give a desired pressure drop over a given length.

diameter (micron)	pitch	friction factor
188	1.5	17.8
188	2.0	46.5
250	1.5	9.3
250	2.0	27.7

Table 4.2: Results of MS pin-fin single channel simulations

### 4.2.3 Header Simulations

Unlike with the previous designs, the project sponsors decided that, for the MS pin-fin design, the designed pressure drop in the channels should be based on achieving adequate flow distribution. In other words, the pressure drop in the channels should be at least ten times that in the headers. This method gives a minimum pressure drop in the channels. A maximum pressure drop goal should still be met in order to avoid excessively high pumping power.

Pressure drop in the headers is estimated by simulating one side of the header system. The header design from the rectangular channel MS design is used. In order to provide a factor of safety for flow distribution, the mass flow rate is increased by a factor of four. The resulting pressure drop in the header is 0.05 bar. Therefore, the channels are designed to have a pressure drop of 0.5 bar.

### 4.2.4 Design Parameters

The lower average fluid temperature and operating pressure, compared with SCO<sub>2</sub>, make SS an appropriate choice for the solid material (see section 4.1). A pitch of 1.5 is chosen as it shows higher heat transfer coefficient than a pitch of 2.0 in the single channel simulations. Note that the pitch was not limited by the

structural requirement as with the SCO<sub>2</sub> pin-fin design. The pin diameter is 314 micron. This is the minimum diameter required to meet the pressure drop goal according to the results of single channel simulations (see section 4.2.2). The etch depth is 150 micron. This results in a pin height of 300 micron. These dimensions are based on the limits of isotropic etching as discussed in section 3.1.1. The dimensions of the pin-fin array are 1 by 1 cm, based on the capacity of the solar simulator.

#### 4.2.5 Analysis

A CFD simulation is performed for the fluid region of the complete design. The solid region has not yet been modeled. Table 4.3 shows the key results of this simulations as well as some of the key design parameters. The pressure drop is lower than predicted by the single channel simulations. This could be due to inaccuracy in the full-design simulation due to lower grid resolution compared to the single-channel simulations. Future work should include investigation of the error in this simulation associated with grid resolution. Grid convergence studies performed for single channel geometries are discussed in section 5. The average channel wall temperature is used to predict the average temperature of the header surface using 1-D conduction. The temperature of the heated surface is then used to calculate efficiency. The resulting receiver and thermal efficiencies were 94.1% and 99.1%.

Figure 4.6 shows a plot of mass flow rate at individual pin-fin gaps at three locations in the pin-fin array. A gap is the flow area between two adjacent pin-fins. This flow area is perpendicular to the net flow direction in the array. There are a discrete number of gaps through which fluid can enter and exit the microchannel

pin diameter	314 micron
transverse pitch	1.5
Reynolds number	378
pressure drop	0.4 bar
heated surface temperature	838 K
receiver efficiency (95% emissivity)	94.1%
thermal efficiency	99.1%

Table 4.3: Parameters and results of the full-design CFD simulation of the MS pin-fin design.

array. Extracting the mass flow rate through each gap gives a measure of flow distribution. The distribution in mass flow rate at each location is fairly uniform.

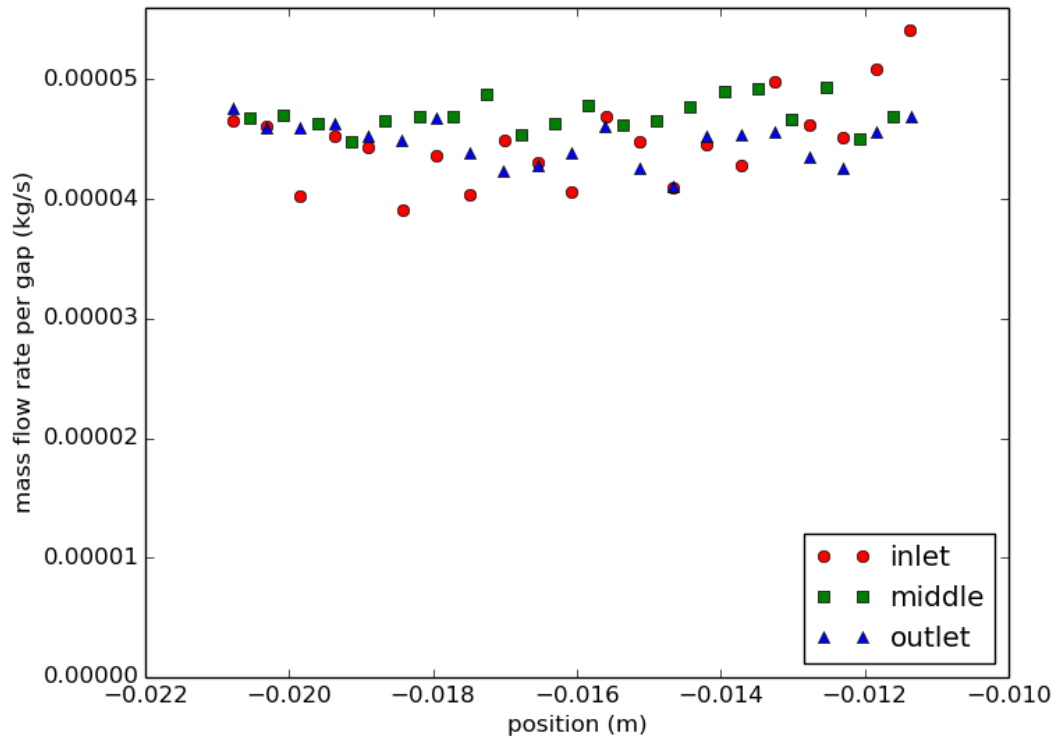


Figure 4.6: MS Pin-Fin Design: Plot of mass flow rate through individual pin-fin gaps at three locations along the microchannel array. A gap is the flow area between two adjacent pin-fins. Data is from a full-design CFD simulation.

## CHAPTER 5. ERROR ANALYSIS

---

### 5.1 Introduction

The following section discusses error analysis performed for the CFD simulations used in designing the receivers. One factor in determining the error of CFD simulations is grid resolution. A grid convergence study calculates error associated with grid resolution by comparing results at different resolutions. Because the SCO2 circular channel and rectangular channel designs were the first (and so far only) designs to be tested in the solar simulator, they were the first designs for which error analysis was performed. Error analysis for the SCO2 pin-fin and MS designs will follow in future work.

For both the SCO2 circular and rectangular channel designs, the geometry consisted of a single slice of the device containing one channel. The geometry contained both fluid and solid domains. The geometry also contained part of the header in order to capture the transition between channel and header flow. This geometry was identical to the single-channel simulation geometry used in designing the receiver. Uniform heat flux was applied to the incident surface.

Three simulations with identical geometries were performed. Each consecutive simulation had approximately 1.5 times higher grid resolution than the previous. The grid was refined uniformly in all directions and at all locations in the model. Figure 5.1 illustrates this by showing a cross-section of the geometry for each of the three grid resolutions.

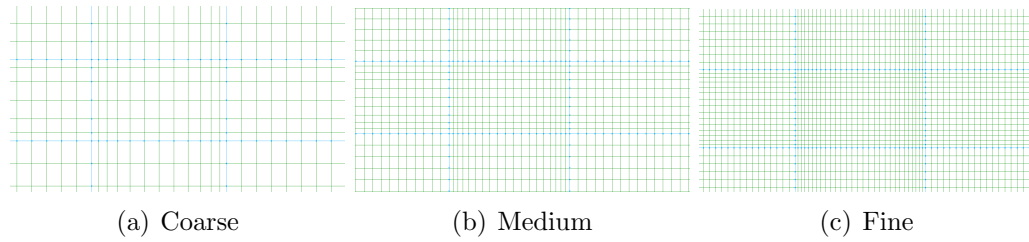


Figure 5.1: Cross-section of channel and surrounding solid showing the three grid resolutions.

In order to quantify error, a metric is measured in each of the three simulations. For this study, the metric was a point measurement of fluid-side heat-flux at the channel wall. Several locations along the length of the channel are used to get multiple error estimates. The solid-side heat flux was also measured to verify that it is equal to the fluid-side heat-flux. These heat-flux values were provided directly by the FLUENT software.

The heat-flux distribution on the channel walls is directly related to the temperature distribution in the device. Therefore, the error in the heat flux at the channel wall is directly related to that of the average temperature on the incident surface and, therefore, the efficiency. Also, the wall heat-flux is related to the velocity profile and turbulence level in the channel. Using the metric and average grid size for each of the three resolutions, the GCI (grid convergence index) is calculated and, from that, the error in the metric is calculated.

## 5.2 Results

Figure 5.2 shows a three-dimensional contour plot of heat flux at the fluid-solid interface for the rectangular channel design. In figure 5.2, the wall of the

channel closest to the incident surface can be seen. Fluid enters on the left and exits on the right. The region of high heat flux near the inlet of the channel is caused by the transition from the header to channel. The constriction and direction change going into the channel causes mixing and high velocity gradients.

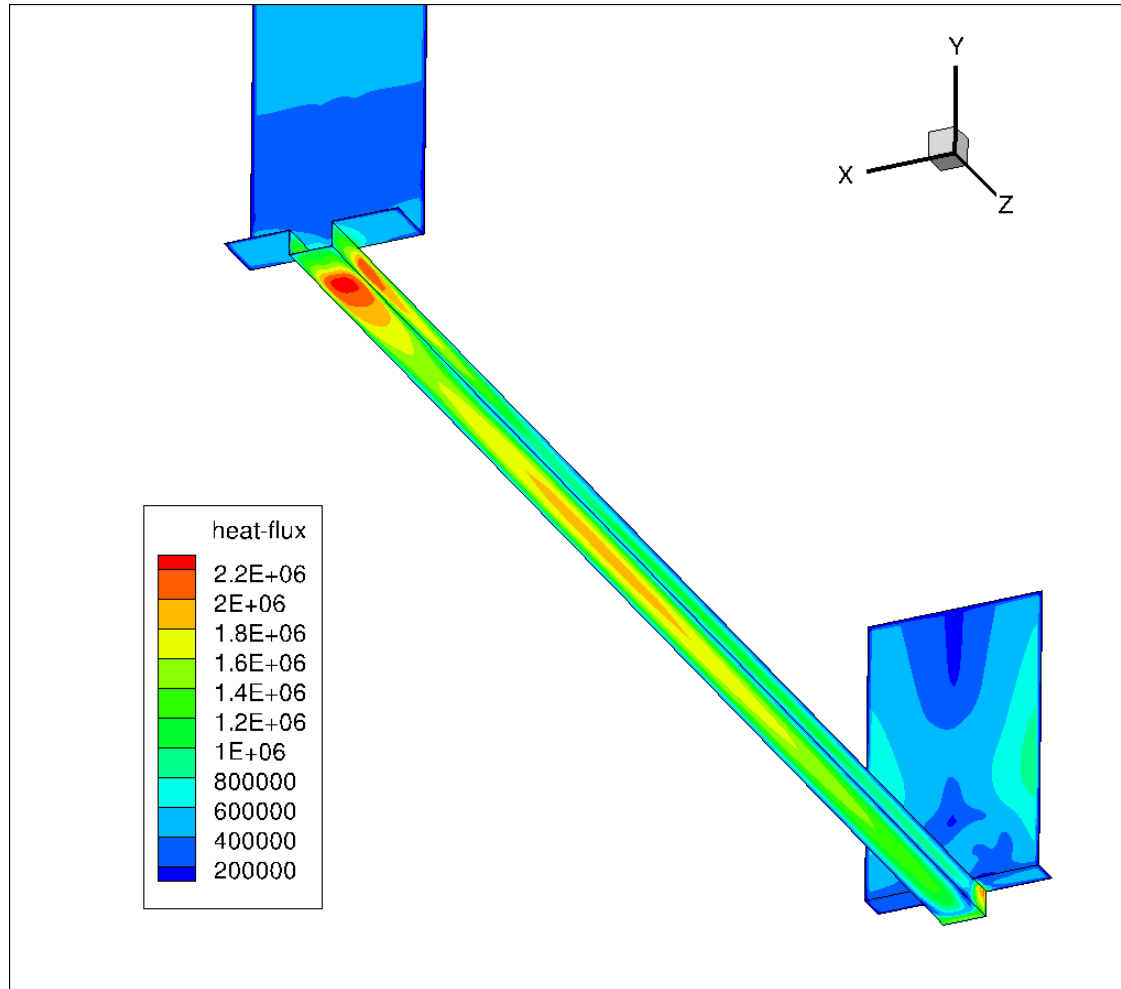


Figure 5.2: Three-dimensional contour plot of heat flux at the fluid-solid interface for the SCO2 rectangular channel design.

There is another region of relatively high heat flux at about halfway along the length of the channel. This is a consequence of heat conducting through the solid toward the inlet and outlet headers; some heat is transferred from solid to fluid in the headers. Heat from the irradiated surface conducts through the solid not only

toward the channel but also upstream and downstream parallel to the fluid flow in the channel. Upstream of this high flux region, heat flows upstream through the solid toward the inlet header; downstream of this region, heat flows downstream toward the outlet header. In this high heat flux region, heat flows direct toward the channel, with no upstream or downstream component. The circular channel design exhibited the same patterns of heat flux distribution.

In figure 5.3, the heat flux at a single point on the channel wall for the rectangular design is plotted against average grid size. The three data points correspond to the three grid resolutions. The coarsest grid corresponds to the right-most point and the finest grid corresponds to the left-most point.

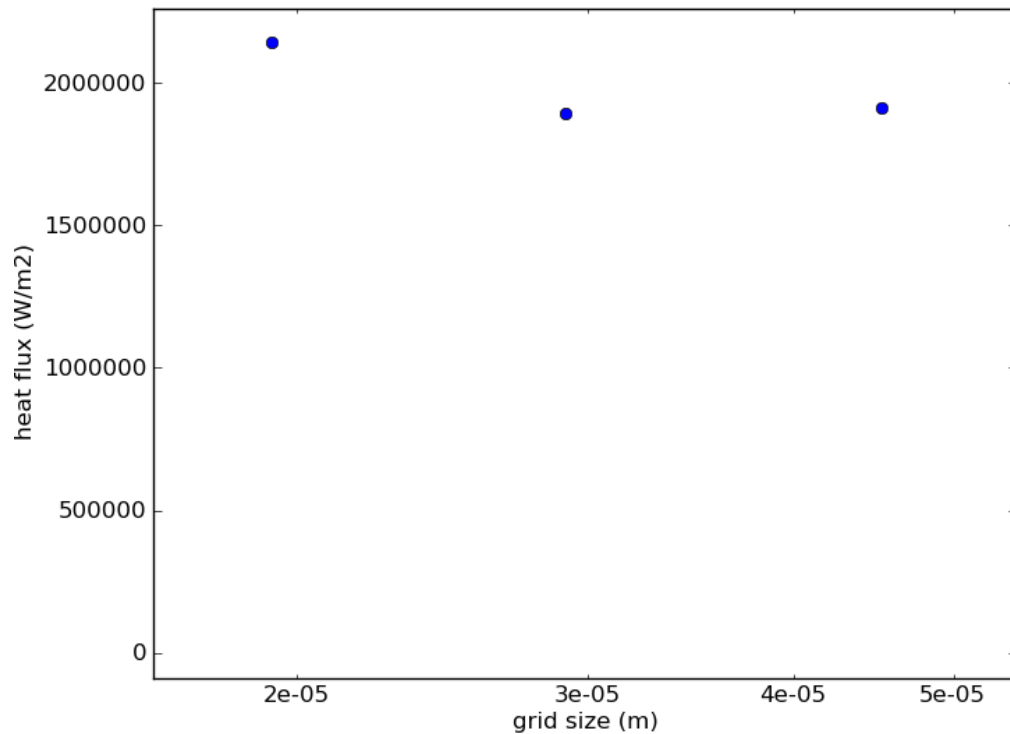


Figure 5.3: Plot of heat flux versus grid size at a single point on the channel wall for the SCO2 rectangular channel design.

For the rectangular channel design, the resulting error ranged from 0.8% to 0.9%. For the circular channel design, the resulting error was approximately 0.7%. The error was slightly different for each point on the channel wall.

## CHAPTER 6. EXPERIMENTAL VALIDATION

---

The following sections introduce experiments and experimental validation simulations. Experimental validation has been performed for one experimental case and will be performed for additional cases as experimental data becomes available.

### 6.1 Introduction

Experimental validation thus far has focused on the designs currently manufactured and tested. So far, only the SCO<sub>2</sub> rectangular design has sufficient experimental data. First, the experimental setup should be briefly explained. Figure 6.1 shows a side-view cross-section of a circular channel device and the experimental setup. Solar flux is incident on the top of the device, indicated by the yellow lines. These lines are angled, converging on the receiver, due to the shape of the reflector in the solar simulator. Some of the solar flux is incident directly on the insulation, indicated by the yellow lines on the far left and right. This caused problems in early experiments because heat was being absorbed by the device than was intended. A water-cooled metal plate was placed above the receiver surface (not in direct physical contact with the insulation) to block this extra radiation.

There are several experimental measurements relevant to validation. First is the fluid temperature and pressure at the inlet and outlet of the device. These values are measured in the inlet and outlet tubes outside of the receiver, but as close as possible to it. The inlet and outlet tubes are insulated, though figure 6.1

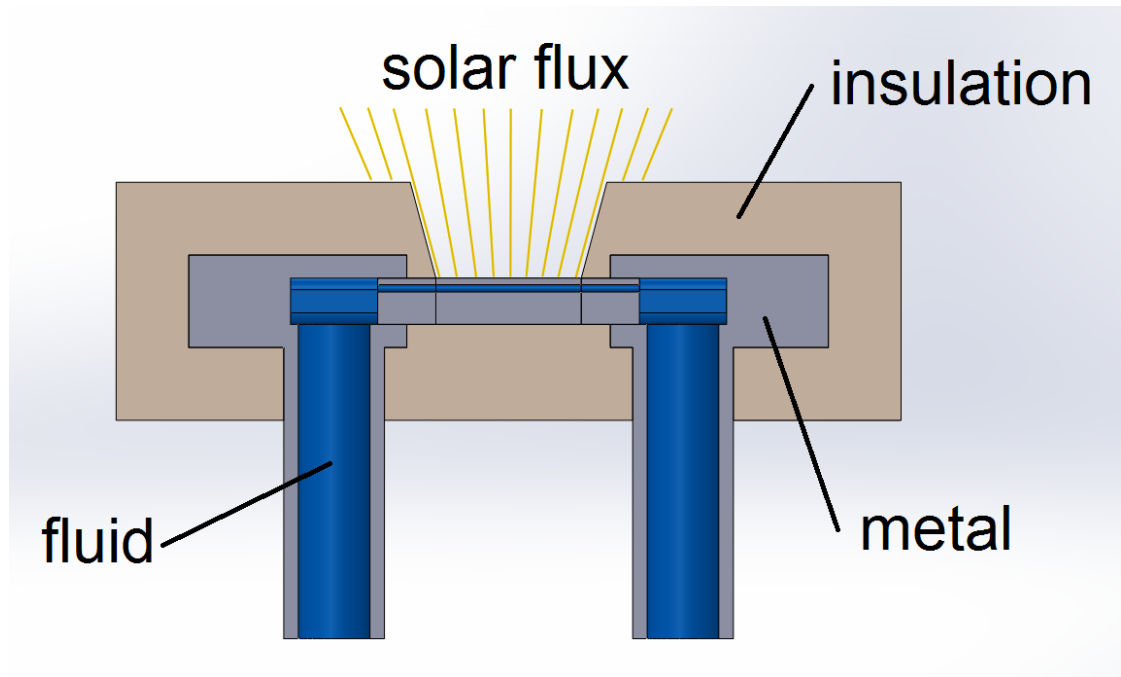


Figure 6.1: Diagram of experimental setup

does not show this insulation. Second is the map of incident solar flux. This map is a set of heat flux measurements on a two-dimensional grid that covers the heated area. The map is generated by moving a small heat flux meter around the heated area using an xy traverse. Third is surface temperature measurements at several locations on the exterior of the device, placed at the interface between metal and insulation. Quantities from simulation which need to be validated are pressure drop, receiver efficiency, and heat loss through the insulated surfaces.

## 6.2 Experiments

Experiments performed so far can be put into two categories: “unheated” and “heated”. The following sections explain these two types of experiment and

their purpose.

### 6.2.1 *Experiments with the Device Unheated*

In “unheated” experiments, the lamp in the solar simulator is off. The region of the exterior of the device which is intended to absorb solar flux (the heated area) is insulated. Hot fluid enters the device and cold fluid exits. Thermocouples are attached to the exterior walls underneath the insulation at various points. The global heat transfer for the device in this experiment is

$$\dot{m}\Delta h = q_{\text{loss,ins}} \quad (6.1)$$

where  $\dot{m}$  is mass flow rate, measured by a flow-meter;  $\Delta h$  is enthalpy change of the fluid, calculated using the inlet and outlet temperature of the fluid; and  $q_{\text{loss,ins}}$  is the heat loss through the insulated exterior walls of the device. Using several such experiments with different inlet temperatures, a “heat loss curve” was created. This is a correlation for heat loss through the insulated walls versus average body temperature (average of the thermocouple readings). Figure 6.2 plots thermocouple measurements versus average body temperature. The plot shows an approximately linear relationship between each of the individual thermocouple measurements and the average body temperature.

### 6.2.2 *Experiments with the Device Heated*

In “heated” experiments, the lamp is on. Cold fluid enters the device and hot fluid exits. The thermocouples mentioned in the previous section remain attached.

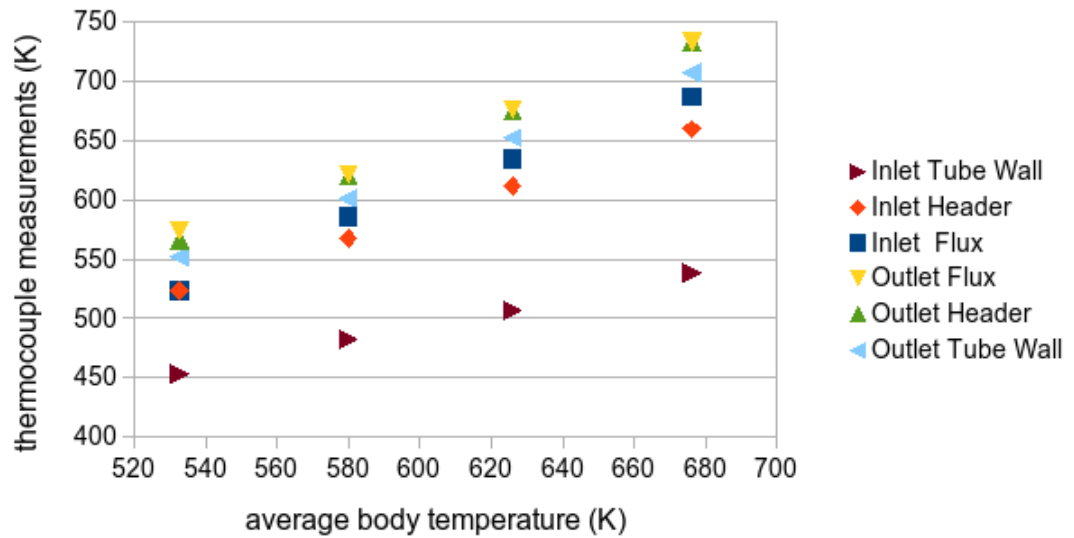


Figure 6.2: Plot of thermocouple measurements for “unheated” experiments versus average body temperature.

The measured flux map is used to estimate the incident flux.

The “heat loss curve” is used to estimate heat loss through the insulated walls. Note that the temperature distribution in the solid material in the “heated” and “unheated” experiments is very different; fluid is heated in one and cooled in the other. This could mean that the relationship between the average body temperature and heat loss through the insulation is also different. This could be a source of error in the estimated heat loss through the insulated walls. Also, the average body temperature in the “heated” experiments is much higher than in the “unheated” experiments. Therefore, the “heat loss curve” has to be extrapolated to the temperatures seen in the “heated” experiments. Since the “unheated” experiments are currently the only method for the team to measure the heat loss through the insulation, this error cannot yet be quantified.

The global heat transfer equation for “heated” experiments is

$$q_{\text{inc}} = \dot{m}\Delta h + q_{\text{loss,ins}} + q_{\text{loss,irr}} \quad (6.2)$$

where  $q_{\text{inc}}$  is the heat input from the solar simulator and  $q_{\text{loss,irr}}$  is heat loss from the irradiated surface. Heat loss from the irradiated surface is calculated from this equation and used to calculate efficiency. Thermal efficiency is

$$\eta_{th} = \frac{\dot{m}\Delta h}{q_{\text{inc}} - q_{\text{loss,ins}} - q_{\text{loss,ref}}} \quad (6.3)$$

where  $q_{\text{loss,ref}}$  is the heat loss from reflection.

### 6.3 Results

CFD simulations are performed which match the conditions in the “heated” experiments. The mass flow rate and inlet temperature are set equal to experimental measurement. In the simulation, no heat loss is modeled from the heated surface or the insulated surfaces; all heat incident to the receiver surface is absorbed by the fluid. This incident heat is set as a constant heat flux boundary condition on the heated surface. The global energy balance for the simulation is

$$\dot{m}(h_{\text{out}} - h_{\text{in}}) = q_{\text{in}} \quad (6.4)$$

where  $\dot{m}$  is mass flow rate,  $h_{\text{out}}$  is the enthalpy at the outlet,  $h_{\text{in}}$  is the enthalpy at the inlet, and  $q_{\text{in}}$  is the heat input. The mass flow rate, inlet enthalpy, and the heat input are all directly controlled using boundary conditions. Therefore, the outlet enthalpy is also directly controlled, which determines outlet temperature.

Receiver efficiency is calculated using the average temperature of the heated surface and compared to the experimentally measured efficiency from (6.3).

Experimental data used for validation comes from a recent set of experiments for a SCO<sub>2</sub> rectangular design. Only one of the experimental cases has been analyzed so far. Table 6.1 presents data from this experimental case and the accompanying simulation. In the experimental data, mass flow rate and incident flux are varied in order to vary the exit temperature. The experimental case presented in the table had one of the highest thermal efficiencies due to its high incident flux.

	mass flow rate (g/s)	heat in (W)	exit temperature (K)	thermal efficiency
experiment	0.910	429	927	0.984
simulation	0.910	276	927	0.931

Table 6.1: Experimental data and validation simulation results for SCO<sub>2</sub> rectangular design.

Using experimental results, the thermal efficiency is estimated to be 98.4%. The CFD simulation, however, predicted a thermal efficiency of only 93.1%, a difference of 5.4%. This difference is within the combined uncertainty of the two values of efficiency. Sources of error include the experimental measurements; the CFD simulation; the “heat loss curve” (curve fit error and experimental error associated with the “unheated” experiments); and estimates of constants (emissivity of the irradiated surface, natural convection coefficient, etc.).

Pressure drop has not yet been measured in experiments. When it is, it will be compared with simulation results.

## CHAPTER 7. SCALED-UP DESIGN

---

A design concept is sought for a 1 m<sup>2</sup> receiver panel. The panel will consist of unit cells based on previously discussed designs. The SCO<sub>2</sub> rectangular channel and pin-fin designs and the MS designs can be made scalable. The header channels which extended beyond the irradiated area can be rearranged to keep them within that area. This does not require significant change to design, nor should it significantly affect pressure drop or efficiency. Using, for example, a 2 by 2 cm unit cell, the large panel would have 50 by 50 cells for a total of 2500 cells. The individual unit cell inlets and outlets will be connected by additional header plates. The challenge is to connect the 2500 inlets and 2500 outlets and have low pressure drop in the header and, therefore, adequate flow distribution to each of the unit cells. At the time of writing, there are two concepts.

The first is a multi-layer branching header. In this concept, a single header channel repeatedly branches into smaller channels. Such a design could take many different forms, depending on how many new branches are formed at each level. The obvious choice for a square panel is for each header channel to branch into four smaller header channels. This is depicted in the following figure. One disadvantage of this concept is that it would require several additional header plates, increasing the size and complexity of the receiver. For example, to have at least 50 unit cells in each direction, the header channel would have to branch six times, requiring at least six additional header plates. Figure 7.1 shows a fluid volume rendering of a branching channel design; the solid material is not shown. The model in the figure contains only 4 by 4 unit cells in order to aid understanding of the concept.

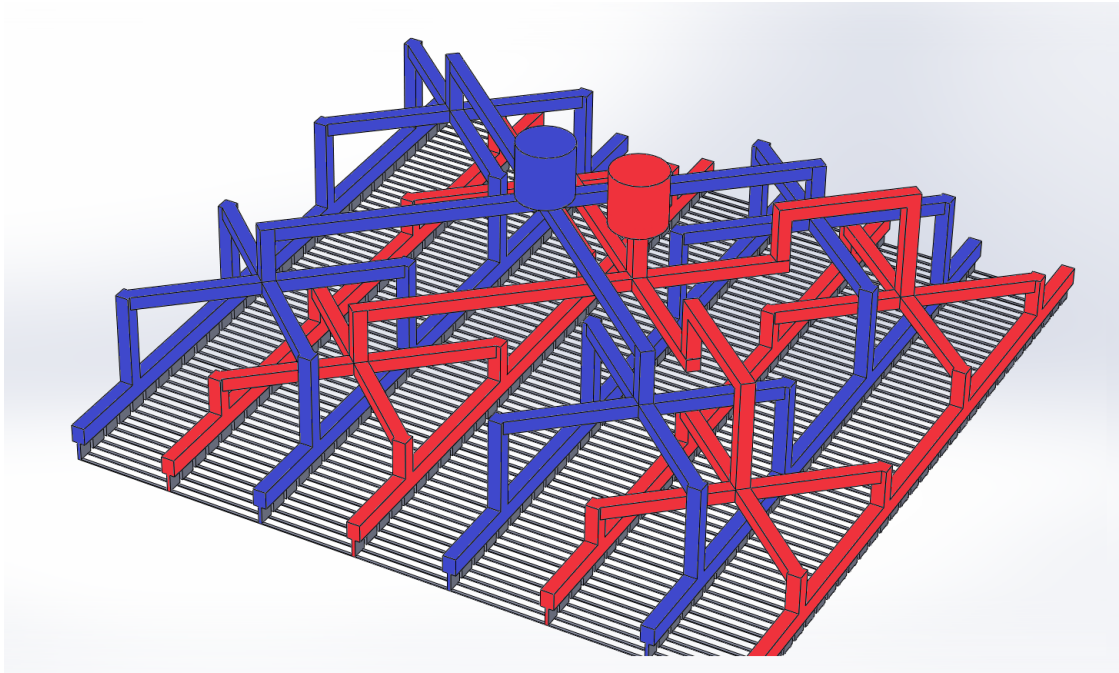


Figure 7.1: Fluid volume rendering of a branching channel header. The large cylindrical sections at the top are the global inlet and outlet tubes. The small parallel sections at the bottom are the microchannels. The inlet header channels are blue and the outlet header channels are red.

The second is a single-layer pin-fin type header. In this concept, there are two pin-fin arrays: one for the cold fluid and one for the hot. Each array would cover the entire area of the  $1 \text{ m}^2$  panel. All of the unit cell inlets and outlets would connect to the pin-fin arrays, along with a large inlet and outlet hole near the center of the arrays. Figure 7.2 shows the concept for a 10 by 10 unit cell panel. The challenge for this concept is to have sufficient flow area to have low pressure drop and also have sufficient bonding area to withstand operating pressure of fluid. As with the receiver designs, this will be a greater issue for  $\text{SCO}_2$  than for MS.

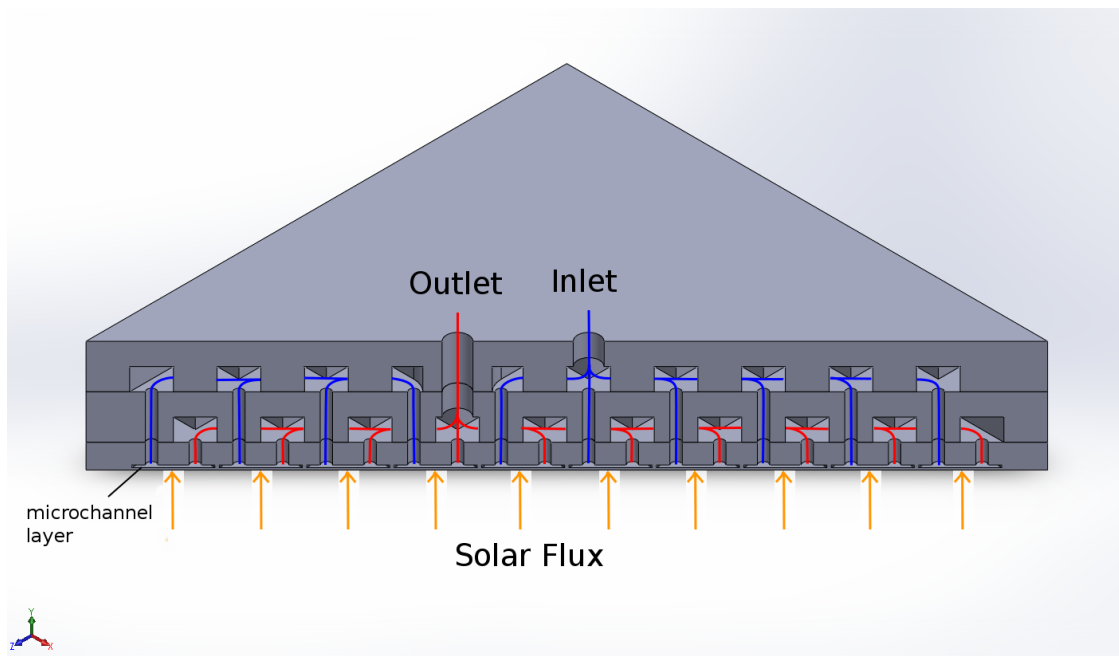


Figure 7.2: Cutaway view of the pin-fin header channel concept. Blue arrows indicate cold fluid, red arrows indicate hot fluid, and yellow arrows indicate solar flux.

## CHAPTER 8. CONCLUSION

---

Based on CFD simulations, the highest receiver efficiencies were 89.7% for SCO<sub>2</sub> and 94.3% for MS (assuming 95% emissivity). These values are close to the goal and the theoretical limits for the given fluid temperature. The receiver efficiency is highly dependent on the emissivity of surface. Investigation of the emissivity for different surface treatments is important to increasing receiver efficiency but was beyond the scope of this work.

The pressure drop goal was satisfied in all cases. The SCO<sub>2</sub> circular channel and MS rectangular channel designs had pressure drop much lower than the target value. This was due to manufacturing limitations which prevented channels of smaller size. Because receiver efficiency generally increases with increased pressure drop, further investigation into what is a maximum acceptable pressure drop should be conducted.

The minimum structural safety factor for any design was 1.3 (SCO<sub>2</sub> rectangular and pin-fin designs). And to date, there have been no structural failures during testing. However, a higher safety factor will probably be necessary for a large scale implementation and long-term operation.

Flow distribution was adequate in all designs. All designs showed noticeable variation in flow rate, but none showed regions of higher temperature as a result. Flow distribution will likely be a most substantial issue when designing a larger-scale receiver.

None of the manufactured devices are directly scalable. However, the SCO<sub>2</sub> rectangular channel and pin-fin designs and the MS designs can be scalable with

some modification to the header (see section 7). Design concepts for a scaled-up design have been developed. However, the task of ensuring flow distribution using CFD simulation has not begun.

Based on the simulation results, microchannels are a viable technology for CSP receivers and can achieve high efficiency with reasonable pressure drop. This work and the successful testing of the manufactured devices should lead to the development of larger scale microchannel CSP receivers.

## 8.1 Recommendation for Future Work

There are several areas of research which could further increase the efficiency of a microchannel solar receiver and make such a device more practical for large scale application. For increasing efficiency, one approach would be to eliminate some of the manufacturing limitations. This would allow for higher aspect ratio channels. Increasing aspect ratio increases the surface area of the channels while maintaining a small diffusion length. As discussed in section 3.2.2, there is an optimal aspect ratio that yields maximum heat transfer coefficient. Allowing for higher pressure drop would also increase efficiency by allowing smaller overall channel dimensions and higher flow rates. The tradeoff between increased efficiency and increased pumping power should be studied. Other channel layouts could also be tested, such as branching channels. Though unrelated to the microchannels themselves, the absorptivity of the receiver surface is a major contributor to receiver efficiency. Research into coatings or surface treatments should be pursued in order to maximize absorption of incoming radiation. Finally, research into the solid materials and manufacturing processes used in creating the microchannels could make the receiver more cost effective and practical.

## APPENDIX A. EQUATIONS

---

### A.1 Pin-Fin Geometry

Figure A.1 shows a top-view diagram of a circular, staggered pin-fin array geometry and key dimensions. There are three spacing dimensions:  $S_T$  is transverse spacing,  $S_L$  is longitudinal spacing, and  $S_D$  is diagonal spacing. In a uniformly spaced array,  $S_T$  and  $S_D$  are equal and

$$S_L = \frac{\sqrt{3}}{2} S_T \quad (\text{A.1})$$

Each spacing dimension has an accompanying pitch, defined as the ratio of the spacing to the pin diameter, and denoted  $P_T$ ,  $P_L$ , and  $P_D$ . Similar to spacing, there are three edge-to-edge distance dimensions:  $G_T$ ,  $G_L$ , and  $G_D$ . These are the distances between the outer edges of adjacent pins. Again, in a uniformly spaced array, the transverse and diagonal distances are equal. We are only concerned with the transverse distance, which we will call  $G$ .

$$G = G_T = G_D \quad (\text{A.2})$$

$$= D - S_T \quad (\text{A.3})$$

$$= D - P_T D \quad (\text{A.4})$$

$$= D(1 - P_T) \quad (\text{A.5})$$

In a pin-fin array, multiple cross-sectional areas of the fluid can be defined. One cross-sectional area is of interest because it has the highest average velocity. This area is between the two top-most pins (where the  $G$  dimension is marked). The area is

$$A_1 = \frac{\pi}{4} G_T^2 \quad (\text{A.6})$$

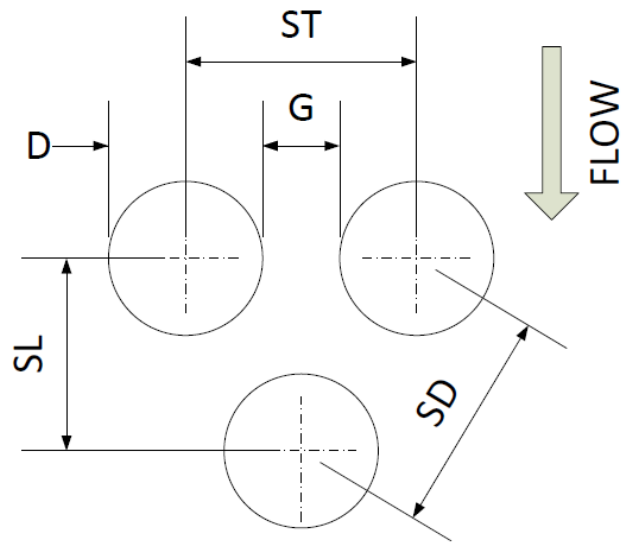


Figure A.1: Top-view diagram of a circular staggered pin-fin array with key dimensions.

## A.2 Fluid Dynamics and Heat Transfer

### A.2.1 Mass Flow Rate

Global heat transfer, ignoring all loss terms, is

$$\dot{m}\Delta h = q'' A \quad (\text{A.7})$$

where  $\dot{m}$  is the mass flow rate,  $\Delta h$  is the change in enthalpy from inlet to outlet,  $q''$  is the average heat flux, and  $A$  is the receiver area. Mass flow rate is given by

$$\dot{m} = \frac{q'' A}{\Delta h} \quad (\text{A.8})$$

The enthalpy change is given by

$$\Delta h = \int_{T_{in}}^{T_{out}} c_p dT \quad (\text{A.9})$$

where  $T$  is temperature and  $c_p$  is the temperature-dependent specific heat.

### A.2.2 Reynolds Number

The Reynolds number is used to determine if the flow is laminar or turbulent and in correlations for pressure drop and heat transfer. The equation for hydraulic diameter Reynolds number is

$$Re = \frac{\rho v D_h}{\mu} \quad (\text{A.10})$$

where  $\rho$  is the density,  $v$  is the average velocity, and  $\mu$  is the dynamic viscosity.  $D_h$  is the hydraulic diameter given by

$$D_h = \frac{4A_{cs}}{P} \quad (\text{A.11})$$

where  $A_{cs}$  is the cross-sectional area and  $P$  is the perimeter.

### **Circular, Staggered, Uniformly-Spaced Pin-Fin Array**

In a circular, staggered, uniformly-spaced, pin-fin array, the velocity used is the average velocity through the smallest cross-sectional area (described in section A.1) given by

$$v_1 = \frac{\dot{m}}{\rho A_1} = \frac{4\dot{m}}{\rho \pi G_T^2} = \frac{4\dot{m}}{\rho \pi D^2 (1 - P_T)^2} \quad (\text{A.12})$$

The hydraulic diameter is equal to the pin diameter. So the Reynolds number is

$$Re = \frac{\rho v_1 D}{\mu} \quad (\text{A.13})$$

$$= \frac{4\dot{m}}{\mu \pi D (1 - P_T)^2} \quad (\text{A.14})$$

### *A.2.3 Pressure Drop*

#### **Rectangular Channel**

Pressure drop for fully-developed flow in a rectangular channel is given by

$$\Delta p = f \frac{L}{D_h} \frac{\rho v^2}{2} \quad (\text{A.15})$$

where  $f$  is Darcy friction factor,  $L$  is channel length,  $D_h$  is hydraulic diameter,  $\rho$  is density and  $v$  is average velocity. Replacing velocity with mass flow rate gives

$$\Delta p = f \frac{L}{D_h} \frac{\rho}{2} \left( \frac{\dot{m}}{\rho A_{cs} N} \right)^2 = f \frac{L}{D_h} \frac{1}{2\rho} \left( \frac{\dot{m}}{A_{cs} N} \right)^2 \quad (\text{A.16})$$

where  $N_T$  is the number of channels. Substituting (A.8) for mass flow rate gives

$$\Delta p = f \frac{L}{D_h} \frac{1}{2\rho} \left( \frac{\frac{q'' A}{\Delta h}}{A_{cs} N} \right)^2 = f \frac{L}{D_h} \frac{1}{2\rho} \left( \frac{q'' A}{A_{cs} N \Delta h} \right)^2 \quad (\text{A.17})$$

Substituting additional geometric relations gives

$$\Delta p = f \frac{L}{D_h} \frac{1}{2\rho} \left( \frac{q'' W L}{A_{cs} N \Delta h} \right)^2 = f \frac{L^3}{D_h} \frac{1}{2\rho} \left( \frac{q'' W}{A_{cs} N \Delta h} \right)^2 \quad (\text{A.18})$$

where  $W$  is the width of the array (direction perpendicular to flow). For laminar flow, Shah and London [10] give a relationship between Fanning friction factor, Reynolds number, and aspect ratio

$$f Re = 24(1 - 1.3553\alpha + 1.9467\alpha^2 - 1.7012\alpha^3 + 0.9564\alpha^4 - 0.2537\alpha^5) \quad (\text{A.19})$$

For turbulent flow, the hydraulic diameter Reynolds number and the Moody chart can be used to get an estimate of friction factor.

### Pin-Fin Array

The pressure drop for fully-developed flow in a uniform pin-fin array is

$$\Delta p = f N_L \frac{\rho v^2}{2} \quad (\text{A.20})$$

where  $f$  is Darcy friction factor,  $N_L$  is the number of channels in the direction of flow,  $\rho$  is the fluid density, and  $v$  is the maximum average velocity (average velocity through the smallest cross-sectional area). Substituting the relationship between mass flow rate and velocity gives

$$\Delta p = f N_L \frac{\rho}{2} \left( \frac{\dot{m}}{\rho A_1 N_T} \right)^2 = f N_L \frac{1}{2\rho} \left( \frac{\dot{m}}{A_1 N_T} \right)^2 \quad (\text{A.21})$$

where  $A_1$  is the cross-sectional area defined in appendix A.2.2. Substituting (A.8) for mass flow rate gives

$$\Delta p = f N_L \frac{1}{2\rho} \left( \frac{\left( \frac{q'' A}{\Delta h} \right)}{A_1 N_T} \right)^2 = f N_L \frac{1}{2\rho} \left( \frac{q'' A}{A_1 N_T \Delta h} \right)^2 \quad (\text{A.22})$$

Substituting additional geometric relations gives

$$\Delta p = f \frac{L}{S_L} \frac{1}{2\rho} \left( \frac{q'' W L}{A_1 \frac{W}{S_T} \Delta h} \right)^2 = f \frac{L^3}{S_L} \frac{1}{2\rho} \left( \frac{q'' S_T}{A_1 \Delta h} \right)^2 \quad (\text{A.23})$$

where  $W$  is the width of the array (direction perpendicular to flow).

Many correlations for friction factor have been reported in literature. However, the results vary greatly between different authors. And most of this literature concerns only laminar flow. Correlations for banks of tubes have been well established for both laminar and turbulent flow. However, since micro-pin-fin height is generally short compared to their diameter, the effect of the walls makes use of such correlations invalid.

## A.2.4 Heat Transfer

### Forced Convection

The general form for convection heat transfer is

$$q = hA_{\text{chan sur}}\Delta T = hA_{\text{chan sur}}(T_{\text{wall}} - T_{\text{bulk fluid}}) \quad (\text{A.24})$$

where  $h$  is heat transfer coefficient,  $A_{\text{chan sur}}$  is the surface area of the channel,  $T_{\text{wall}}$  is the wall temperature, and  $T_{\text{bulk fluid}}$  is the average temperature of the fluid. The heat transfer coefficient can be determined from the Nusselt number

$$Nu_{D_h} = \frac{hD_h}{k_f} \quad (\text{A.25})$$

where  $D_h$  is the hydraulic diameter and  $k_f$  is the thermal conductivity of the fluid. Correlations for Nusselt number based on Reynolds number and channel dimensions can be found in literature. Solving for the temperature of the wall gives

$$T_{\text{wall}} = \frac{q}{hA_{\text{chan sur}}} + T_{\text{bulk fluid}} \quad (\text{A.26})$$

### Conduction

The general form for one-dimensional conduction heat transfer is

$$q = -k_s \frac{\Delta T}{\Delta x} \quad (\text{A.27})$$

where  $k_s$  is the thermal conductivity of the solid,  $\Delta T$  is the temperature difference across the solid, and  $\Delta x$  is the thickness of the solid. The temperature difference

across a section of solid material is

$$\Delta T = \frac{q\Delta x}{k_s} \quad (\text{A.28})$$

### A.3 Efficiency

#### A.3.1 Receiver Efficiency

Receiver efficiency is given by

$$\eta = \frac{q_{\text{fluid}}}{q_{\text{inc}}} \quad (\text{A.29})$$

where  $q_{\text{fluid}}$  is the heat absorbed by the fluid and  $q_{\text{inc}}$  is the total incident solar flux. The heat absorbed by the fluid can be substituted to get

$$\eta = \frac{q_{\text{inc}} - q_{\text{loss}}}{q_{\text{inc}}} = 1 - \frac{q_{\text{loss}}}{q_{\text{inc}}} \quad (\text{A.30})$$

where  $q_{\text{loss}}$  is the total heat loss from the device. Alternatively, the denominator can be expanded to get

$$\eta = \frac{q_{\text{fluid}}}{q_{\text{fluid}} + q_{\text{rad}} + q_{\text{conv}} + q_{\text{ref}}} \quad (\text{A.31})$$

where  $q_{\text{rad}}$  is radiation loss,  $q_{\text{conv}}$  is convection loss, and  $q_{\text{ref}}$  is reflection loss from the heated surface of the receiver. This assumes no loss through the other exterior surfaces of the device. The reflection loss can be written as

$$q_{\text{ref}} = \rho q_{\text{inc}} = (1 - \epsilon)q_{\text{inc}} \quad (\text{A.32})$$

This is then substituted into the equation for the total incident solar flux

$$q_{\text{inc}} = q_{\text{fluid}} + q_{\text{rad}} + q_{\text{conv}} + (1 - \epsilon)q_{\text{inc}} \quad (\text{A.33})$$

$$(1 - 1 + \epsilon)q_{\text{inc}} = \epsilon q_{\text{inc}} = q_{\text{fluid}} + q_{\text{rad}} + q_{\text{conv}} \quad (\text{A.34})$$

$$q_{\text{inc}} = \frac{1}{\epsilon}(q_{\text{fluid}} + q_{\text{rad}} + q_{\text{conv}}) \quad (\text{A.35})$$

This can be used to give a new form for the receiver efficiency

$$\eta = \frac{q_{\text{fluid}}}{\frac{1}{\epsilon}(q_{\text{fluid}} + q_{\text{rad}} + q_{\text{conv}})} = \frac{\epsilon q_{\text{fluid}}}{q_{\text{fluid}} + q_{\text{rad}} + q_{\text{conv}}} \quad (\text{A.36})$$

### A.3.2 Thermal Efficiency

We define thermal efficiency as the efficiency ignoring reflection losses

$$\eta = \frac{q_{\text{fluid}}}{q_{\text{inc}} - q_{\text{ref}}} \quad (\text{A.37})$$

$$\eta = \frac{q_{\text{fluid}}}{q_{\text{inc}} + q_{\text{rad}} + q_{\text{conv}}} \quad (\text{A.38})$$

### A.3.3 Estimation of Constants

Several constants appear in the efficiency equations and must be determined. The emissivity used in the presented results is 95%. This is based on the reported properties of pyromark paint [23].

The coefficient for natural convection is estimated using correlations for nat-

ural convection for a horizontal plate [24].

$$\overline{Nu}_L = \begin{cases} 0.54Ra_L^{1/4} & (10^4 < Ra < 10^7) \\ 0.15Ra_L^{1/3} & (10^7 < Ra < 10^{11}) \end{cases} \quad (\text{A.39})$$

where  $Ra_L$  is the Rayleigh number

$$Ra_L = Gr_L Pr = \frac{g\beta(T_s - T_\infty)L^3}{\nu\alpha} \quad (\text{A.40})$$

where  $g$  is the acceleration due to gravity,  $\beta$  is the volumetric thermal expansion coefficient of the fluid,  $T_s$  is the surface temperature,  $T_\infty$  is the ambient temperature,  $L$  is the characteristic length,  $\nu$  is the kinematic viscosity of the fluid, and  $\alpha$  is the thermal diffusivity of the fluid.

The ambient temperature for both radiation and natural convection are, at first, set equal to room temperature. Later, experimental measurements of the surface of the reflector and the air near the heated surface are used.

### A.3.4 Overall Efficiency

It is useful to examine the relationship between overall plant efficiency and receiver temperature and other design parameters. We can derive an equation for the overall efficiency of a CSP plant by combining cycle efficiency and receiver efficiency. We will assume cycle efficiency equal to the Carnot efficiency. Carnot efficiency is

$$\eta_{\text{Carnot}} = 1 - \frac{T_C}{T_H} \quad (\text{A.41})$$

where  $T_H$  is the temperature of the receiver (assumed to be close to the peak temperature of the working fluid) and  $T_C$  is the temperature of the surroundings (we will use 293.15 K).

For receiver efficiency, convection losses are ignored; only reflection and radiation losses are considered.

$$\eta_{\text{rec}} = \frac{q_{\text{inc}} - q_{\text{rad}} - q_{\text{ref}}}{q_{\text{inc}}} \quad (\text{A.42})$$

$$= \frac{q_{\text{inc}} - q_{\text{rad}} - (1 - \epsilon)q_{\text{inc}}}{q_{\text{inc}}} \quad (\text{A.43})$$

$$= \frac{\epsilon q_{\text{inc}} - q_{\text{rad}}}{q_{\text{inc}}} \quad (\text{A.44})$$

$$= \epsilon - \frac{q_{\text{rad}}}{q_{\text{inc}}} \quad (\text{A.45})$$

$$= \epsilon - \frac{A\sigma\epsilon(T_H^4 - T_C^4)}{Aq_{\text{inc}}''} \quad (\text{A.46})$$

$$= \epsilon \left( 1 - \frac{\sigma}{q_{\text{inc}}''} (T_H^4 - T_C^4) \right) \quad (\text{A.47})$$

$$= \epsilon \left( 1 - \frac{\sigma T_C^4}{q_{\text{inc}}''} \left( \frac{T_H^4 - T_C^4}{T_C^4} \right) \right) \quad (\text{A.48})$$

$$= \epsilon \left( 1 - K \left( \left( \frac{T_H}{T_C} \right)^4 - 1 \right) \right) \quad (\text{A.49})$$

A dimensionless constant  $K$  is used to simplify the equation.

$$K = \frac{\sigma T_C^4}{q_{\text{inc}}''} \quad (\text{A.50})$$

The numerator of  $K$  is the heat flux emitted by a black body at  $T_C$  and the denominator is the solar flux incident on the receiver.

The overall plant efficiency is the product of the cycle and receiver efficiency

$$\eta = \left( 1 - \frac{T_C}{T_H} \right) \epsilon \left( 1 - K \left( \left( \frac{T_H}{T_C} \right)^4 - 1 \right) \right) \quad (\text{A.51})$$

The derivative of efficiency with respect to  $T_H$  is

$$\frac{\partial \eta}{\partial T_H} = \frac{\epsilon}{T_C^4 T_H^2} (T_C^5 (K + 1) + 3KT_C T_H^4 - 4KT_H^5) \quad (\text{A.52})$$

Using the derivative, a contour plot of maximum efficiency versus  $K$  and emissivity is created (see figure A.2). The overall efficiency increases with increasing emissivity and decreasing  $K$ .  $K$  can be decreased by increasing the incident solar flux.

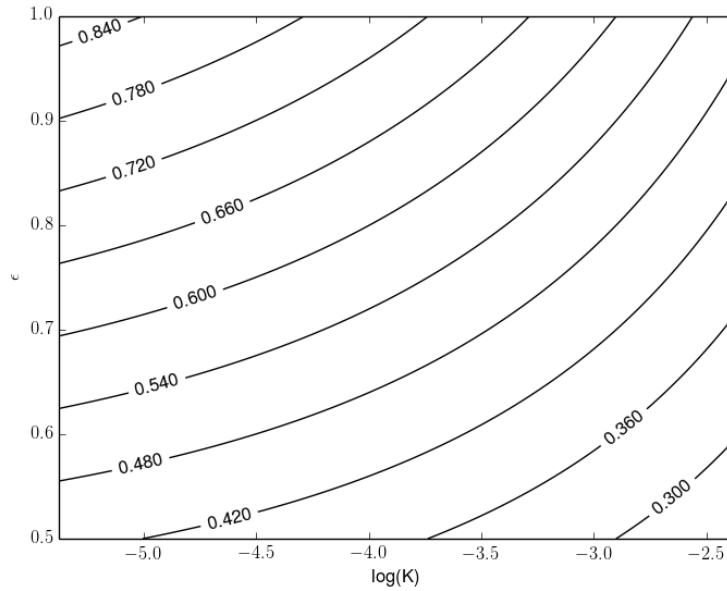


Figure A.2: Contour plot of maximum efficiency versus  $K$  and emissivity.

$T_{H,1}$ , the temperature of the receiver corresponding to the maximum efficiency, is a function of only  $K$ . Figure A.3 plots this relationship.

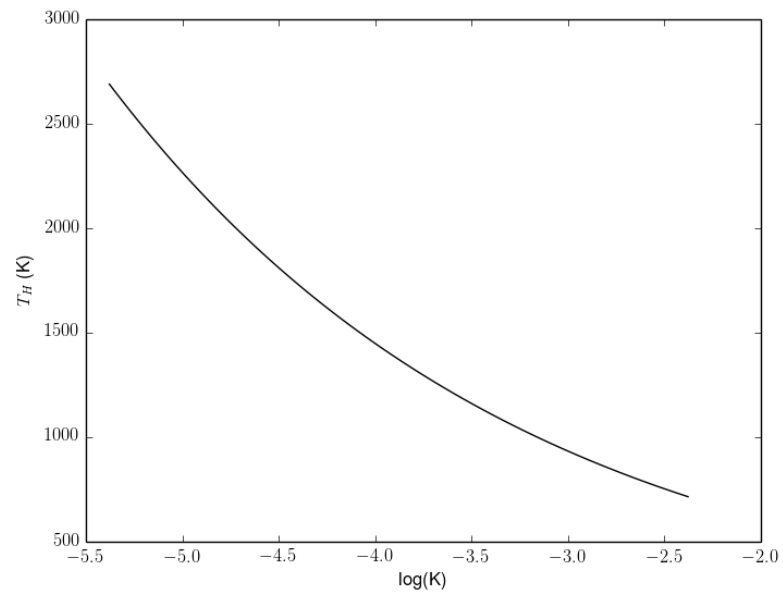


Figure A.3: Plot of receiver temperature at maximum efficiency versus  $K$ .

## APPENDIX B. MATERIALS

---

### B.1 Carbon-Dioxide

Properties for carbon-dioxide are curve-fit to polynomial functions of temperature from EES data. EES data comes from various sources [25, 26, 27]. The temperature range is centered around the inlet and outlet temperature. Properties are evaluated at a pressure of 120 bar.

	Inlet (773 K)	Average (848 K)	Outlet (923 K)
Density (kg/m <sup>3</sup> )	81.1	73.5	67.3
Specific Heat (J/kg K)	1.20E3	1.22E3	1.24E3
Dynamic Viscosity (Pa s)	$3.50E - 5$	$3.73E - 5$	$3.96E - 5$
Thermal Conductivity (W/m K)	$5.72E - 2$	$6.23E - 2$	$6.73E - 2$

Table B.1: Properties of carbon-dioxide at 120 bar and at the inlet, average, and outlet temperature of the fluid.

### B.2 Dynalene MS-1

Some properties for Dynalene MS-1 are curve fit to polynomial functions of temperature [6]. Dynamic viscosity and thermal conductivity are not reported to change significantly with temperature.

	Inlet (573 K)	Average (723 K)	Outlet (873 K)
Density (kg/m <sup>3</sup> )	1.78E3	1.72E3	1.66E3
Specific Heat (J/kg K)	1.54E3	1.42E3	1.29E3
Dynamic Viscosity (Pa s)	1.9E3	1.9E3	1.9E3
Thermal Conductivity (W/m K)	0.48	0.48	0.48

Table B.2: Properties of Dynalene MS-1 at the inlet, average, and outlet temperature of the fluid.

### B.3 Stainless Steel

Table B.4 lists relevant properties of 316 Stainless Steel. This data comes from Allegheny Ludlum Steel Corporation [28].

Density (kg/m <sup>3</sup> )	7990
Specific Heat (J/kg K)	500
Thermal Conductivity (W/m K)	21.4
Coefficient of Thermal Expansion (0-871 C) ( $10^{-6}C^{-1}$ )	11.1
Stress to rupture in 100 hours (871 C) (MPa)	41.4
Stress to rupture in 1000 hours (871 C) (MPa)	20.7

Table B.3: Properties 316 Stainless Steel.

## B.4 Haynes 214

Table B.4 lists relevant properties of Haynes 214. This data comes from Haynes [29]. In CFD simulations, temperature dependence was modeled for specific heat and thermal conductivity using a polynomial function.

Density (kg/m <sup>3</sup> )	8050
Specific Heat (700 C) (J/kg K)	668
Thermal Conductivity (700 C) (W/m K)	26.9
Coefficient of Thermal Expansion (0-700 C) ( $10^{-6}C^{-1}$ )	15.8
Stress to rupture in 100 hours (870 C) (MPa)	91
Stress to rupture in 1000 hours (870 C) (MPa)	54

Table B.4: Properties Haynes 214.

## B.5 Haynes 230

Table B.5 lists relevant properties of Haynes 230. This data comes from Haynes [30]. In CFD simulations, temperature dependence is modeled for specific heat and thermal conductivity using a polynomial function.

Density (kg/m <sup>3</sup> )	8970
Specific Heat (700 C) (J/kg K)	574
Thermal Conductivity (700 C) (W/m K)	22.4
Coefficient of Thermal Expansion (0-700 C) ( $10^{-6}C^{-1}$ )	14.7
Stress to rupture in 100 hours (870 C) (MPa)	83
Stress to rupture in 1000 hours (870 C) (MPa)	57

Table B.5: Properties Haynes 230.

## APPENDIX C. EXPERIMENTAL VALIDATION

---

The following section discusses numerical modeling of insulation heat loss. This is not necessary for validation of key experimental variables and is therefore presented as an appendix.

Numerical modeling of the heat loss through the insulated walls is sought. To do this, a temperature profile for the exterior surface of the receiver is generated from thermocouple measurements using a simple two-dimensional conduction model applied over the exterior surfaces of the device. This temperature profile is then applied as a constant temperature boundary condition (Dirichlet) to CFD simulations. The constant temperature condition leads to heat transfer through the exterior walls.

Initially, a generated temperature profile was applied to CFD simulations for different experimental cases. In each case, the heat transfer through the exterior walls was very different than that predicted by the “heat loss curve”. In the simulation for some cases, heat was actually coming into the device through the insulated surfaces. The suspected issue was inaccuracy in the generated temperature profile. Varying the temperature profile shows that the simulated heat loss is very sensitive to this profile.

Instead, three experimental cases are used to first calibrate a scaling factor. The scaling factor is applied to the thermocouple measurement before generating the profile. The scaling factor is adjusted until the heat loss in the simulation matches that predicted by the “heat loss curve”.

Figure C.1 shows the results of the calibration as a plot of average body tem-

perature versus the required scaling factor to match the heat loss predicted by the “heat loss curve”. The scaling factor decreases slightly with body temperature. A fourth simulation is performed for a fourth experimental case with a different average body temperature than the calibration cases. The scaling factor is calculated based on the results of the calibration. The simulation heat loss is within 12% of that predicted by the “heat loss curve”.

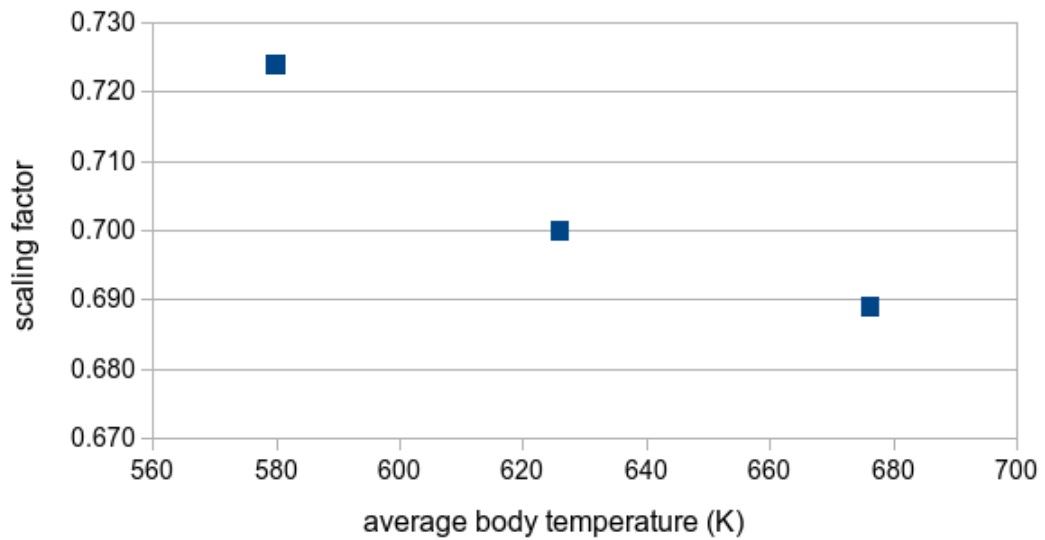


Figure C.1: Plot of scaling factor required to match “heat loss curve” in simulation versus average body temperature.

## REFERENCES

- [1] Bhubaneswari Parida, S Iniyar, and Ranko Goic, “A review of solar photovoltaic technologies,” *Renewable and sustainable energy reviews*, vol. 15, no. 3, pp. 1625–1636, 2011.
- [2] M. Romero, R. Buck, and J.E. Pacheco, “An update on solar central receiver systems, projects, and technologies,” *Journal of Solar Energy Engineering*, vol. 124, pp. 98, 2002.
- [3] Gregory J Kolb, “An evaluation of possible next-generation high-temperature molten-salt power towers,” *Albuquerque, NM: Sandia National Laboratories*, 2011.
- [4] Antonio L Ávila-Marín, “Volumetric receivers in solar thermal power plants with central receiver system technology: a review,” *Solar Energy*, vol. 85, no. 5, pp. 891–910, 2011.
- [5] E.G. Feher, “The supercritical thermodynamic power cycle,” in *Advances in energy conversion engineering*. ASME, 1967, pp. 37–44.
- [6] Dynalene, “Dynalene ms-1,” On the WWW, 2014, URL [http://www.dynalene.com/v/vspfiles/templates/210/datasheets/Dynalene\\_MS-1\\_Technical\\_DataSheet.pdf](http://www.dynalene.com/v/vspfiles/templates/210/datasheets/Dynalene_MS-1_Technical_DataSheet.pdf).
- [7] Nathan P Siegel, Clifford K Ho, Siri S Khalsa, and Gregory J Kolb, “Development and evaluation of a prototype solid particle receiver: on-sun testing and model validation,” *Journal of Solar Energy Engineering*, vol. 132, no. 2, pp. 021008, 2010.
- [8] Gary E. Rochau, “Supercritical CO2 Brayton Cycle: The DOE Program,” May 2011.
- [9] D.B. Tuckerman and RFW Pease, “High-performance heat sinking for vlsi,” *Electron Device Letters, IEEE*, vol. 2, no. 5, pp. 126–129, 1981.
- [10] R. K. Shah and A. L. London, *Laminar Flow Forced Convection in Ducts*, Academic Press, New York, NY, 1978.
- [11] A. Siu-Ho, W. Qu, and F. Pfefferkorn, “Experimental study of pressure drop and heat transfer in a single-phase micropin-fin heat sink,” *Transactions-Americal Society of Mechanical Engineers Journal of Electronic Packaging*, vol. 129, no. 4, pp. 479, 2007.

- [12] Y. Peles, A. Koşar, C. Mishra, C.J. Kuo, and B. Schneider, “Forced convective heat transfer across a pin fin micro heat sink,” *International Journal of Heat and Mass Transfer*, vol. 48, no. 17, pp. 3615–3627, 2005.
- [13] K.A. Moores, J. Kim, and Y.K. Joshi, “Heat transfer and fluid flow in shrouded pin fin arrays with and without tip clearance,” *International Journal of Heat and Mass Transfer*, vol. 52, no. 25, pp. 5978–5989, 2009.
- [14] A. Kosar, C. Mishra, and Y. Peles, “Laminar flow across a bank of low aspect ratio micro pin fins,” *Transactions of the ASME-I-Journal of Fluids Engineering*, vol. 127, no. 3, pp. 419–430, 2005.
- [15] A. Kosar and Y. Peles, “Thermal-hydraulic performance of mems-based pin fin heat sink,” *Transactions-American Society of Mechanical Engineers Journal of Heat Transfer*, vol. 128, no. 2, pp. 121, 2006.
- [16] AK Saha and S. Acharya, “Parametric study of unsteady flow and heat transfer in a pin-fin heat exchanger,” *International journal of heat and mass transfer*, vol. 46, no. 20, pp. 3815–3830, 2003.
- [17] N. Sahiti, A. Lemouedda, D. Stojkovic, F. Durst, and E. Franz, “Performance comparison of pin fin in-duct flow arrays with various pin cross-sections,” *Applied Thermal Engineering*, vol. 26, no. 11, pp. 1176–1192, 2006.
- [18] W. Qu and A. Siu-Ho, “Liquid single-phase flow in an array of micro-pin-fins-part i. heat transfer characteristics,” *Journal of heat transfer*, vol. 130, no. 12, 2008.
- [19] W. Qu and A. Siu-Ho, “Liquid single-phase flow in an array of micro-pin-fins-part ii. pressure drop characteristics,” *Journal of heat transfer*, vol. 130, no. 12, 2008.
- [20] K.T. Chiang, F.P. Chang, and T.C. Tsai, “Optimum design parameters of pin-fin heat sink using the grey-fuzzy logic based on the orthogonal arrays,” *International communications in heat and mass transfer*, vol. 33, no. 6, pp. 744–752, 2006.
- [21] Henk Kaarle Versteeg and Weeratunge Malalasekera, *An introduction to computational fluid dynamics: the finite volume method*, Pearson Education, 2007.
- [22] Anthony Bedford and Kenneth M. Liechti, *Mechanics of Materials*, Prentice Hall, Upper Saddle River, NJ, 2000.
- [23] Tempil, “Pyromark,” On the WWW, 2013, URL <http://www.tempil.com/products/pyromark>.

- [24] Frank P. Incropera, David P. DeWitt, Theodore L. Bergman, and Adrienne S. Lavine, *Fundamentals of Heat and Mass Transfer*, John Wiley & Sons, Hoboken, NJ, sixth edition, 2007.
- [25] A. Fenghour, W.A. Wakeham, and V. Vesovic, “The viscosity of carbon dioxide,” *Journal of Physical and Chemical Reference Data*, vol. 27, no. 1, pp. 31–44, 1998.
- [26] R. Span and W. Wagner, “A new equation of state for carbon dioxide covering the fluid region from the triple-point temperature to 1100 k at pressures up to 800 mpa,” *Journal of physical and chemical reference data*, vol. 25, no. 6, 1996.
- [27] V. Vesovic, WA Wakeham, GA Olchowy, JV Sengers, JTR Watson, and J. Millat, “The transport properties of carbon dioxide,” *Journal of Physical and Chemical Reference Data*, vol. 19, no. 3, pp. 763–808, 1990.
- [28] Stainless Steel Handbook, “Allegheny ludlum steel corporation,” *Pittsburgh, Pa*, 1956.
- [29] Haynes, “Haynes 214 alloy,” On the WWW, 2014, URL <http://www.haynesintl.com/pdf/h3008.pdf>.
- [30] Haynes, “Haynes 230 alloy,” On the WWW, 2014, URL <http://www.haynesintl.com/pdf/h3000.pdf>.